Characterisation unstable behaviour of a centrifugal pump in organ perfusion via experimental and numerical analysis

Leon V. Wierenga
Student number: S3162354
Research project Mechanical Engineering

Research Group: CMME
First supervisor: A. O. Krushynska
Second supervisor: M. Ghandchi Tehrani

Table of Contents

1. Abstract **4**
2. Foreword **4**
3. Introduction **5**
3.1 Problem description 6
3.2 Research Questions 8
3.2.1 Eigenfrequency problem 8
3.2.2 Pump performance 8
3.2.3 Internal Flow Behaviour 9
3.3 Research Methodology 9
3.4 Background Literature 10
3.4.1 Theoretical interpretation of the eigenfrequency problem 10
3.4.1.1 Eigenfrequency theory: The Mass-spring system 11
3.4.1.1.1 Damped system 11
3.4.1.1.2 Multiple DOF systems 12
3.4.1.2 Theory on resonance 13
3.4.1.3 Blade-pass frequency 13
3.4.1.4 Flow induced vibrations/Vortex shedding 14
3.4.2 Performance and Stability Experiments 14
3.4.3 CFD for centrifugal pumps 15
3.4.4 Balance of forces in centrifugal pumps 16
3.4.4.1 Axial Forces 17
3.4.4.2 Radial Forces 17
4. Modelling approach **18**
4.1.1 Assessment of the application 18
4.1.2 Simplifying assumptions for the experimental model 20
4.1.2 Simplifying assumptions for the numerical model 21
5. Materials/Methods **22**
5.1 Materials and methods for the Experimental Model 22
5.1.1 Materials 22
5.1.2 Methods 26
5.1.2.1 Methods Performance test 26
5.1.2.2 Stability experiment 26
5.1.2.3 Designing experiment conditions 27
5.1.2.4 Design Alterations 28
5.1.2.5 Data processing 29
5.2 Materials and methods for the numerical models 29
5.2.1 Materials 29
5.2.2 Methods 29
5.2.2.1 Eigenfrequency model 29

5.2.2.2 CFD model 30
6. Results 32
6.1 Eigenfrequency model results 32
6.1.1 Eigenfrequencies 2D model 32
6.1.2 Mode Shapes 2D model 32
6.1.3 Eigenfrequencies 3D model 33
6.1.4 Mode Shapes 3D model 34
6.2 Performance test and stability experiment results 34
6.2.1 Mean output parameters: pressure difference and flow rate 34
6.2.2 Q-H curves 37
6.2.3 Stability regime results per rotational speed 38
6.3 CFD model results 39
6.3.1 CFD analysis of the conventional impeller pump model 39
6.3.2 CFD analysis of the closed hole impeller pump model 42
6.3.3 Calculations on the balance of forces 44
7. Discussion 45
7.1 Interpretation of the eigenfrequency model results 45
7.2 Discussing the possibility of an eigenfrequency problem 46
7.2 Interpretation of the performance test results 47
7.3 Discussing the Q-H curves 49
7.4 Interpretation of the stability experiment results 49
7.5 Interpretation of the CFD model results 51
7.5.1 Figures on the internal flow behaviour of the conventional impeller 51
7.5.2 Output and performance tables of the conventional impeller 52
7.5.3 Output and performance results from the auxiliary sweep for the conventional impeller design 52
7.5.4 Comparing the internal flow behaviour of the closed impeller to the conventional impeller design 53
7.5.5 Comparing the output and performance parameters of the closed impeller to the conventional impeller design 54
7.5.6 Comparing the auxiliary sweep results of the closed impeller to the conventional impeller design 54
7.6 Discussion on the balance of forces 55
8. Conclusion & Recommendations 56
8.1 Conclusion on eigenfrequency 56
8.2 Recommendations for the eigenfrequency analysis 57
8.3 Conclusion on the pump performance & stability 57
8.4 Recommendations for the performance test and stability experiment 58
8.5 Conclusion on the CFD analysis of the internal flow behaviour 59
8.6 Recommendations on the CFD model and numerical characterisation of the internal flow behaviour 60
8.7 Conclusion on the balance of forces results 60

8.8 Recommendations on the assessment of the balance of forces 61
9. Appendix 62
9.1 Modelling instructions 2D eigenfrequency model 62
9.2 Modelling instructions 3D eigenfrequency model 70
9.3 Modelling instructions CFD model 81
9.4 List of performance variables of the CFD model 84
9.5 List of eigenfrequencies 2D model 85
9.6 List of eigenfrequencies of 3D model 87
9.7 Mean output parameters of the performance test and stability experiment 89
9.8 Stability results table for sample 1-5;A-E 92
9.9 Mean output parameters of the performance test and stability experiment for the altered samples with closed holes 92
9.10 Stability results table for sample A*-E* 95
9.11 Additional figures 96
9.12 T-test results 103
10. Bibliography 107

1. Abstract

Centrifugal pumps are the most common type of pump used in industrial, agricultural and domestic fields. To design a higher-performance pump, design optimization using mechanical concepts is required. This project covers the study of the poorly understood mechanical behaviour, performance and internal flow behaviour at higher rotational speeds of the XVIVO cirQlife pump – a centrifugal pump used in the field of biomedical engineering for a hypothermic- and normothermic machine perfusion medical device. The characteristics of the pump have been investigated through a combination of numerical analysis of the linear dynamics and nonlinear fluid dynamics, and experimental tests on the pump performance. Furthermore, the influence on the performance and the internal flow behaviour by the holes in the shaft of the impeller has been investigated by altering the design both experimentally and numerically. Finally, conclusions have been made based on the results and discussion of the experimental and numerical models and recommendations have been given for future research to investigate possible design changes to the centrifugal pump.

2. Foreword

The request for the study carried out in this thesis originates from the company XVIVO B.V., more specifically their department XVIVO Abdominal, located in Groningen, the Netherlands. This department was originally founded as a spin-off from PhD research regarding liver perfusion at the Universitair Medisch Centrum Groningen (UMCG. The initial version of the “Organ Assist”, contained a fluid pump obtained from an external manufacturer for perfusing the organ. During the continuous development cycle of the “Organ Assist” this manufacturer stopped with the manufacturing of this pump. This required Organ Assist to redesign their fluid

pump, reallocating the design process for the pump head to Mecora GmbH. The design created by this third-party company incorporated an innovative impeller design. Instead of a rigid one, it used a moveable impeller balancing on an axis via a single ball bearing, and being pulled down onto the axis via a set of four magnets present in the lower part of the impeller opposing a set of four magnets present in the electromotor below the pump head. The design for the new pump met the requirements and was incorporated into the medical device.

The request for investigating the stability behaviour of this fluid pump used in their system arose when the requirements for the perfusion device changed as research on organ perfusion for organ transplantation continued and desired requirements for hypothermic machine perfusion and normothermic machine perfusion shifted. It appeared that the fluid pump was not able to meet the requirements for other organs such as the lungs anymore, with the pump head MECORA design displaying stability issues at higher rotational speeds. The unstable performance of the fluid pump had become a limiting factor for XVIVO Abdominal, hampering their progress in researching the optimal settings of their machine perfusion device to allow for maximising the life expectancy of different classes of transplanted organs. As the origin of the stability issues of the pump head is poorly understood, it is of most interest for XVIVO Abdominal to understand possible reasons for the unstable behaviour of the pump at higher rotational speeds.

This thesis has been the start of the investigation of the stability issues and is therefore original, i.e., not built on any previous research regarding the parameters of the fluid pump.

3. Introduction

The centrifugal pump is the most commonly used pump in industrial, agricultural and domestic applications. This type of pump allows for an even volume flow, is low in both purchase and maintenance costs due to fewer moving parts and is relatively small in size compared to other pump types with the same output specifications. However, centrifugal pumps also require the most detailed understanding of the internal flow behaviour as this is critical for its impeller design. Nonuniform internal pressure distribution, high flow rates and intricate velocity streamlines can ultimately lead to poor performance of the designed centrifugal pump and even unstable behaviour of components of the pump.[1]

To predict the performance of a centrifugal pump, a deep understanding of the flow behaviour in different parts of the pump is required. Traditionally this is achieved by extensive experimental model testing. However, this process is tedious, time-consuming and requires a lot of expenses. On the other hand, a theoretical approach is only able to give a value, while a root cause for poor performance or instability remains undetermined. In the last decade, computational fluid dynamics (CFD) has come to play an increasingly important role in the prediction of internal flow behaviour through centrifugal pumps, successfully contributing to the improvement of their design. However, the CFD method is not able to predict the fluid behaviour without any prior knowledge of the system. Combining the experimental and CFD methods have shown to complement each other in the characterisation of fluid dynamics in complex systems. [2]

3.1 Problem description

For this project, the root cause of a stability problem in the performance of the XVIVO cirQlife pump is studied. This centrifugal pump is applied for organ perfusion as a pumping component in the XVIVO perfusion machine, which performs Hypothermic Machine Perfusion (HMP) on livers and kidneys for transplantation.

HMP was introduced as a method to allow better and longer preservation of a donor organ. In HMP, the donor organ is continuously perfused with a preservation solution with a temperature of 4-12℃. This allows for a continuous supply of nutrients and a continuous removal of waste products from the liver cells. Additionally, HMP allowed for monitoring of the organ quality by intravascular organ resistance measurements, bio-impedance measurements and perfusate analysis, making it possible to add medication to the preservation solution to increase the quality of the organ.[3,4]

In recent years, research on liver perfusion has taken a great interest in combining HMP with Normothermic Machine Perfusion (NMP) at a temperature close to body temperature as this combination has shown more promising results regarding the quality of an organ in terms of oxidative stress, tissue inflammation and improved metabolic recovery of higher-risk donor livers.[5]

To assist research on NMP, the XVIVO perfusion device has been adapted to allow for the settings required for organ perfusion at body temperature. However, during testing of the XVIVO perfusion device for NMP of organs with high flow rate requirements, it was found that the cirQlife pump, responsible for pumping the perfusion medium through the fluid circuit on which the donor organ is connected, was unable to meet the set requirements for this type of perfusion. At the required high rotational velocity (over 5000 RPM) of the impeller of the pump, the impeller showed unstable behaviour by lifting of the axis, becoming ‘airborne’ in the process, making contact with other components of the pump, while continuing to rotate. This limiting factor obstructs extended NMP research using the XVIVO perfusion device perfusion machine.

In order to approach the understanding of the origin of this unstable behaviour of the impeller, first the design of this centrifugal pump should be discussed. As shown schematically in figure 1., the cirQlife pump is a centrifugal pump consisting of a shell-shaped housing (2 & 3) with its inlet (1) on the top side and its outlet (1) laterally oriented. The housing is attached on top of a base (4). The inside of the pump contains an axis (9) attached to the base and a cone-shaped impeller (5-10). This impeller contains characteristic features: directly underneath the tip (6) two holes connecting the space below and above the impeller located at the transition from the tip to the shaft of the impeller are present, their centre points made visible with the black line. These holes prevent fluid underneath the pump from becoming standing fluid. This prevents more viscous fluids, e.g. perfusion medium or blood, from clotting. The ball bearing (8) connected to the bottom of the tip allows the impeller to remain on the axis while preserving five degrees of freedom. The impeller has six vanes, with larger and smaller vanes alternating each other. Four magnets (10) present in the lower part of the impeller pull the impeller onto the axis and allow it to rotate synchronically with the electromotor. Figure 2. shows the pump from different angles.

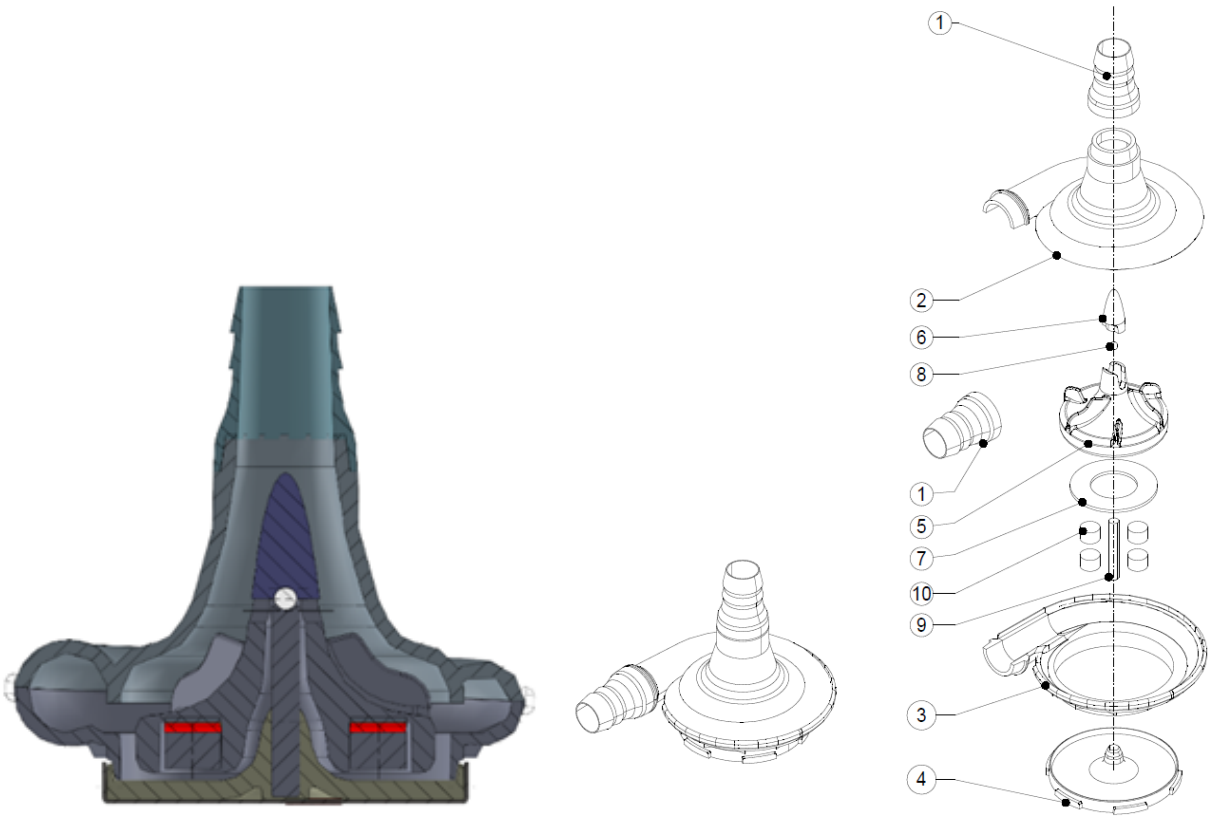

Figure 1. Schematic of the XVIVO cirQlife pump. Left: assembled. Right: separated in parts.

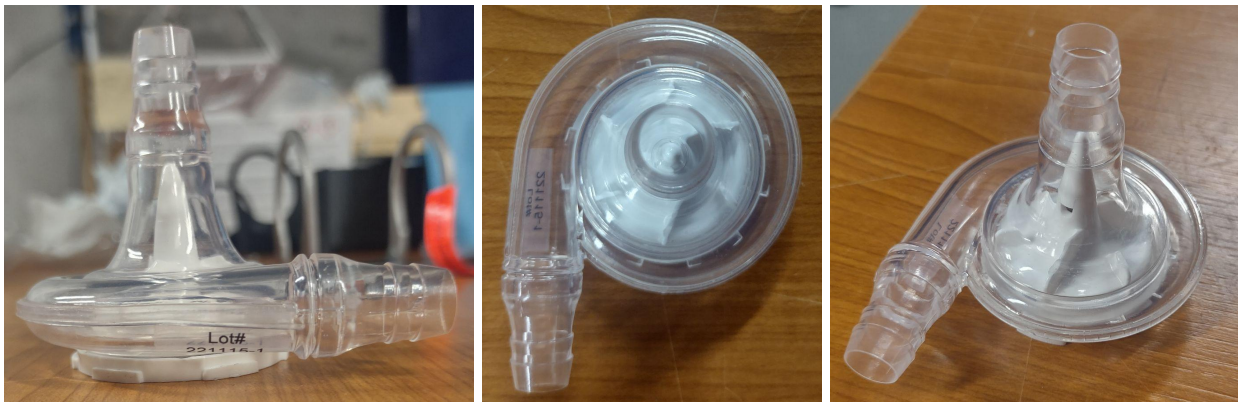

Figure 2. The XVIVO cirQlife centrifugal pump. Left: side view. Middle: top view. Right: overview.

Deep understanding of the dynamic behaviour of the pump and its components and the flow behaviour inside the pump is a necessity, in order to interpret what is causing the vibrations and unstable behaviour and to make correct improvements to the current pump design. Unfortunately, the input data for an in-depth analysis are lacking: there is no deeper understanding of the performance parameters of the cirQlife pump for higher rotational speeds, both the dynamic behaviour of the system as well as the internal flow behaviour at different operating speeds are not known, together with the resulting unstable behaviour of the rotating

impeller of the pump. It is therefore of most importance to start collecting and analysing these characteristics.

3.2 Research Questions

The main goal of this project is to investigate and characterise the dynamic behaviour, the internal flow behaviour and the performance of the XVIVO cirQlife centrifugal pump, as this knowledge may be crucial to explain the origin(s) of the observed instabilities. The overarching research question of this project can be formulated as:

RQ: What is the root cause of the unstable behaviour of the impeller in the XVIVO cirQlife centrifugal pump at higher rotational speeds?

This research question is rather global, as the root cause of unstable behaviour in an application with fluid flows can originate from several different sources. In order to make the research question more graspable, it is divided into research sub-questions covering these types of solid- and fluid dynamics.

3.2.1 Eigenfrequency problem

First, one of the primary causes of vibrations or instabilities in complex dynamic systems with a linear dynamic behaviour are resonances that occur at eigenfrequencies (natural frequencies) of the systems as a whole or of its separate components. Therefore, the first subdivision of the research questions refers to the eigenfrequency problem:

RSQ1: Can resonances linked to the eigenfrequencies of the XVIVO cirQlife centrifugal pump or its components be responsible for causing the vibrations inducing its unstable behaviour?

The RSQ1 (Research Sub-Question 1) implies both eigenfrequencies dependent solely on the mechanical properties and the geometry of the centrifugal pump and those caused by the interaction between the centrifugal pump and surrounding components, including fluid-structure interactions. If the ratio between a vibration frequency of a specific origin and one of the obtained values for the eigenfrequencies lies within the range $0.5 > wa/w0 < 1.5$, where wa is the vibration frequency and w0 is one of the simulated eigenfrequencies, the possibility of an eigenfrequency problem cannot be excluded. If this ratio is outside this range, the possibility of an eigenfrequency problem because of this vibration is rejected. Relevant theories related to the eigenfrequency problem are discussed more thoroughly in 3.4.1 by analysing the general literature.

3.2.2 Pump performance

Second, the lack of deeper understanding of higher operational settings for the XVIVO cirQlife pump requires the analysis of the pump performance. Without the knowledge of basic parameters of the pump, e.g. suction- and discharge pressure and corresponding pressure head, flow rate at higher operating speeds, and stability observations for different, new

characteristic settings, the analysis of the internal flow behaviour in the pump is impossible. Thus, the second research sub-question is:

RSQ2: What are the performance parameters of the XVIVO cirQlife pump at higher rotational speeds?

Furthermore, the influence of the design aspects of the pump is questioned. The implementation of the holes inside the shaft of the impeller. With RSQ2, it is a small step to compare the performance parameters of the conventional design to the performance parameters of a changed design of the pump, excluding any holes in the impeller. An additional research sub-question is:

RSQ3: What influence do the holes inside the impeller have on the performance parameters compared to an impeller design without holes?

In the null hypothesis for this RSQ3 the closed holes impeller design shows no significant difference in performance parameters to the conventional impeller design. In the alternative hypothesis the closed holes impeller design does show a significant difference in performance parameters to the conventional design.

3.2.3 Internal Flow Behaviour

The internal flow behaviour in the pump is the third important characteristic that should be studied, since it cannot be well understood through the results of a performance test. Therefore a third subdivision in this research revolves the characterisation of the internal flow behaviour with the aim to find out whether the fluid dynamics of the pump can be responsible for the observed pump instabilities or not:

RSQ4: Can the internal flow behaviour of the XVIVO cirQlife centrifugal pump create a force imbalance large enough to cause the unstable behaviour?

In the null hypothesis for RSQ4 the internal flow behaviour is not capable of creating a combined upwards lift force that exceeds the combined downwards suction forces. For the alternative hypothesis this combined lift force is capable of creating a combined upwards lift force that exceeds the magnetic force pulling the impeller down, making it a probable cause of the unstable behaviour.

3.3 Research Methodology

To answer the posed RSQs, different methodological approaches are used. For RSQ1, the eigenfrequency analysis of the pump is done by means of the computational solid mechanics FEA using a numerical model of the centrifugal pump. The eigenfrequency analysis allows estimating the eigenfrequencies of an empty pump, without fluid. Then, the theoretical analysis is performed to predict whether different vibration-exciting phenomena can excite any

of the eigenfrequencies and cause a resonance. Section 3.4.1 further elaborates on the theory behind the concept of eigenfrequencies of a structure and the related modelling approaches, as well as on the different vibration-exciting phenomena.

The RSQ2 and RSQ3 cannot be answered without prior knowledge of the output parameters. For the suction- and discharge pressure and flow rate at different operating conditions, it is impossible to develop a numerical model reliably representing these performance measurements. Furthermore, simulating mechanical instabilities is a challenging topic by itself, especially for such a complex structure as the pump. Therefore, an experimental approach is required to determine the performance parameters of the pump. It implies running a performance test with an experimental setup to model different operational settings. The setup of this experiment for centrifugal pumps is further explained in section 3.4.2. The combination of a performance test and a stability observation test, can provide a performance sheet of the pump. Furthermore, it enables the experimental determination of the stability regimes of the pump.

Subsequently, using the performance parameters obtained from the experiments performed for RSQ2, it will be attempted to numerically approach the internal flow behaviour of the pump via computational fluid dynamics (CFD). It is aimed to obtain key parameters characterising this internal flow behaviour – pressure, flow velocity and streamlines in different parts of the pump to be able to answer RSQ4. In section 3.4.3, relevant literature on CFD analysis of internal flow behaviour of centrifugal pumps is elaborated on. Finally, the data obtained from the simulation is used to analytically calculate if the internal flow behaviour is able to cause a force exceeding the magnetic force of the magnets holding the impeller on the axis.

3.4 Background Literature

The numerical- and experimental models used in this study are based on fundamental literature on those models. In the case of an eigenfrequency problem, this fundamental literature is often more meaningful to the aid of a research than eigenfrequency research performed for a specific structure. For the experimental setup for a performance test and stability observation experiment however, it is important to use an experimental setup very similar to setups used in previous studies. For CFD, literature on several centrifugal pumps is used to properly set up the boundary conditions of the model.

3.4.1 Theoretical interpretation of the eigenfrequency problem

One of the first steps in characterising the dynamic behaviour of any structure is research of linear behaviour. In the case of free vibrations of an elastic body, the broad possibility of an eigenfrequency problem is often extensively investigated for structures in endless applications. Eigenfrequencies or natural frequencies of a mechanical system are discrete frequencies at which the system is prone to vibrate/oscillate in absence of any driving force. When a body or system is vibrating at a certain eigenfrequency, a structure deforms into a corresponding shape, the eigenmode or normal mode. In the absence of damping, the vibration amplitude can take critically large values. These vibrations are therefore potentially able to cause damage to the structure and the surrounding area, requiring immediate redesigning

before the structure is even realised. The origin of an eigenfrequency problem for a complex system such as a centrifugal pump can vary from vibrations created by the rotational speed, blade-pass frequency from the impeller material, or from flow induced vibrations and vortex shedding originating from the fluid flow.[6]

3.4.1.1 Eigenfrequency theory: The Mass-spring system

The concept of natural frequencies and natural vibrations can be explained using a simple single degree of freedom (DOF) mass-spring system as shown in figure 3. This system consists of a mass attached to a spring and undergoes a simple harmonic motion along one direction in the absence of damping from the surrounding medium or in the spring.

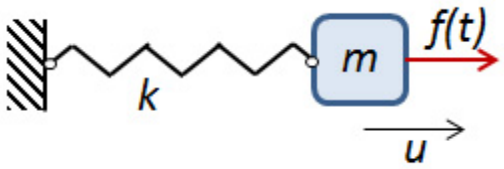

Figure 3. Undamped mass-spring system with 1 DOF.[6]

In this 1-DOF system, where *m* denotes the mass, *k* is the spring stiffness, *u* is the displacement in a 1D direction and *f(t)* equals the external force function of the system, the equation of motion for the mass is expressed as $m\ddot{u} + ku = f(t)$.
If, however, no external force is acting on the mass, i.e. f(t) = 0, nonzero solutions may still exist. It can be found that $u = A\sin\omega_0 t + B\cos\omega_0 t$ fulfils the homogeneous equation of motion if $\omega_0 = \sqrt{\frac{k}{m}}$. Here, ω_0 is the natural angular frequency (in rad/s), which is related to natural frequency f_0 (in Hz.) through $\omega_0 = 2\pi f_0$. I.e., $f = \frac{1}{2\pi}\sqrt{\frac{k}{m}}$. This solution can be interpreted as a free vibration existing at exactly this frequency without any external excitation (f(t) = 0), i.e. the mass would oscillate forever at this frequency. Since the system is undamped, the energy of the system is conserved: the kinetic energy of the mass is transformed into the strain energy of the spring and the other way around. The expression for ω_0 shows how the angular- and therefore also eigenfrequency is influenced by spring stiffness and mass $\omega_0 \propto \sqrt{\frac{\text{stiffness}}{\text{inertia}}}$.[6,7]

3.4.1.1.1 Damped system

In a real situation there is always some form of damping, resulting in the oscillations fading away over time. When viscous damping is included in the system, the equation of motion of the mass-spring-damper system is $m\ddot{u} + c\dot{u} + ku = f(t)$ for the system shown in figure 4., where *c* is the damping coefficient.

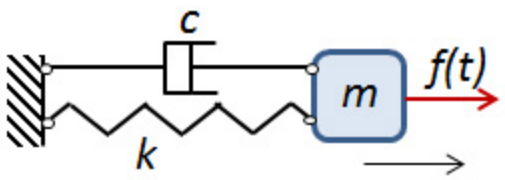

Figure 4. viscous damping in a system with 1 DOF.[6]

Then, time dependent harmonic functions are represented by $e^{i\omega t}$ and the displacement can be written as $u = \tilde{u}e^{i\omega t}$, where $\tilde{u}$ is a complex-valued amplitude. Each time derivative gives a factor $i\omega$. Without any external forces, this equation of motion can be written as $\left(-\omega^2 m + i\omega c + k\right)\tilde{u}e^{i\omega t} = 0$.

Using the earlier mentioned expression for ω_0 (equation X.) and the notation for the damping ratio $\zeta = \frac{c}{2\sqrt{km}}$, the equation for the eigenvalue reads $-\omega^2 + 2i\zeta\omega_0\omega + \omega_0^2 = 0$ with the solutions $\omega_{1,2} = \omega_0\left(i\zeta \pm \sqrt{(1-\zeta^2)}\right)$. ω_0 here is the (undamped) natural angular frequency and ζ is the damping ratio. Inserting this value of ω in the complex-valued displacement results in $u = \tilde{u}e^{-\zeta\omega_0 t}e^{\pm i\sqrt{1-\zeta^2}\omega_0 t} = \tilde{u}e^{-\zeta\omega_0 t}e^{\pm i\omega_d t}$, with $\tilde{u}$ being an arbitrary amplitude and ω_d denoting the damped natural angular frequency $\omega_d = \omega_0\sqrt{1-\zeta^2}$. The second exponentially decaying multiplier, describes then the decay of free oscillations over time in the damped system. Oscillating solutions can only exist when $\zeta < 1$. If ζ is larger than 1, the system is overdamped and will not vibrate at all. Damping processes in multi-DOF systems are difficult to characterise. The viscous damping used above is popular because of its mathematical simplicity.

Another common damping model is hysteretic damping or loss factor damping. This model cannot be explicitly described in terms of time derivatives, but is expressed directly in terms of complex numbers in the frequency domain. The force in the spring is assumed to be out of phase with the displacement, which results in a complex-valued stiffness. The resulting eigenvalue equation becomes $\left(-\omega^2 m + k(1+i\eta)\right)\tilde{u}e^{i\omega t} = 0$, with η being the loss factor. The complex-valued complex natural angular frequency will be $\omega = \omega_0\sqrt{(1+i\eta)}$. For small values of the loss factor, the decay in amplitude for the oscillations is given by the exponential factor $e^{-\eta\omega_0 t/2}$.[6,7]

3.4.1.1.2 Multiple DOF systems

A linear system with multiple degrees of freedom (DOFs), such as shown in figure 5., can be characterised by a matrix equation $\mathbf{M}\ddot{\mathbf{u}} + \mathbf{C}\dot{\mathbf{u}} + \mathbf{K}\mathbf{u} = \mathbf{f}(t)$, where second order tensor $\mathbf{M}$ is a mass matrix, second order tensor $\mathbf{C}$ denotes the damping matrix, second order

tensor $\mathbf{K}$ is a stiffness matrix, first order tensor $\mathbf{u}$ is the displacement row vector containing every DOF and first order tensor $\mathbf{f}(t)$ is the force vector.

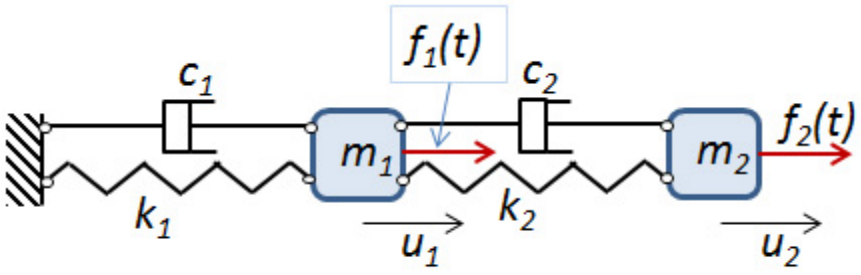

Figure 5. Mass-spring-damper system with two degrees of freedom.[6]

The equation of motion for a free oscillation problem is then described by the equations in the matrix form $\left(-\omega^2\mathbf{M}+i\omega\mathbf{C}+\mathbf{K}\right)\tilde{\mathbf{u}}e^{i\omega t}=\mathbf{0}$, the structure of which is essentially the same as that for the equation for the 1-DOF mass-spring-damper system. The eigenvalues, angular natural frequencies and subsequently the eigenfrequencies can be determined in the same way as described above, i.e, by solving equation $\det\left(-\omega^2\mathbf{M}+i\omega\mathbf{C}+\mathbf{K}\right)=\mathbf{0}$. For multiple DOFs however, other methods are more commonly used. The number of eigenvalues is equal to the rank of the mass matrix. Each eigenvalue has its corresponding (eigen)mode. When a structure is oscillating at a natural frequency, the shape of the deformation is that of the corresponding eigenmode.[6,7]

3.4.1.2 Theory on resonance

Eigenfrequencies play a prominent role in the phenomenon called resonance. If a dynamic system is excited by an oscillating force, *f(t) =/= 0*, at a frequency close to one of its eigenfrequencies, there occurs resonance . The dynamic system will oscillate at a higher amplitude than that excited by a similar force on other, non-resonant frequencies, i.e. the system resonates. Frequencies at which the response amplitude has a relative maximum are known as resonance frequencies of the system. Harmonic forces of a frequency near a resonant frequency of the system produce large amplitude oscillations in the system due to the storage of vibrational energy.[8]

3.4.1.3 Blade-pass frequency

The blade-pass frequency is the frequency at which the vanes of the centrifugal pump pass by the outlet of the pump. The blade-pass frequency is therefore equal to the rotational speed of the impeller multiplied by the number of blades on the impeller. When the blade-pass frequency is close to an eigenfrequency of a system, this can cause an eigenfrequency problem caused by this produced pure tone.

3.4.1.4 Flow induced vibrations/Vortex shedding

A flow induced vibration (FIV), or vortex shedding, is an oscillating flow that is the result of turbulence caused by discontinuities such as bends, tees, partially closed valves and small bore connections.[9] Laminar flow can be presented as a bundle of parallel streamlines. In the case of turbulence, the discontinuities disrupt this parallelity, as different streamlines collide with each other, creating vortices and detaching periodically from either side of the structure forming a Karman vortex street.[10] This vortex flow past the body creates alternating low-pressure vortices from the back of the object downstream and the structure will tend to move towards the low-pressure zone. If the body is not rigidly mounted, driven by the energy of the flow the structure can start to resonate.[11] The excitatory vortex shedding frequency f is determined from the following formula:

$$\mathrm{St} = \frac{fd}{U}$$ (eq. 1)[11]

Where St is the Strouhal number (-), *d* the diameter of the cylinder (m) and *U* the velocity of the flow (m/s). The Strouhal number is a dimensionless number describing oscillating flow mechanisms and is related to the Reynolds number. The Reynolds number, Re_d, is a dimensionless quantity that assists in the prediction of flow patterns in different environments by measuring the ratio between inertial and viscous forces. A low Reynolds number indicates a flow dominated by laminar flow, while a high Reynolds number indicates a flow tending to be turbulent. This turbulence results from differences in speed and direction within the fluid. For a flow in a pipe with a Reynolds number between 250 and 200000, the Strouhal number can be estimated by using the formula:

$$\mathrm{St} = 0.198\left(1 - \frac{19.7}{\mathrm{Re}_d}\right)$$ (eq. 2)[11]

3.4.2 Performance and Stability Experiments

The performance of a centrifugal pump is critical to know if the pump is suitable for a specific application. Therefore, analysing the pump's performance parameters by the means of a performance test is a necessity to create a general performance sheet of a pump. In general, a performance test is conducted after both ensuring proper strength for the housing and testing for leaks, and properly balancing the impeller and rotor dynamics. Such tests are normally conducted by a manufacturer to prove that a pump has required specifications corresponding to those indicated in the pump datasheet and other purchase documents.[12]

Performance tests are performed for pumps of all shapes and sizes. The scope of the test and the contents of it are usually defined by standardised test plans agreed between the pump manufacturer and the pump purchaser, but the most important characteristics for this project is the Q-H curve.

The Q-H curve shows the volume flow rate, or capacity of a pump, that travels through the pump in a given time. The static head of a pump (H) can be defined as the maximum height (pressure) it can deliver. Through the Q-H curve the rate at which a pump can push fluid through the system can be defined in terms of the maximum height. Flow rate is one of the first parameters specified by a system designer, who determines the pump requirements on the flow rate allowing for a system to function properly. The capability of the pump at a specific RPM can

be obtained from its Q-H curve. [13, 14] The Q-H curve also enables a system designer to further select a desired pump based on power consumption and efficiency-flow rate relation of the pump.

3.4.3 CFD for centrifugal pumps

CFD has become a widely used tool to estimate flow characteristics and by knowing them to improve the performance of centrifugal pumps. With the aid of CFD simulations, the complex internal flow through different parts of a pump can be studied in different operating conditions.

In the field of CFD research a lot of research has been done on specific cases of centrifugal pumps. CFD research in centrifugal pumps is not perfect, as models are almost never able to simulate the complete real situation, containing errors on local level for specific cases, but in the process a lot is learned about CFD. For example, Mentzos et al. [15] performed CFD of the internal flow of a centrifugal pump with backwards curved vanes. The moving reference frame (MRF) approach used to include the interaction between an impeller and a volute completely failed, because of its fixed coupling formulation. However, recommendations were made for the model being used for basic understanding of the flow at various operating points. This transient analysis was recommended as a good option to study the interaction between an impeller and a spiral housing. Three-dimensional modelling of the centrifugal pump is shown in Fig. 6(a).

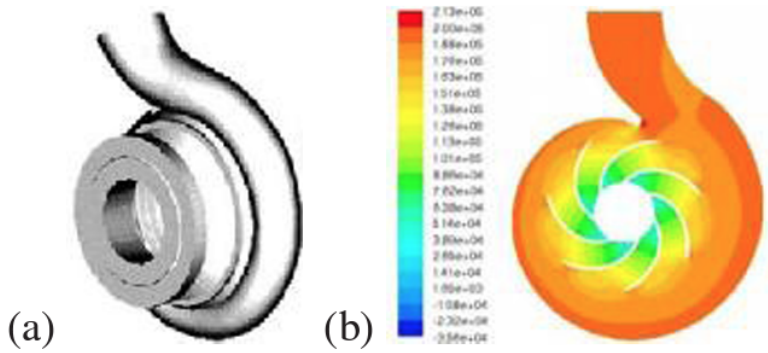

Fig. 6.(a) Three-dimensional computational model of the centrifugal pump with backwards curved vanes. (b) The static pressure contours in the pump at the operating conditions. [15]

Subsequently, Mentzos et al. [16] modelled the flow through an impeller of a centrifugal pump using the finite-volume method. A detailed structured mesh was used to discretize governing equations. This CFD technique was shown to enable the estimation of the pressure distribution, distinct flow patterns and Q-H curve of the pump. Though the mesh size was too large to investigate the boundary layer variables on a local level, the global boundary layer variables were captured well. This approach was recommended for the basic understanding of the internal fluid flow of a centrifugal pump at various global level operating points.

In most cases, CFD is used as an assisting tool to predict the internal flow behaviour in different parts of the pump before manufacturing the pump. However, it can also be useful in the process of modifying an existing system to predict the effects of the design on the internal flow behaviour numerically. Furthermore, the CFD analysis can assist in studying the effects of different internal flow parameters on a pump's performance.

Bacharoudis et al. [17] studied the performance of a pump by modifying the outlet blade angles, while keeping the rest of the design unchanged. At the nominal flow rate, increasing the outlet blade angle from 20° to 50°, the pump's pressure head increased by more than 6%. However, the hydraulic efficiency of the pump was reduced by 4.5%. Meanwhile, at high flow rates, this increased outlet blade angle caused significant improvement of the hydraulic efficiency.

More recently, Kim et al. [18] analysed the performance of a centrifugal pump by modifying four parameters of the design – 25 combinations for different values for the inlet angle of an impeller hub, the inlet angle of an impeller shroud, the outlet angle of an impeller hub, and the outlet angle of an impeller shroud – by using a CFD model that allowed choosing an optimised design for the impeller. Subsequently, four volute cases were designed differing in cross-section distributions compared to the cross-section distribution of the base volute. The numerical model was again used to analyse the modifications made to the design. It was concluded that a 90% cross-section distribution area compared to the base volute has both greater pressure head and efficiency.

These studies already show the great benefit of CFD for analysing internal flow behaviour of centrifugal pumps. CFD methods continue to improve including more extensive numerical computations, making it possible to increase the performance values of concept centrifugal pumps, as well as conceptual modifications to existing pumps.

3.4.4 Balance of forces in centrifugal pumps

The complex design and internal flow behaviour are accompanied by a more complex balance of forces in centrifugal pumps compared to that in other types of pumps. The forces acting in centrifugal pumps can be subdivided into 2 types: axial and radial forces, as schematically shown in a Free-Body diagram (FBD) in figure 7. for a single stage-stage centrifugal pump.

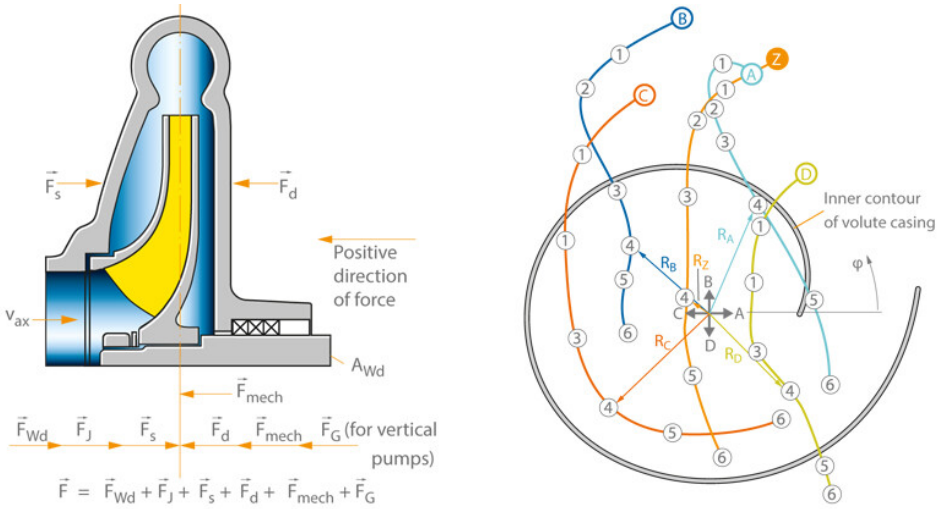

Figure 7. Balance of forces of a centrifugal pump. Left: axial forces, right: radial forces. [19,20]

3.4.4.1 Axial Forces

The left pane of figure 7. shows the axial forces acting on the impeller: the axial impeller force *F(1)*, composed of a discharge side component *F(d)* and a suction side component *F(s)*, momentum *F(J)*, static pressure force *F(Wd)*, and other mechanical forces *F(mech)* present in specific pump designs. The resultant force *F* of all the axial forces acting on the impeller of the centrifugal pump is called the axial thrust. [19]

The axial impeller force *F(1)* has components on both sides of the impeller. The axial impeller force *F(1)* is the difference between the axial forces on the discharge-side *F(d)* and suction-side *F(s)* impeller shroud: $F(1) = F(d) - F(s)$. These opposing forces can be described in terms of either the suction- or discharge pressure on that side of the impeller shroud over the relevant area of that side.

The momentum (FJ) is a force which constantly acts on the fluid contained in a defined space: $F(J) = \rho \cdot Q \cdot \Delta v,ax$. Here, *Q* is the flow rate (m^3/s), ρ is the density (kg/m^3) of the fluid handled and $\Delta v,ax$ is the difference between the axial components of the absolute velocity (m/s) at the inlet and outlet of the impeller.

The static pressures up- and downstream of the shaft seal *ss* create a resultant pressure force *F(Wd)* on the relevant shaft cross-section *A(ss)*: $F(Wd) = A(Wd) \cdot \Delta p(Wd)$. Here *A(Wd)* is the shaft cross-section, and $\Delta p(Wd)$ is the difference between the pressure upstream and downstream.

Other axial forces, the force of the rotor weight *F(G)* on non-horizontal centrifugal pumps or magnetic pull in the electric motor *F(mech)*, and axial thrust balancing through the use of bearings are added to the equation for specific cases of centrifugal pumps.

3.4.4.2 Radial Forces

The right pane of figure 7. shows the radial thrust acting on the impeller. Radial thrust can be divided into steady radial force and unsteady radial force. The steady radial force is expressed as $R = K \cdot \rho \cdot g \cdot H \cdot D \cdot B$. Here *R* is the steady radial force (N), *K* is the radial force

coefficient (1), ρ is the density of the fluid handled (kg/m^3), g is the gravitational constant (m/s^2), H equals the pressure head (m), D is the outside diameter of the impeller (m) and B equals the impeller outlet width (m).[20]

Unsteady radial forces cannot be explicitly defined, because their origins and characteristics can be different. Unsteady hydraulic radial forces is the most well-known example. These forces have a frequency = number of impeller vanes * rotational speed. These radial forces appear in all types of centrifugal pumps.

4. Modelling approach

To model the characteristics of the centrifugal pump as objectively as possible, both experimental- and numerical approaches have been used described in the materials/methods section. These corresponding models include simplifying assumptions that exclude some elements present in the application of the pump and do not completely resemble the performance of the XVIVO perfusion machine application. However, they are useful to analyse the effects of a range of relevant parameters on the working conditions of the pump.

4.1.1 Assessment of the application

As mentioned, the XVIVO cirQlife pump is applied in the XVIVO perfusion device. In this complex system the pump functions as the heart of the device, pumping a pulsatile flow of blood or perfusion medium through the circuit with its different components, towards and through the perfused organ. This means that, within the XVIVO perfusion device, the performance of the pump is influenced by multiple different elements. To be able to create a reliable experimental model, first an overview and assessment in terms of controllability of all pump performance influencing elements has been made. These elements are schematically shown in figure 8. with their relevant parameters labelled according to their controllability:

- fully controllable parameters *'C'*
- Variable parameters *'V'*
- Noise parameters, being difficult to control and having unknown exact values and thus unknown influence, labelled *'N'*.

The values and influence of the noise parameters are unknown and can only partially be reduced by testing multiple visually identical samples.

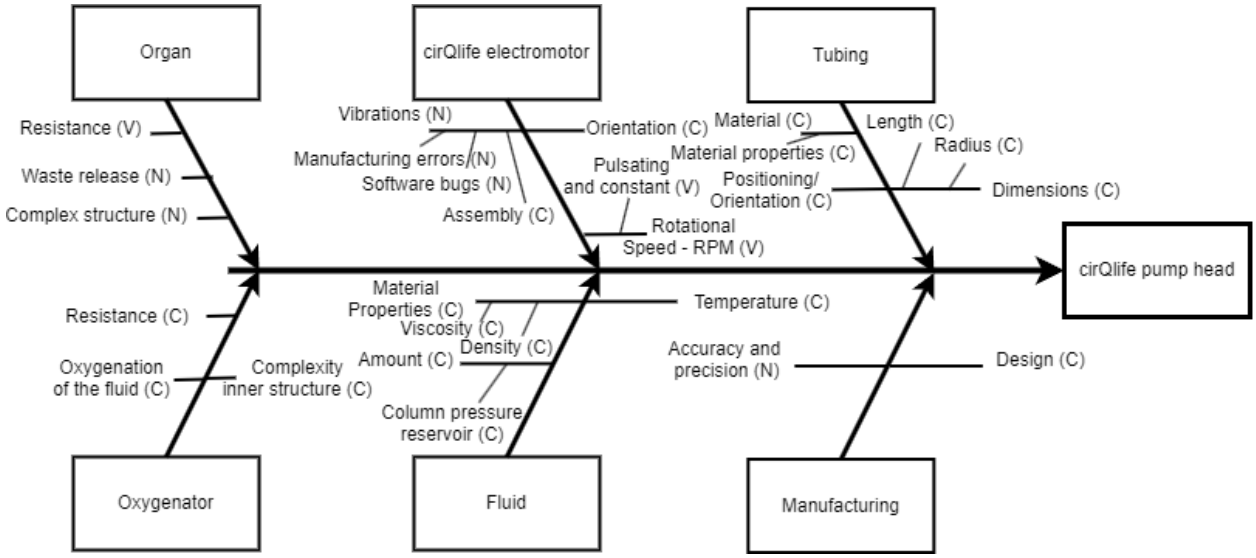

Figure 8. Influence analysis of all elements from the components in contact with the centrifugal pump. Labels: C = controllable parameter, V = variable parameter, N = noise parameter (uncontrollable).

Figure 8. shows that the fluid and tubing components are fully characterised by only controllable parameters with constant values. The amount of fluid and the material properties of the fluid used in the system, i.e. blood or perfusion medium, can all be controlled. The tube network of the device has also all been defined. Every tube used in the device has predefined dimensions, material properties and positioning.

Furthermore, the component ‘oxygenator’ describes a component in the XVIVO system that enriches the flowing fluid with oxygen. This manufactured component and its influences on the system have been fully characterised and therefore only consists of controllable parameters.

The element for the manufacturing of the pump head contains a noise component (N) governed by a limited accuracy and precision of the manufacturing process. The error margin of the manufacturing creates room for anomalies in a manufactured pump head that can display an incorrect performance of the pump head during experiments.

The ‘organ’ component contains one controllable, variable parameter in the ‘resistance’ element. This parameter varies with the operating temperature required for perfusion of a specific organ. However, the component also contains two noise parameters governed by the complex structure of the organ and uncontrollable waste release into the perfusion fluid from the organ. These parameters are organ-specific, varying for every organ sample, and therefore impossible to characterise in the planned tests.

Finally, the electromotor contains both a noise and a controllable variable parameter. Motor specific vibrations during operation have been identified as a noise. This noise cannot be controlled or overcome, as vibrations can differ between motors. The rotational speed is labelled as a variable parameter, as it can be varied during the operation of the device in order to increase or decrease the flow rate in the system, according to the requirements for a specific organ at any moment. This speed can furthermore also be altered between a pulsating or constant regime.

4.1.2 Simplifying assumptions for the experimental model

Using the influence analysis, aimed to simulate the mere effect of one variable parameter on the experimental results, it is necessary that only one variable element is changed, while the other elements are not altered, removed or added in the model. To achieve this and create a reproducible experimental model, simplifying assumptions have been made, by removing uncontrollable and unnecessary characteristic features, while simultaneously conserving as many characteristics as possible.

First, the circuit components that are theoretically able to cause the fluid flow to show turbulent behaviour have been excluded. For this purpose, the reservoir and tubing setup of the XVIVO perfusion device were excluded, as they contain multiple components capable of inducing turbulent flow; the tubing setup contains multiple elbow pipes in its tubing network, including the reservoir.[21] Furthermore the oxygenator has not been considered in the simplified experimental model. The addition of oxygen to the fluid was assessed as an unnecessary parameter. The tubing layout inside this component was also assessed to activate turbulent flow. Instead, a completely custom setup has been made for the experiments. This experimental setup contains a custom reservoir and no oxygenator component. The type of tubing used in the circuit has remained equal to the XVIVO perfusion device, as have the centrifugal pump and the electromotor. This model is discussed in section 5.1.1.

Second, in the experiments, only a constant flow has been considered. The rotational speed was labelled a variable element with an additional variation included for the type of rotational speed given by the electromotor. Pulsating speeds were excluded from this consideration, as the influence of a constant speed element was deemed more essential for the performance experiments of the pump. Simplifying the rotational speed to a strictly constant speed by excluding pulsating flow allows for easier setup of the experiments to obtain the Q-H curves.

Third, the ‘organ’ component has been simplified to a pallet of flow resistors with flow resistances comparable to organs. The noise parameters, different for any organ sample, were assessed as too impactful to the pump’s performance in the experimental model. The complex structure of the organ has therefore been simplified to a simple tube containing a narrowed part, allowing to assume the flow through the organs as a single flow through a cylindrical tube. Organ-resistance-mimicking resistors were created using a combination of Ohm’s and Poisseuille’s law discussed in section 5.1.1. With this simplification, the other noise parameter governed by an organ, i.e. the influence on the flow behaviour by the waste products present in the fluid in the circuit, has not been considered in the experimental model, as well as the compliance of an organ, excluding the consideration of a distinct characteristic feature of a real organ.

Finally, the fluid flowing through the setup has been replaced by water. In the influence analysis, the fluid component was shown to be completely controllable. It is therefore not necessary to change it because of uncontrollable noise parameters. However, previous tests showed that the unstable behaviour of the impeller was also observed for perfused water replacing perfusion medium or blood. The characteristics of water are more suitable for this fundamental research, because water cannot cause no clotting, has no cellular material, is a Newtonian fluid, and is easier accessible and replaceable than blood, it was used for the

planned tests. The replacement of the organ component by resistors with different resistances, allowed eliminating the influence of normothermic temperatures and hypothermic temperatures on the resistances. Therefore the fluid (water) has been kept at room temperature.

4.1.2 Simplifying assumptions for the numerical model

Similar to the experimental model, the numerical model also relies on simplifying assumptions, of another nature however. The assumptions have been made by setting model-specific boundary conditions that can represent the pump in its real application in the XVIVO perfusion device.

To simulate the linear dynamics, the numerical model of the pump was simplified to consist of only the rotating part the impeller and the ball bearing, and the axis and base the impeller is balancing on. The housing of the pump and the electromotor have been excluded from this model, as the vibrations of the pump have been observed to occur only in the internal pump components and therefore are assumed to occur only there. Thus, the numerical analysis is focused on estimating the dynamic characteristics of only the internal components of the pump. The base of the impeller has a fixed constraint boundary condition to simulate its connection to the housing of the pump and the electromotor. The magnetic force between the magnets present in the impeller and the magnets of the electromotor is excluded from these models, as this force does not influence the eigenfrequency values of the geometry. Therefore they are not assumed in the model. This means for the rotating impeller no boundary conditions are assumed. It is also assumed that the pump is in a vacuum instead of in a fluid.

For the CFD model, only the fluid inside the pump has been considered. The physical structure of the pump has been left out of the model, while the complex geometry is preserved through the geometry of the fluid. With this simplification, possible fluid-structure interactions (FSI) have been ignored and are therefore assumed to not have any influence on the fluid flow. The physical boundaries of the fluid are formed by the rotating impeller, the axis and base underneath the impeller and the housing of the pump from the pump inlet to the pump outlet, in order to only contain the fluid inside the pump. All boundaries have been assigned a boundary condition corresponding to their function. The fluid in other parts of the circuit have not directly been considered. Instead, the influence of the rest of the circuit on the pump has been simulated by applying boundary conditions to the inlet and outlet. Furthermore, no backflow was assumed.

Second, for the properties of the fluid it is assumed that the flow is a strictly incompressible flow. Furthermore the reference pressure level is assumed to be 1 atmosphere, and the reference and fluid temperature are set to 22 degrees Celsius (295.15 K). Further fluid properties are based on these reference parameters.

Third, the domain around the impeller has been considered as a rotating domain and has been discretized by its own rotating mesh. This rotating domain contains all of the space around, over, and underneath the impeller. It has been assumed that this entire space is influenced by the rotating of the boundaries resembling the impeller. As the exact influence of the rotating of the impeller on the rotation of the fluid is unknown, the rotating domain includes excess space above and below the impeller on which the rotating impeller possibly has less or no influence on in terms of direct rotation translation. The flow velocity and flow rate from the

simulation are therefore prone to turn out different than they would be in reality. However through this method the influence of the rotation of the impeller is believed to become more clear then if the influence on rotation would have been made lower. The outer boundaries of this domain is assumed to be a fixed wall, therefore not rotating along with the rest of the domain. These boundaries resemble the surface of the housing in contact with the fluid.

In accordance with the simplified assumptions made for the experimental model, for the numerical model a constant flow of water at room temperature has been considered. This has made it possible to compare the experimental results with the numerical simulation results. It furthermore has decreased the computational time of the simulation.

Lastly, experimental results from the experimental model for determining the performance of the centrifugal pump are used as input for the numerical model. These results are not obtained from the boundaries of the pump but have been obtained at a specific distance from the tubes connected to the inlet and outlet. It still has been assumed that these parameter values are equal to the parameter values at the inlet and outlet of the pump. It is also assumed that the input data obtained from the experiments are obtained correctly.

5. Materials/Methods

The triptych of research methods divided between the experimental and numerical fields have required a different setup.

5.1 Materials and methods for the Experimental Model

5.1.1 Materials

The performance test and the stability experiment require one setup, shown in figure 9. The setup consists of an XVIVO cirQlife centrifugal pump test sample (*A*, orange), a custom reservoir (dark blue), two pressure sensors (*P1* and *P2*, green), one flow sensor (*Q1*, light blue), a resistor (*R1*, purple), and tubing.

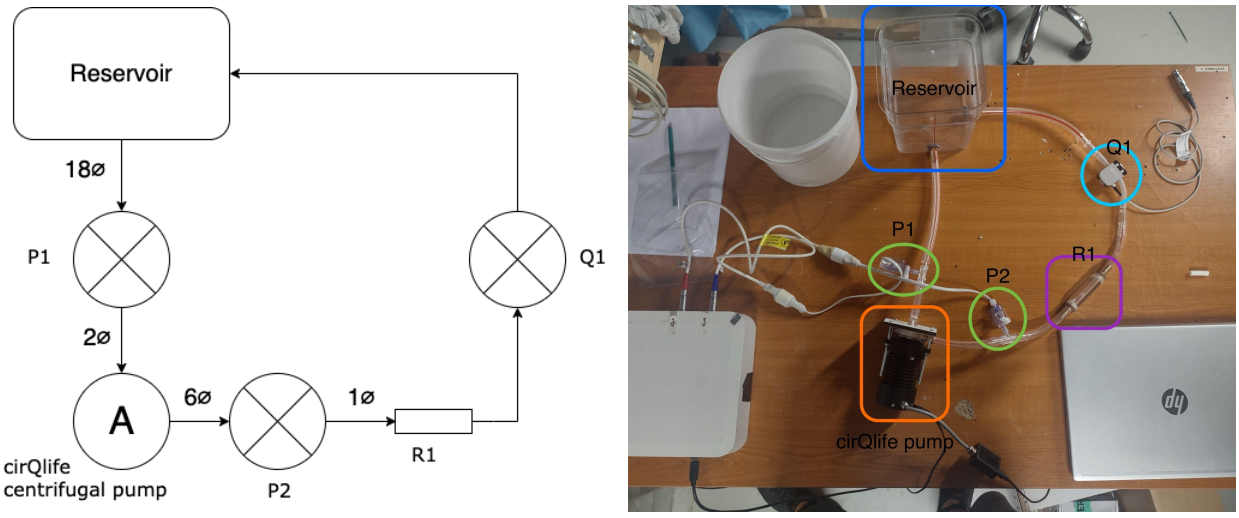

Figure 9. The experimental model setup. Left: schematic. Right: photograph. Blue = reservoir, green = pressure sensors, purple = resistor, light blue = flow sensor.

The XVIVO cirQlife pump samples, discussed thoroughly in the problem description in section 3.1, have been tested for two assembly methods: glued and clamped. The glued samples were conventional samples from the manufacturer. Therefore, from here they will be addressed as the reference group. The clamped samples were received in parts and manually clamped together. Both groups consisted of five samples. The reference samples were studied only in the performance test and stability experiment, while the clamped samples additionally were used to study the influence of the holes in the design of the impeller on the output parameters and the pump stability. Keeping the parts unassembled and mechanically clamping them during the experiments has allowed it to separate the parts in between experiments to alter the impeller design.

The main tubing used in the experimental model was 3/8'' ID x 3/32'' thickness PVC. Thus, the diameter of the main tube in the circuit is 0.9525 cm. The distances between the different setup components has been determined using literature to prevent turbulent flow from influencing pressure- and flow rate measurements. Therefore, the tubing is conformed to the nominal size of the test specimen connection and to specific length requirements, also shown in the schematics of figure 9, according to:

"The upstream pressure sensor shall be at least two nominal tube diameters (1.905 cm) from the test specimen connection, while the downstream pressure sensor must be at least six nominal tube diameters (5.715 cm) from the test specimen connection. Between the reservoir and pressure sensor P1 must be eighteen nominal tube diameters (17.145 cm) of straight tube. And between pressure sensor P2 and the reservoir should be at least one tube diameter (0.9525 cm) of straight tube."[22]

As *R1* is also present in the setup after *P2*, it was decided to have at least one nominal tube diameter between P2 and R1. The distance between *R1* and the reservoir was kept at least one nominal tube diameter.

Furthermore, the diameter of the tubing used in the circuit must be kept constant if possible. Due to the use of a flow sensor that is applicable only to 1/4''ID silicone tubing, the uniform diameter of tubes is not always possible. The specifications of the silicone tubing for the flow sensor are 1/4'' ID x 3/32'' thickness. Therefore, the diameter of this tubing is 0.635 cm. This means the maximum decrease in diameter between the largest and smallest diameter tubing is 33% and the largest diameter increase between the smallest and largest diameter tubing is 50%. To limit the influence of the changing diameter to the rest of the circuit, the silicone tubing was placed behind all other components. Any possible turbulent flow created by the change in diameter size, has therefore not influenced other components..

The reservoir functions as both the inlet and outlet of the circuit to create a circular system. In order to prevent a turbulent surge from the outlet directly to the inlet, the reservoir contains additional two litres of water. This volume prevents the fluid coming from the inlet to be directed immediately to the outlet. The inlet and outlet of the reservoir are oriented normally, further preventing a possible turbulent surge, at equal height, reducing the effect of different column pressures on the flow, and are of equal size to fit a 3/8'' ID tube. Finally, the reservoir is open to atmospheric pressure.

The two pressure sensors are Edwards TruWave disposable pressure transducers. They are connected to the circuit via an intermediate piece, perpendicular to the direction of the flow. On the other side they are connected to a transmission box connected to a laptop equipped with a custom java script. This script allows the pressure measurements to be displayed analogue and logged over time. *P1* in front of the pump measures the suction pressure, and *P2* behind the pump the discharge pressure. Pressure is displayed and stored in mmHg as this is the conventional unit used by the system. The pressure sensors are calibrated after the fluid has been added and the circuit has been deaerated. The script was calibrated, before the start of the tests.

For the flow sensor, an EM-TEC 1/4'' x 1/16'' Flow Sensor is used. As mentioned, this sensor is attached over a straight section of 1/4'' ID x 3/32'' thickness silicone tubing to measure flow rate through the tube. It is connected to the control unit of an Organ Assist module meant for experimental uses to digitally read out the measured value for the flow rate from the display and note them. The flow rate is measured in litres per minute, as this is the conventional unit used by this system. Calibration of the flow sensor has been done beforehand and is checked after the sensor was applied on the tube.

Five orifice resistors, *R1*, were designed (figure 10.) and manufactured (figure 11.) to mimic the flow resistance of an organ at normothermic and hypothermic temperatures. The resistances to three different flows through two different organs were mimicked by the resistors: the flow through a liver from the hepatic artery, through a liver from the portal vein, and through a kidney from the renal artery. The difference in resistance is created by varying the diameter of the narrowed part of the tube, labelled *ØD*.

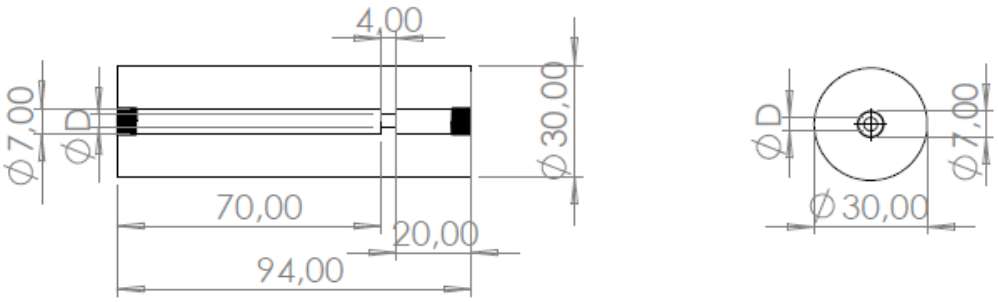

Figure 10. Technical drawing of the orifice resistor. Left: side view. Right: front view.

Figure 11. The set of five fabricated orifice resistors.

This hollow transparent cylinder contains hose barbs on both ends to connect to the tubes, shown in black in the schematics. To minimise possible turbulent behaviour, multiple actions were taken. The inside diameter of the cylinder and the hose barbs were matched (7 mm) to allow for a uniform diameter. The cylinder contains a narrowed part, with an inside diameter determined using the method explained below. The distance between the hose barb entrance and the narrowed part of the resistor is 7 cm. For the back end of the cylinder this distance is not needed as the flow behaviour is not important after the resistor.

To determine the dimensions of the narrowed part of the resistor, a combination of Ohm's law and Poiseuille's law was used, as shown in figure 12. First, Ohm's law for electrical circuits was represented in the fluid domain as flow rate Q through a pipe in terms of pressure difference ΔP over flow resistance R. Subsequently, the flow resistance of the pipe has been rewritten in terms of viscosity η, pipe length l and pipe radius r, i.e. the dimensions of the narrowed part:

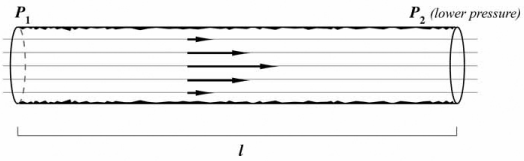

$$I = \frac{V}{R}$$ Ohm's Law

$$Q = \frac{\Delta P}{R}$$ Fluid Flow

$$Q = \frac{\Delta P \, \pi \, r^4}{8 \, \eta \, l}$$

$$R = \frac{8 \, \eta \, l}{\pi \, r^4}$$ Flow Resistance

Figure 12. The relation between Ohm's law for resistance in electrical circuits and Poiseuille's law for vascular resistance.

Inside the human body, the resistance of the liver to blood flow is extremely low with the maximum pressure gradients between the portal venous inflow and hepatic venous outflow *ΔP*

= 5 mmHg and the portal venous inflow of 840 mL/min. The resistance of the liver between the hepatic artery and the hepatic vein is much higher with the mean pressure gradient ΔP = 85 mmHg and the hepatic artery inflow of 360 mL/min. For other organs the pressure gradient across all other organs is in the range of *ΔP* = 115 mmHg and a lower inflow (500 mL/min for one kidney) also leads to a much higher resistance of these organs.[23, 24, 25]

In both HMP and NMP the medium inflow and pressure gradient over a liver or kidney are different from the *in vivo* situation and vary in the experiments. The literature indicates average resistances for different organ setups provided in Table 1. together with the dimensions of the narrowed part required to mimic the resistance of a specific organ. For the resistance of a liver for blood flow through the portal vein during NMP, no dimensions could be determined as this resistance is too low.

Table 1. Flow resistances during NMP and HMP through the liver and kidney with corresponding orifice resistor dimensions.

Organ	Resistor #	Resistance (R) [mmHg min/mL]	Length (l) [mm]	Radius (r) [mm]
Liver - Portal Vein NMP [5,26-29]	N.A.	0.01	N.A.	N.A.
Liver - Hepatic Artery NMP [5,26-29]	R2	0.15	4.0	2.8 (2.778)
Kidney - NMP [30-33]	R3	0.21	4.0	2.6 (2.553)
Liver - Portal Vein HMP [34-40]	R1	0.08	4.0	3.3 (3.251)
Liver - Hepatic Artery HMP [34-40]	R5	0.69	4.0	1.9 (1.897)
Kidney - HMP [30,41-43]	R4	0.39	4.0	2.2 (2.188)

5.1.2 Methods

5.1.2.1 Methods Performance test

The performance of the pump has been measured in terms of flow rate, suction pressure, and discharge pressure for multiple rotational speeds and multiple resistances. The rotational speed has been varied from 3500 RPM to 6500 RPM with a step size of 500 RPM for each resistor. At each rotational speed all parameter values have been noted in an MS Excel® sheet in a table setup like table 2. The experiments were repeated for 10 pump samples.

5.1.2.2 Stability experiment

The stability of the pump was observed and mapped in terms of stability regimes for multiple rotational speeds and multiple resistances. The rotational speed was varied from 3500 RPM to 6500 RPM with a step size of 500 RPM for all five resistors. During the experiment the stability of the impeller was examined and qualitatively determined based on the visual and

aural observation of the impeller. For this, five possible regimes are specified based on visual and aural observations of the impeller:

1 = stable: the impeller remains fixed on the axis and does not wiggle; no additional sounds are perceived.

2 = minor instability: the impeller remains fixed on the axis, but wiggles; no additional sounds are perceived.

3 = major instability: the impeller remains fixed on the axis, but wiggles; additional sounds are perceived.

4 = critical instability: the impeller lifts off the axis and wiggles, additional sounds are perceived.

5 = desynchronization: the impeller becomes out of sync with the electromotor.

For each resistor at each rotational speed the observed stability regime was recorded in an MS Excel® sheet in a table setup like table 2. The experiment was repeated for 10 pump samples.

Table 2. Combined measurement table for the performance test and stability experiment.

Resistor:							
Rotational speed of cirQlife pump [RPM]	3500	4000	4500	5000	5500	6000	6500
Q1 [L/min]							
P1 (suction pressure) [mmHg]							
P2 (discharge pressure) [mmHg]							
H Pressure Head (m)							
Stability observation (1/2/3/4/5)							

5.1.2.3 Designing experiment conditions

The results for the influence analysis were used to design the experiment conditions. It was decided to nullify the noise effect of anomalies in the pump head samples by repeating the experiments for ten newly fabricated pump head samples. The experiments were performed at room temperature (the measured 22 degrees Celsius) at the same atmospheric pressure and environmental conditions in the lab. Furthermore, to nullify the effect of testing time and to prevent deformities and overtime wear for each pump to influence the results, the testing scheme for each pump is different, as shown in table 3.

The set of five glued pump samples is labelled by 1-5. The set of five clamped pump samples is labelled by A-E. Figure 13. Illustrates the clamping of the pump samples. The clamping mechanism includes a cut-out wooden plank, with one larger hole for the inlet of the

pump and four smaller holes for four bolts. The location of these holes corresponds to that of the holes present in the XVIVO cirQlife electromotor. They were tightened to the electromotor using nuts.

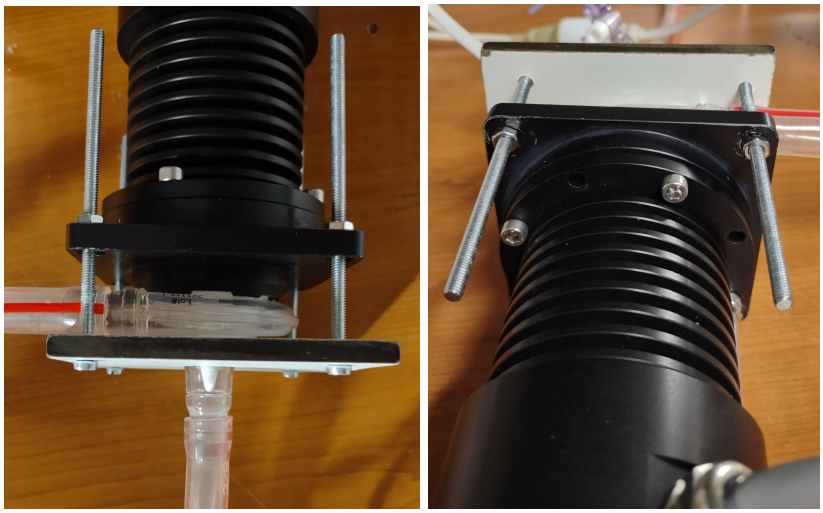

Figure 13. Clamp setup holding the clamped pump samples to the electromotor.

Table 3. Resistor testing scheme.

Pump #	Test run 1	Test run 2	Test run 3	Test run 4	Test run 5
1; A	R1	R2	R3	R4	R5
2; B	R2	R3	R4	R5	R1
3; C	R3	R4	R5	R1	R2
4; D	R4	R5	R1	R2	R3
5; E	R5	R1	R2	R3	R4

5.1.2.4 Design Alterations

After performing the performance test and stability experiment for the reference group and clamped group, the group of clamped pumps was used to study the influence of the holes present in the shaft of the impeller. After the first set of experiments the design of these samples was changed by closing the holes with a silicone kit. Afterwards, the experiments were repeated with the altered sample design using the same setup as discussed in 5.1.2.1 and 5.1.2.2 to enable a paired comparison between the two designs. The same resistor scheme was used for these samples. The results were recorded in an MS Excel® sheet in a table setup like table 2. The altered impeller design pumps are labelled pump A*-E* as a counterpart to pump samples A-E.

5.1.2.5 Data processing

After performing the experiments on all the samples, the results were grouped and analysed statistically to determine the mean output values of the pump, identify possible outliers, and study the differences between the conventional design group and the clamped design group, as well as between the clamped design group and the altered design group. Next, the output parameters were used to determine and display the characteristic Q-H curves for each operational setting. The results from the stability data were statistically analysed and then averaged for each rotational velocity for each resistor.

5.2 Materials and methods for the numerical models

5.2.1 Materials

The numerical models have been created using the commercially available software COMSOL Multiphysics®. The model used to compute the eigenfrequencies and corresponding mode shapes of the centrifugal pump utilises the Solid Mechanics module within the branch module Structural Mechanics. The model used to compute the internal flow behaviour of the centrifugal pump utilises the CFD module within the module branch Fluid Flow & Heat Transfer to model an internal single-phase flow rotating machinery.

5.2.2 Methods

5.2.2.1 Eigenfrequency model

The model used to simulate the eigenfrequencies of the impeller in 2D and 3D is shown in figure 14. The instructions for setting up this model have been included in the appendix, section 9.1 and section 9.2, respectively, together with more figures of the models.

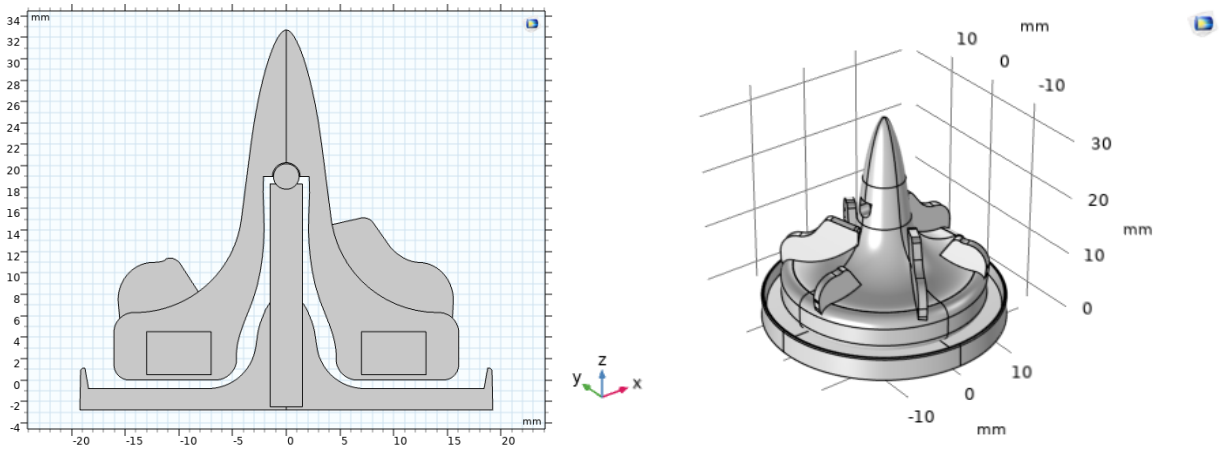

Figure 14. 2D & 3D CAD model of the centrifugal pump impeller. Left: 2D model. Right: 3D model.

All domains have been assigned their material including their material properties relevant for the eigenfrequency analysis, shown in table 4.

Table 4. Model components and material properties.[44-48]

Material	Domains	Modulus of Elasticity E [N/m^2]	Poisson's ratio λ [-]	Density ρ [kg/m^3]
ABS	Impeller, Axis, Base	1.79e9	0.35	1050
S06x04Ni-N45	Magnets	152e9	0.24	7500
Nylon	Ball	1.59e9	0.39	1150

In both models, the connection between the geometries representing the impeller, the magnets and the ball bearing was modelled by including all parts in the same union. The same method was used to model the connection between the axis and the base. These unions are kept separate by modelling them as an assembly.

The axis and base union were assigned a fixed domain constraint to model the rigid connection of the parts to the rest of the pump and the electromotor. The other union is considered free, and does therefore only own default boundary conditions, as these parts are not connected or influenced by any other part. The mesh settings were set to a physics-controlled, fine element size mesh. An eigenfrequency analysis was performed using the eigenfrequency solver ARPACK. The desired number of eigenfrequencies has been set to 60 starting from around 1 Hz.

5.2.2.2 CFD model

The model used to simulate the internal flow behaviour using CFD is shown in figure 15. The instructions for setting up this model have been included in the appendix, section 9.3, together with more figures of the model.

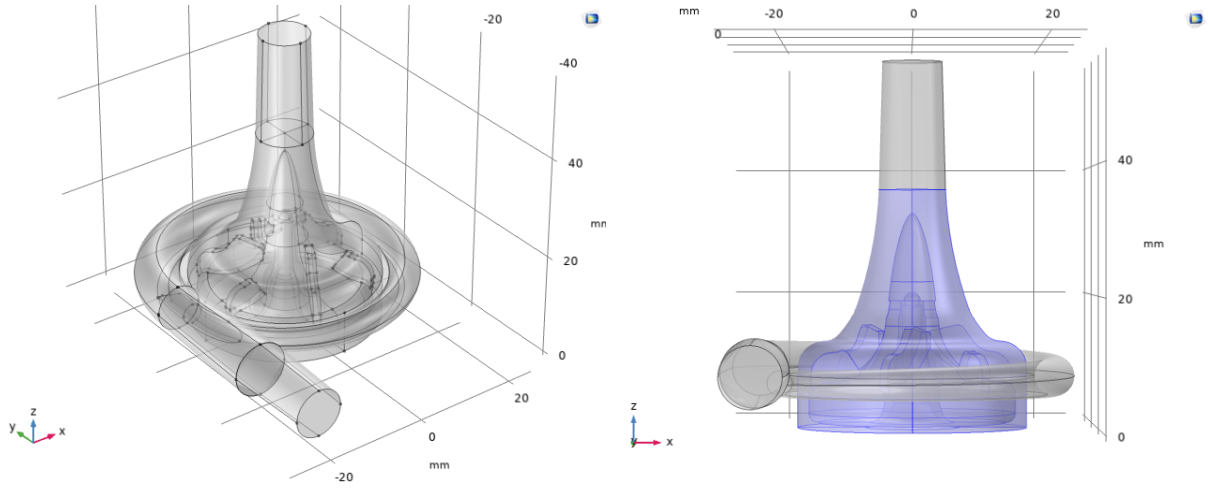

Figure 15. 3D model geometry of the fluid domain inside the pump. Left: overview. Right: front view with highlighted domain around the impeller.

This model has been used to simulate the internal flow behaviour of the pump at a set rotational speed using the output parameters obtained from the performance test for a resistor

mimicking the resistance to blood flow through the liver from the portal vein (diameter 6.6). The parameters that correspond to this are shown in table 5.

Table 5. Global parameters of the CFD model.

Parameter	Value (open holes)	Value (closed holes)	Description
p_tot_in	-38.80[mmHg]	-38.80[mmHg]	Total pressure at inlet
p_tot_out	124.70[mmHg]	123.80[mmHg]	Total pressure at outlet
rot_rpm	4000[RPM]		Rotational speed
T_ref	22[degC]		Reference temperature

To model the flow through the pump, the two-equation turbulence k-ω model was used as an approximation for the Reynolds-averaged Navier–Stokes equations (RANS equations). Here, the simplified assumptions for incompressible flow, T_ref as the reference temperature and the 1 atmosphere as the reference pressure level were implemented. As the model is meant to simulate the fluid inside the pump, all domains were assigned the materials properties of water. All fluid properties of water have been determined by the model parameters.

The inlet and outlet were assigned the Inlet and Outlet boundary conditions, respectively. These boundary conditions were set to assume fully developed flows and defined by the average pressure with parameters p_tot_in and p_tot_out to define the Inlet and Outlet, respectively.

A second Wall boundary condition was used to define the outer boundary of the rotating domain around the impeller as a fixed wall, with zero translational velocity. In order to simulate the rotation of the pump during operation, the domain around the impeller, highlighted in the right pane of figure 15. was assigned the Rotating Domain selection. The expression for the rotational velocity was set to use the general revolutions per time, given by parameter rot_rpm.

The geometry was specified by a set of definitions, including the list of expressions for variables regarding the pump's performance, given in table 18. included in the appendix, section 9.4. These include static pressure (Δp) total pressure increase (Δp_tot), torque (T), shaft power consumption (W), flow rate (Q), mass flow (μ), power given to the fluid (HP), pressure head of the pump (H) and pump efficiency (η). Furthermore, boundary probes to calculate the change in fluid density were placed at the inlet and outlet together with average probes. Integration probes for the impeller, inlet and outlet were also defined.

A physics-controlled mesh with extremely coarse element size was used to reduce computation times as much as possible, as the complexity of the model results in expensive computations requiring much computation power and time. After successful simulation of the model, this mesh was manually refined by halving the maximum mesh size in order to grade the quality of the initial simulation and study if the model is able to converge towards the solution obtained from the performance test.

The fluid inside the pump was simulated using the Frozen Rotor with Initialization study of COMSOL. This has decreased the computation time significantly to a time dependent CFD study. Using the parameter values in table 5., the internal flow behaviour at 4000 RPM was

simulated, i.e. in the stable regime of the pump. Subsequently, an auxiliary sweep was performed to simulate and compare the simulations of the pump at the different rotational speeds used in the performance test, where both stable and unstable behaviour was observed.

The influence of the holes on the internal flow behaviour of the pump at 4000 RPM was studied by removing the holes from the geometry in the simulation and using the experimental output parameters from the closed impeller experiment as input parameters for this model, as shown in table 5. An auxiliary sweep was performed to simulate and compare the results for the pump at different stable and unstable situations in the performance test. The outcomes of this simulation were compared to the outcomes of the simulations of the conventional design.

6. Results

The obtained results are presented in order of RSQs. First, the eigenfrequency analysis was performed. Next, the performance test and stability experiment were carried out for both the conventional impeller design and the closed impeller design. Finally, the CFD analysis was performed using the experimental results as inputs, first for the conventional impeller design and subsequently for the closed impeller design.

6.1 Eigenfrequency model results

6.1.1 Eigenfrequencies 2D model

Table 6. List of the first six values simulated for the eigenfrequencies of the 2D model.

Eigenfrequency (Hz)	Angular frequency (rad/s)
204.56	1285.3
220.38	1384.7
2387.4	15001
3107.7	19526
4087.2	25681
7109.4	44670

6.1.2 Mode Shapes 2D model

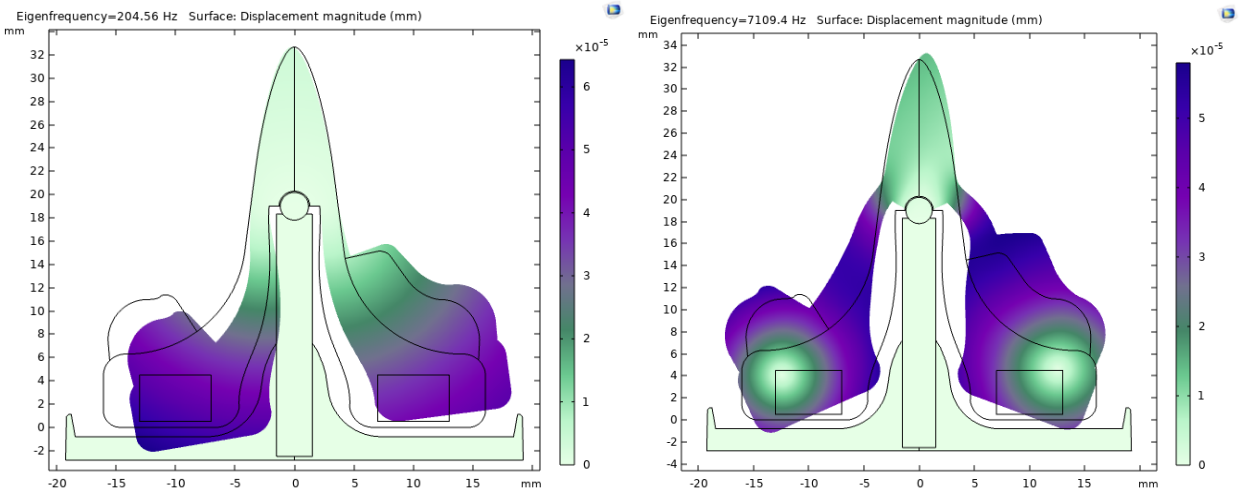

Figure 16. Mode shapes of the model corresponding to the first and sixth simulated eigenfrequencies. Left: mode shape at 204.56 Hz. Right: mode shape at 7109.4 Hz.

6.1.3 Eigenfrequencies 3D model

Table 7. Value seven to twelve simulated for the eigenfrequencies of the 3D model.

Eigenfrequency (Hz)	Angular frequency (rad/s)
5207.9	32722
5667.3	3.56E+04
7139.5	4.49E+04
8993.7	5.65E+04
12033	7.56E+04
12090	7.60E+04

6.1.4 Mode Shapes 3D model

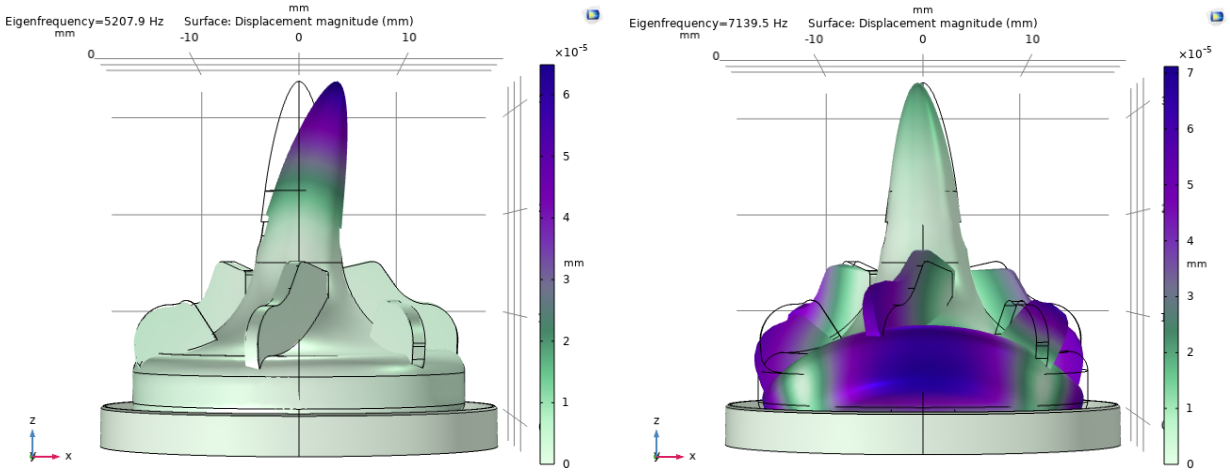

Figure 17. Mode shapes of the model corresponding to simulated eigenfrequency seven and nine. Left: mode shape at 5207.9 Hz. Right: mode shape at 7139.5 Hz.

6.2 Performance test and stability experiment results

6.2.1 Mean output parameters: pressure difference and flow rate

The results used to plot the figures are included in the appendix, section 9.7, in table 21.-25. for the reference group and clamped group. For the experimental group this is section 9.9, in table 27.-31.

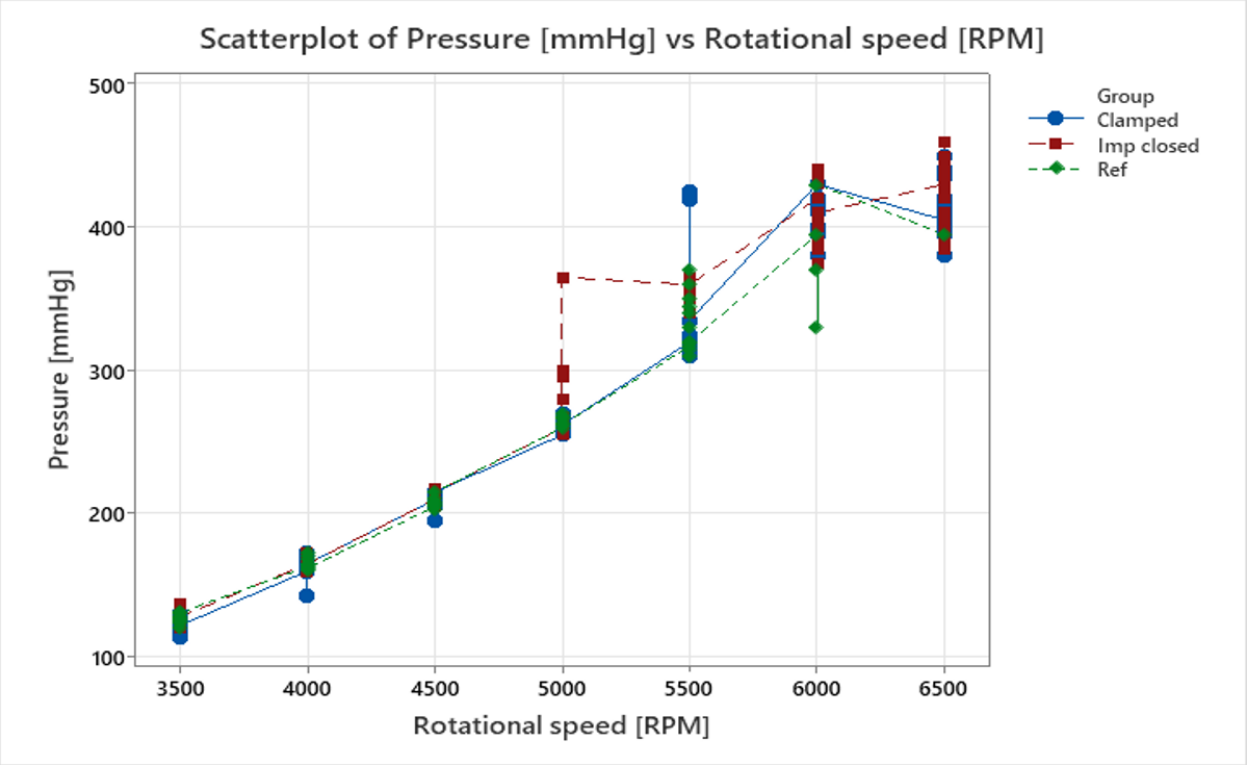

Figure 18. Scatter plot of the pressure difference vs rotational speed of all three sample groups for all resistances and all rotational speeds.

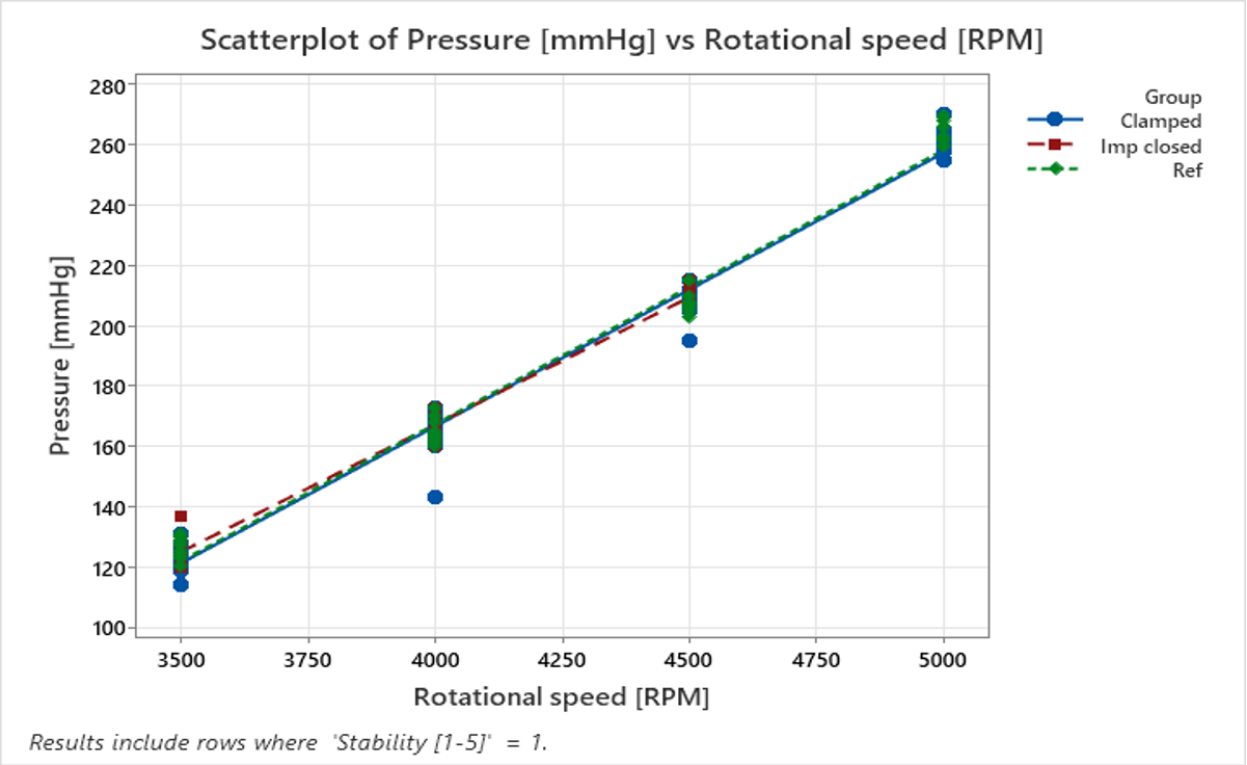

Figure 19. Scatter plot of the pressure difference vs rotational speed of all three sample groups for all resistors and all rotational speeds, only including results for which the stability regime was ‘stable’ (1).

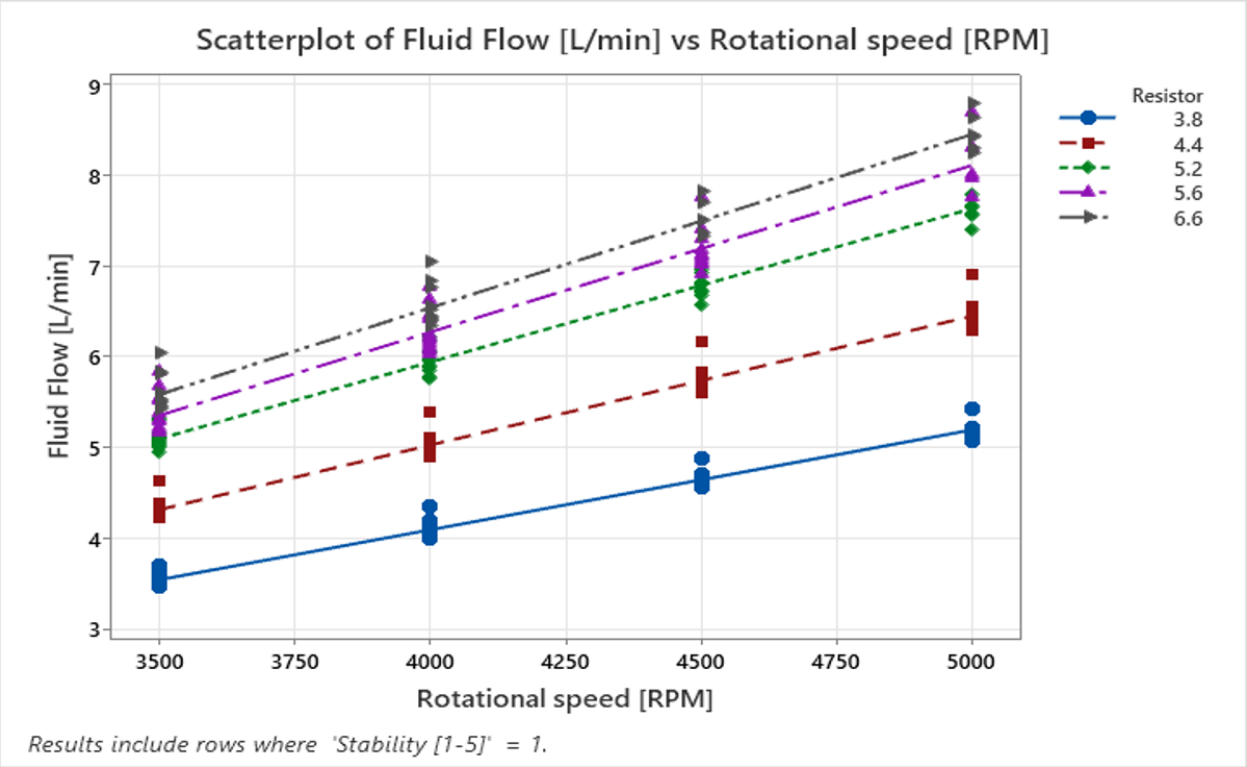

Figure 20. Scatter plot of the flow rate vs rotational speed of all three sample groups only including rotational speeds for which the stability regime was ‘stable’ (1).

6.2.2 Q-H curves

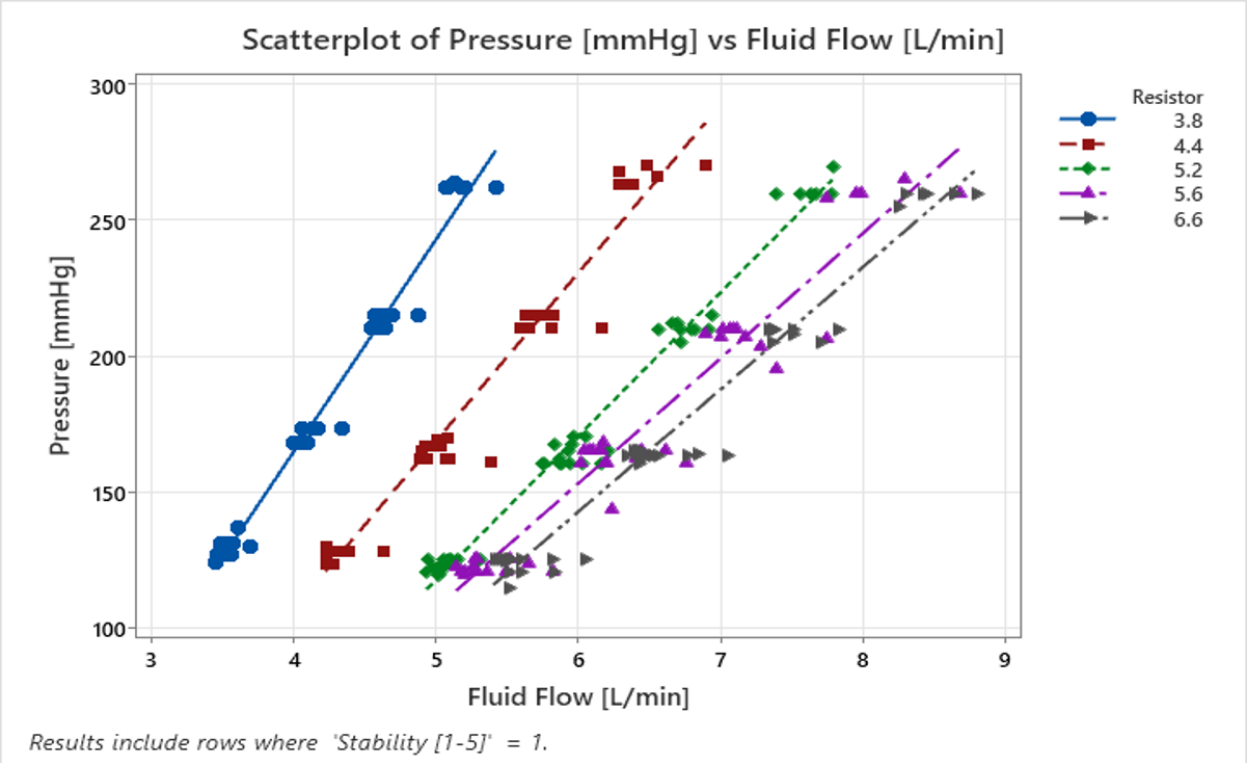

Figure 21. Scatter plot of the pressure difference [mmHg] vs fluid flow [L/min]. The mean Q-H curves drawn for every resistor only including rotational speeds for which the stability regime was ‘stable’ (1).

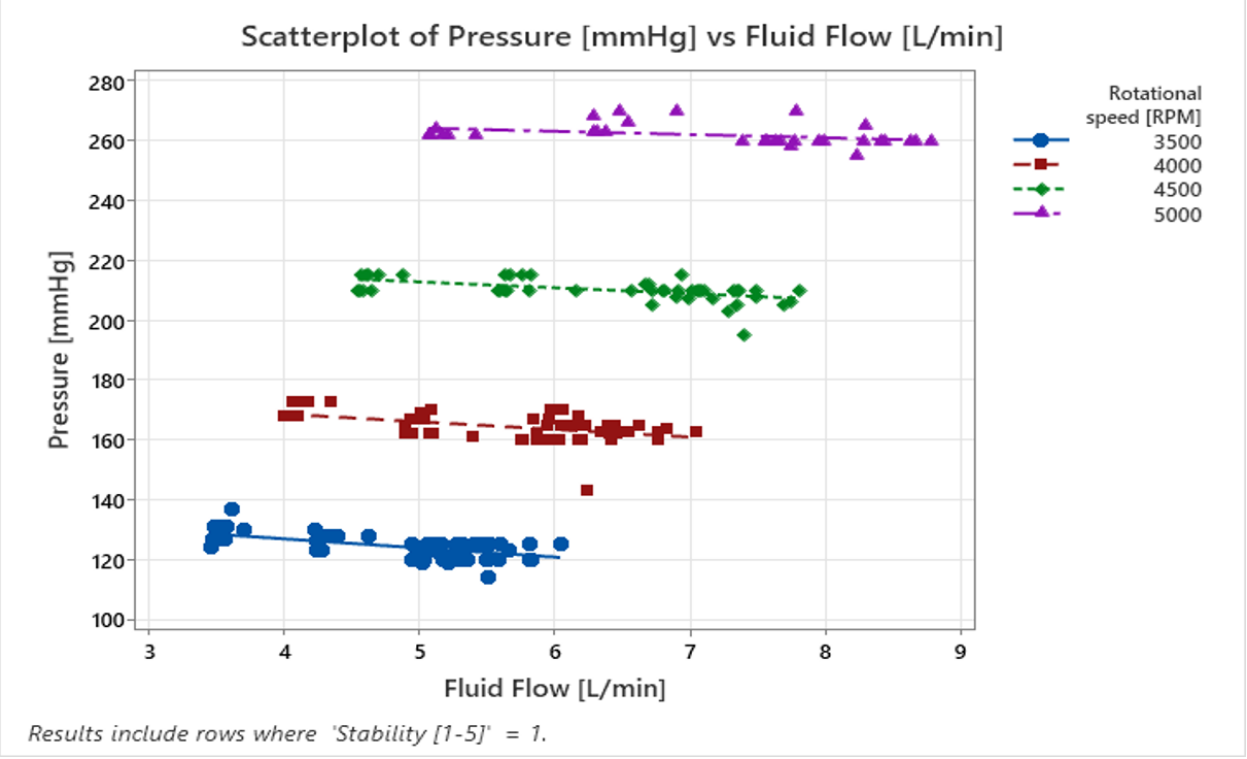

Figure 22. Scatter plot of the pressure difference [mmHg] vs fluid flow [L/min]. The mean Q-H curves drawn for every RPM, only including rotational speeds for which the stability regime was ‘stable’ (1).

6.2.3 Stability regime results per rotational speed

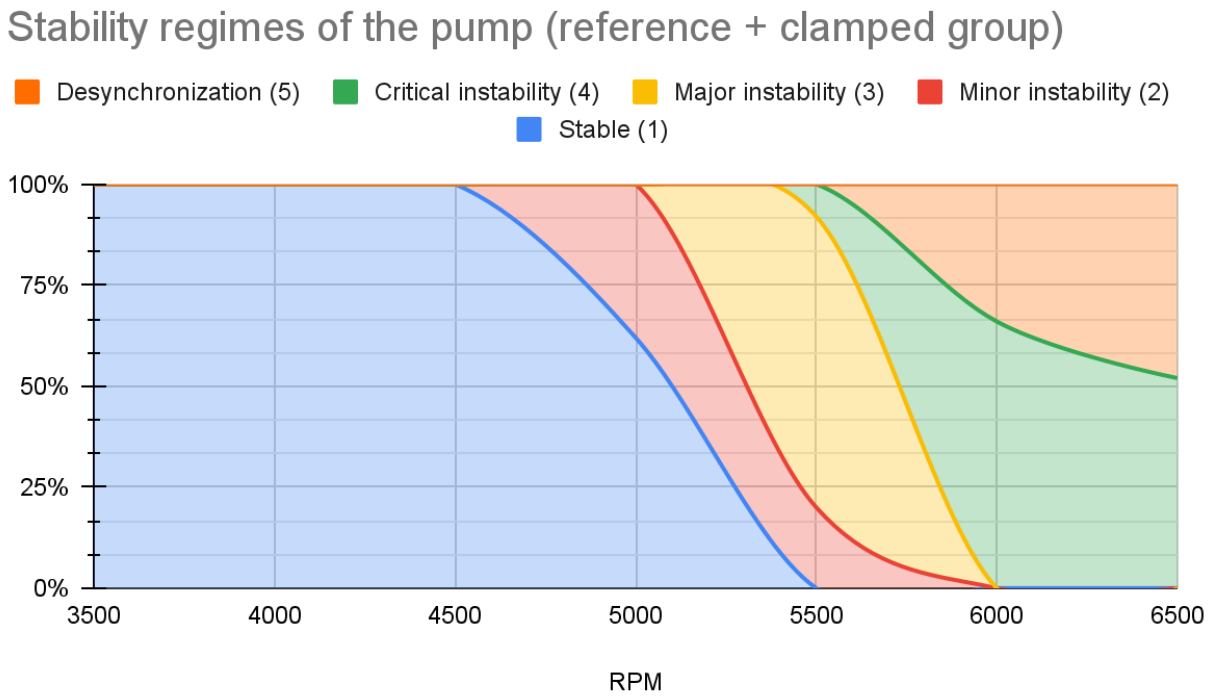

Figure 23. 100% stacked area chart of the mean stability regime graph of pump samples 1-5 and A-E.

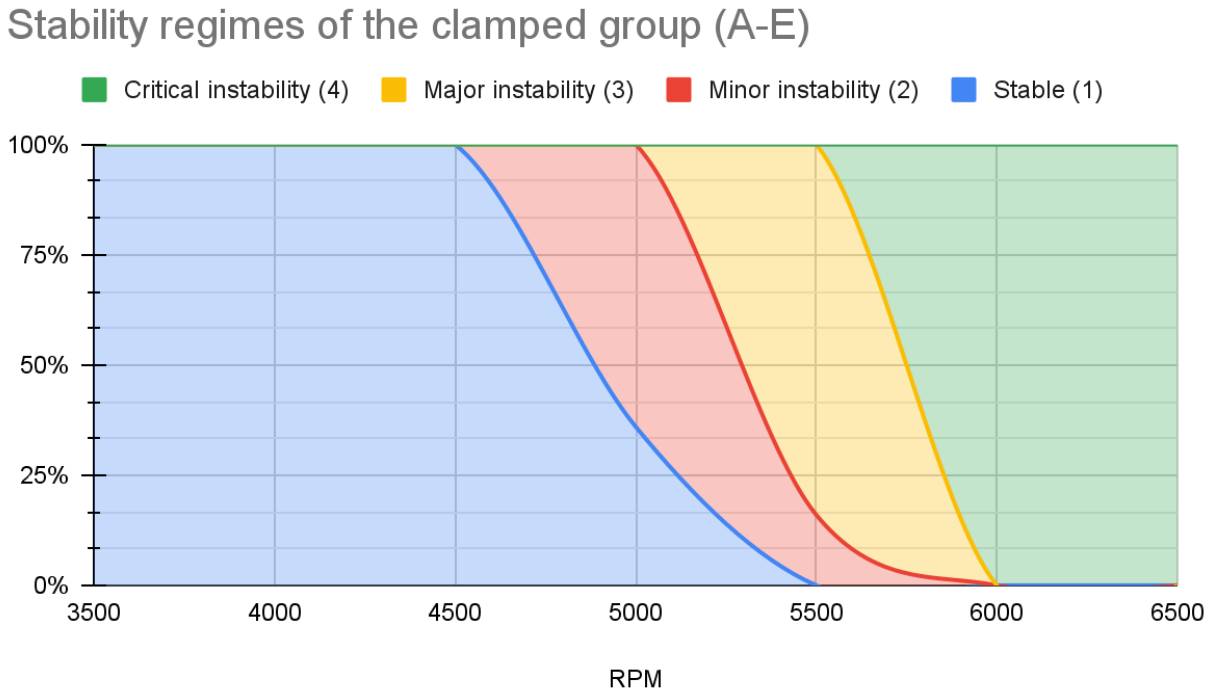

Figure 24. Mean stability regime graph for pump samples A-E.

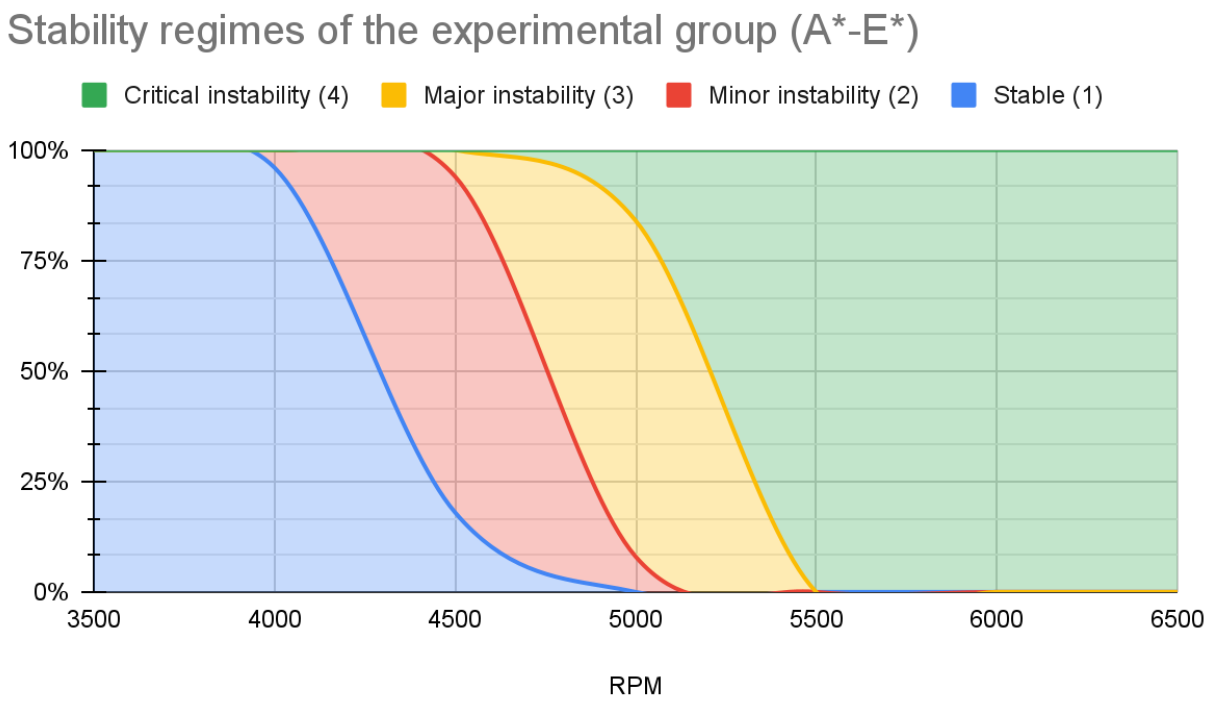

Figure 25. Mean stability regime graph of pump samples A*-E*.

6.3 CFD model results

6.3.1 CFD analysis of the conventional impeller pump model

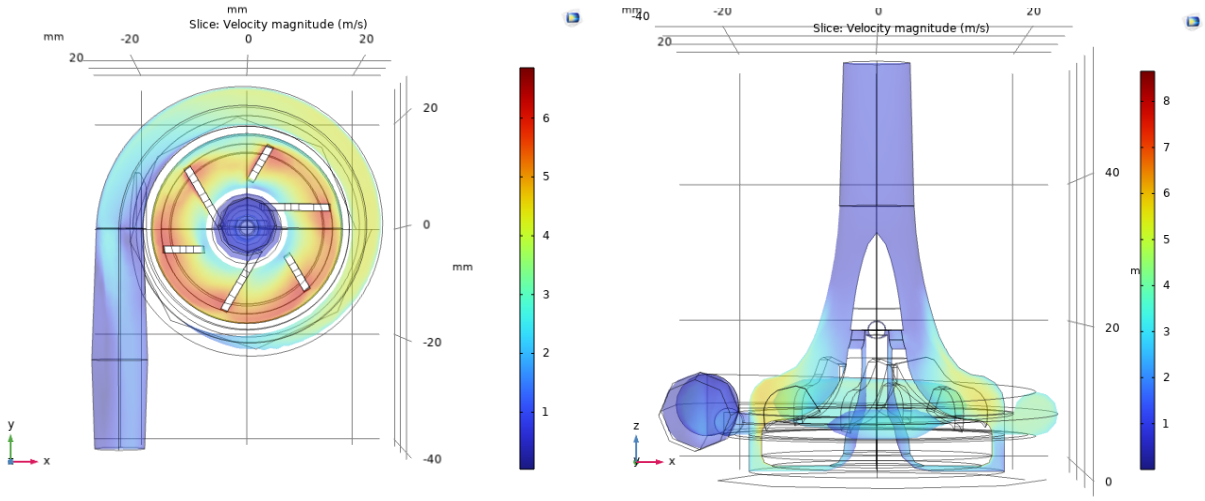

Figure 26. Velocity of fluid in the pump model at 4000 RPM. Left: top view, horizontal cross-section. Right: front view, vertical cross-section.

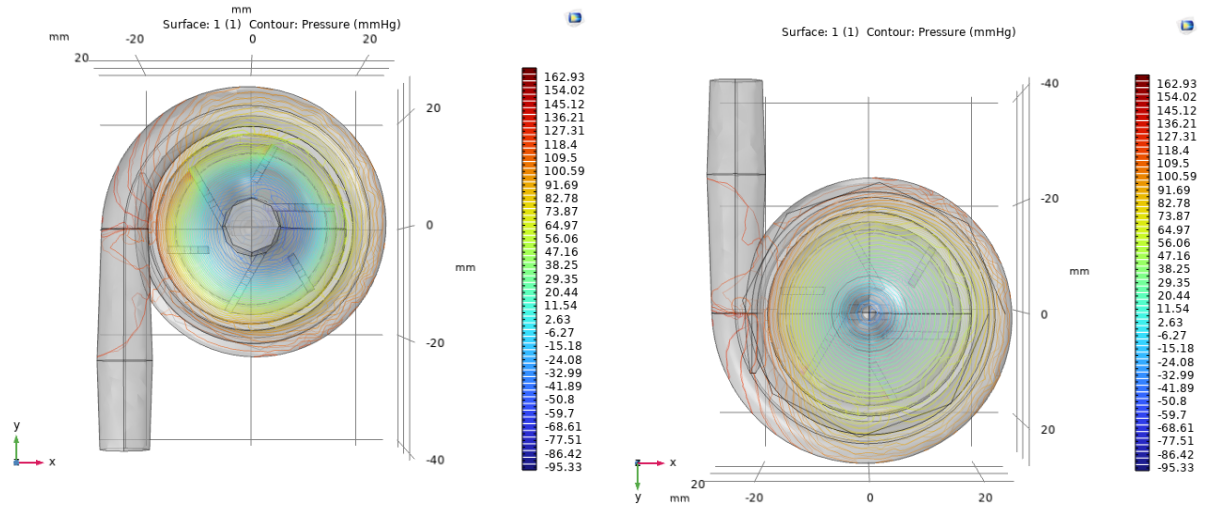

Figure 27. Pressure distribution of the fluid in the pump model at 4000 RPM. Left: top view. Right: bottom view.

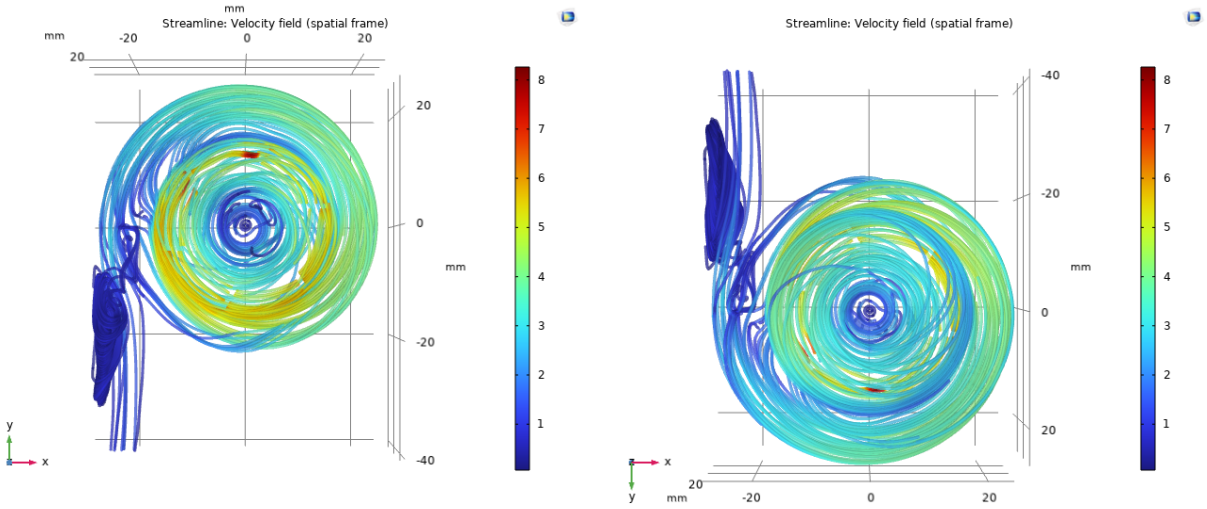

Figure 28. Velocity streamlines of the fluid in the pump model at 4000 RPM. Left: top view. Right: bottom view.

Table 8. Simulated inlet and outlet parameters of the pump model at 4000 RPM.

	Initial mesh	Mesh refinement #1	Mesh refinement #2
Average Inlet flow rate [L/min]	2.910	2.960	2.593
Average inlet pressure [mmHg]	-38.801	-38.801	-38.800
Average outlet flow rate [L/min]	2.910	2.960	2.593
Average outlet pressure [mmHg]	124.70	124.70	124.70

Table 9. Simulated performance parameters of the pump model for at 4000 RPM.

Parameter	Initial mesh	Mesh refinement #1	Mesh refinement #2
Δp [mmHg]	161.16	161.13	161.00
Δp_tot [mmHg]	162.64	162.64	162.55
Torque [N*m]	-0.011	-0.010	-0.010
Shaft Power Consumption [N*m/s]	4.404	4.384	4.264
Power given to fluid [N*m/s]	1.067	1.070	0.937
Pump efficiency [1]	0.242	0.244	0.220
Head [m]	2.216	2.216	2.215
Flow rate [L/min]	2.954	2.960	2.593

Table 10. Simulated inlet and outlet parameters of the pump model through an auxiliary sweep for different rotational speeds.

Rotational speed [RPM]	3500	4000	4500	5000	5500	6000
Average Inlet flow rate [L/min]	2.839	2.911	3.268	3.767	3.645	-9.734
Average inlet pressure [mmHg]	-28.800	-38.800	-48.800	-60.000	-75.500	-98.00
Average outlet flow rate [L/min]	2.839	2.911	3.268	3.797	3.645	-9.734
Average outlet pressure [mmHg]	93.50	124.70	160.00	199.00	243.50	306.00

Table 11. Simulated performance parameters of the pump model for different rotational velocities.

Rotational speed [RPM]	3500	4000	4500	5000	5500	6000
Δp [mmHg]	120.61	161.17	205.79	255.32	314.32	451.202
Δp_tot [mmHg]	121.74	162.62	207.70	257.74	317.24	442.30
Torque [N*m]	-0.008	-0.010	-0.013	-0.016	-0.020	-0.011
Shaft Power Consumption [N*m/s]	2.976	4.393	6.258	8.632	11.377	6.638
Power given to fluid [N*m/s]	0.768	1.052	1.508	2.175	2.569	9.566
Pump efficiency [1]	0.258	0.239	0.241	0.252	0.226	1.441
Head [m]	1.659	2.216	2.830	3.512	4.323	6.027

Flow rate [L/min]	2.839	2.911	3.268	3.797	3.645	-9.734

6.3.2 CFD analysis of the closed hole impeller pump model

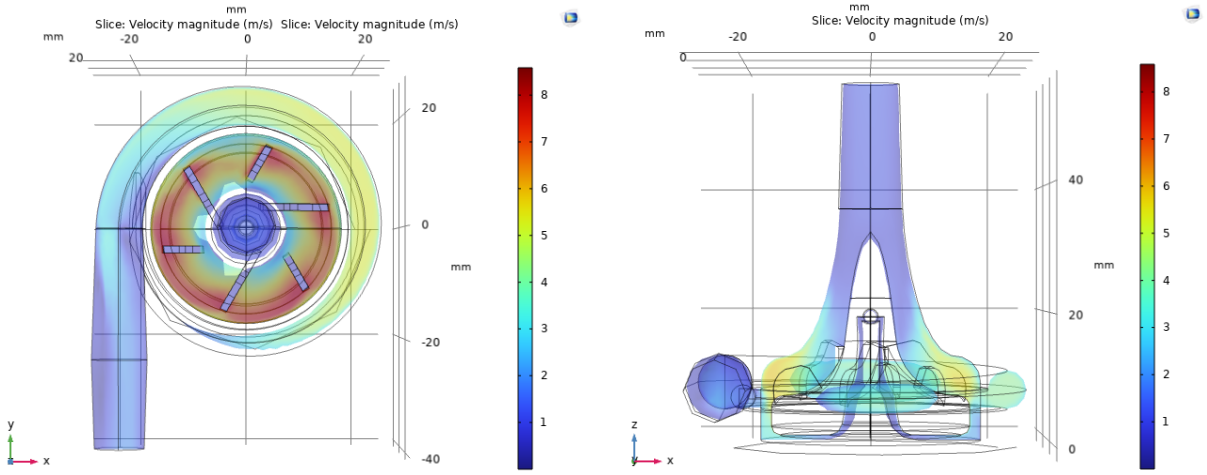

Figure 29. Velocity of fluid in the closed impeller pump model at 4000 RPM. Left: top view, horizontal cross-section. Right: front view, vertical cross-section.

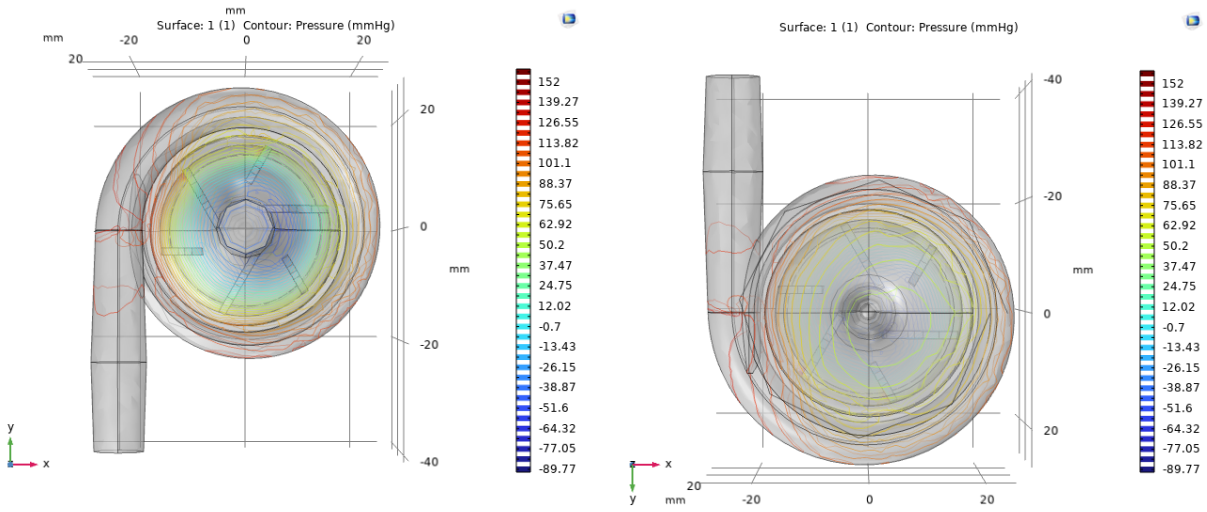

Figure 30. Pressure of the fluid in the closed impeller pump model at 4000 RPM. Left: top view. Right: bottom view.

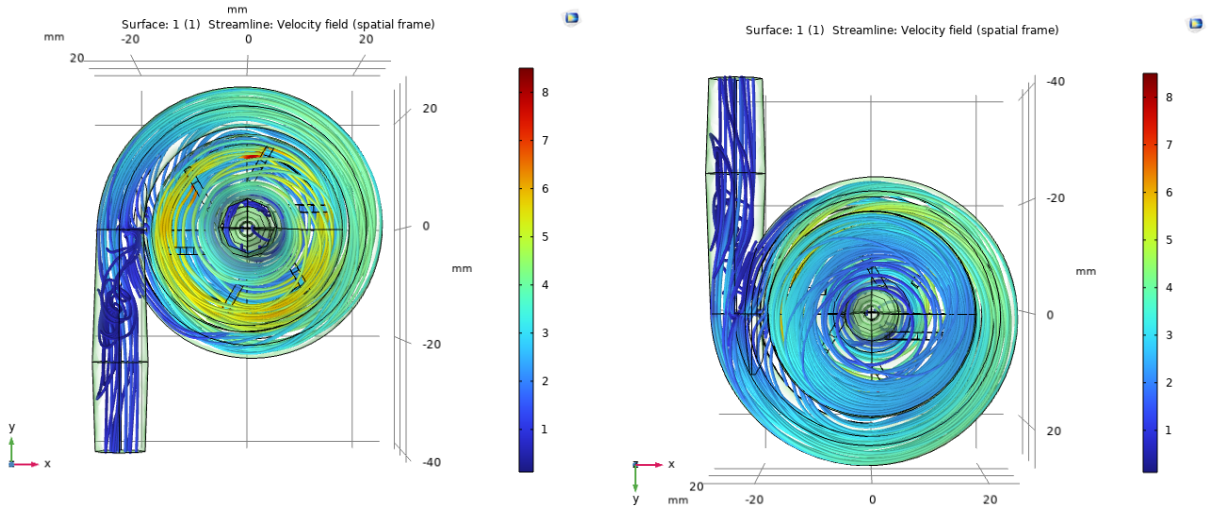

Figure 31. Velocity streamlines of the fluid in the closed impeller pump model at 4000 RPM. Left: top view. Right: bottom view.

Table 12. Simulated inlet and outlet parameters of the closed impeller pump model at 4000 RPM.

Average Inlet flow rate [L/min]	3.414
Average inlet pressure [mmHg]	-38.800
Average outlet flow rate [L/min]	3.414
Average outlet pressure [mmHg]	123.80

Table 13. Simulated performance parameters of the closed impeller pump model for at 4000 RPM.

Parameter	Value
Δp [mmHg]	160.37
Δp_tot [mmHg]	161.95
Torque [N*m]	-0.010
Shaft Power Consumption [N*m/s]	4.260
Power given to fluid [N*m/s]	1.228
Pump efficiency [1]	0.288
Head [m]	2.207
Flow rate [L/min]	3.414

Table 14. Simulated inlet and outlet parameters of the closed impeller pump model for different rotational speeds.

Rotational speed [RPM]	3500	4000	4500	5000	5500	6000
Average Inlet flow rate [L/min]	2.651	3.413	3.706	4.177	0.709	2.208
Average inlet pressure [mmHg]	-30.00	-38.80	-48.60	-60.00	-81.00	-96.00
Average outlet flow rate [L/min]	2.651	3.413	3.706	4.177	0.709	2.208
Average outlet pressure [mmHg]	95.00	123.80	160.00	199.00	272.00	307.00

Table 15. Simulated performance parameters of the closed impeller pump model for different rotational velocities.

Rotational speed [RPM]	3500	4000	4500	5000	5500	6000
Δp [mmHg]	123.32	160.38	205.72	255.46	353.77	399.27
Δp_tot [mmHg]	124.42	161.97	207.74	258.03	352.54	401.67
Torque [N*m]	-0.008	-0.010	-0.013	-0.016	-0.017	-0.021
Shaft Power Consumption [N*m/s]	2.797	4.259	6.030	8.276	10.007	13.246
Power given to fluid [N*m/s]	0.733	1.228	1.711	2.395	0.555	1.971
Pump efficiency [1]	0.262	0.288	0.284	0.289	0.055	0.149
Head [m]	1.695	2.207	2.831	3.516	4.804	5.473
Flow rate [L/min]	2.651	3.413	3.706	4.177	0.709	2.208

6.3.3 Calculations on the balance of forces

Table 16. Balance of axial forces of the conventional impeller in the pump for all rotational speeds.

Force	3500 RPM	4000 RPM	4500 RPM	5000 RPM	5500 RPM	6000 RPM	6500 RPM
F(s)	-3.107 N	-4.186 N	-5.265 N	-6.474 N	-8.146 N	-10.574 N	-10.574 N
F(d)	9.245 N	12.330 N	15.820 N	19.677 N	24.077 N	30.257 N	30.257 N
F(mag)	-21.263 N						

F(J)	-0.121 N	-0.165 N	-0.217 N	-0.273 N	-0.340 N	-0.418 N	-0.421 N
F(Wd)	-0.115 N	-0.154 N	-0.197 N	-0.244 N	-0.301 N	-0.381 N	-0.381 N
F	-8.905 N	-5.066 N	-0.592 N	4.371 N	10.319 N	18.769 N	18.766 N

Table 17. Balance of axial forces of the experimental impeller in the pump for all rotational speeds.

Force	3500 RPM	4000 RPM	4500 RPM	5000 RPM	5500 RPM	6000 RPM	6500 RPM
F(s)	-3.237 N	-4.186 N	-5.244 N	-6.474 N	-8.740 N	-10.358 N	-10.574 N
F(d)	10.250 N	13.357 N	17.263 N	21.471 N	29.348 N	33.124 N	33.340 N
F(mag)	-21.263 N						
F(J)	-0.118 N	-0.162 N	-0.212 N	-0.269 N	-0.375 N	-0.420 N	-0.421 N
F(Wd)	-0.118 N	-0.153 N	-0.197 N	-0.244 N	-0.333 N	-0.380 N	-0.384 N
F	-8.012 N	-4.035 N	0.835 N	6.169 N	16.117 N	21.419 N	21.846 N

7. Discussion

7.1 Interpretation of the eigenfrequency model results

Table 6. lists the first 6 values simulated for the eigenfrequencies of the 2D model, closest to 1 Hz. A complete list of all 60 simulated eigenfrequencies obtained from the 2D model is shown in the appendix, section 9.5 in table 19. All obtained values correspond to eigenfrequencies of the system as the free-body motions do not appear for the 2D model. All eigenfrequencies are strictly positive real numbers. The lowest eigenfrequency value is found at 204.56 Hz., and only the first seven values are below 10kHz. The other 53 obtained eigenfrequencies range from 10kHz to 140kHz.

Figure 16. shows the mode shapes corresponding to the first and sixth simulated eigenfrequencies of the 2D model. The legend depicts the displacement magnitude of the material in millimetres. The mode shapes corresponding to the second to fifth eigenfrequencies obtained from the model are shown in the appendix, section 9.9 in figure 34. These mode shapes all have different characteristics, as there are no mirroring mode shapes between these six mode shapes. The displacement for the first three eigenfrequencies is only present in the lower half of the impeller. The mode shapes belonging to the fourth and fifth eigenfrequencies also show a displacement of the tip of the impeller. The sixth eigenfrequency has a mode shape completely different from the others shown in figure 16., as the direction of displacement of the impeller is in the other direction.

Table 7. lists value seven to twelve simulated for the eigenfrequencies of the 3D model, closest to 1 Hz. A complete list of all 60 simulated eigenfrequencies for the 3D model is shown in the appendix, section 9.6 in table 20. The first set of six eigenfrequencies are imaginary, close to zero values that are expected when performing a numerical eigenfrequency simulation of a 3D model, as they correspond to the free-body motions of the free system components. These values are therefore neglected. The seventh to twelfth simulated values, the second set of six eigenfrequencies, are all found to be strictly real and positive. These are the lowest eigenfrequencies computed for the numerical 3D model. The first set of eigenfrequencies occurs at a frequency range between 5kHz-~12kHz. This is a large range with a high limit. The lowest value obtained for an eigenfrequency is 5207.9 Hz.

Figure 17. shows the mode shapes corresponding to simulated eigenfrequencies seven and nine of the 3D model. The legend depicts the displacement magnitude of the material in millimetres. The mode shapes corresponding to the sixth, eighth, and tenth to twelfth eigenfrequencies obtained from the model are shown in the appendix, section 9.9 in figure 35. The first two mode shapes of the 3D model show displacement only at the tip of the impeller. Both mode shapes have comparable displacements in either x-direction for an eigenfrequency of 5207.9 Hz., or y-direction for an eigenfrequency of 5667.3 Hz. This same mirroring of the mode shapes in x- and y-direction is seen for the third and fourth mode shapes, where the displacement is present in the bottom half of the impeller. The mode shapes belonging to the obtained eigenfrequencies 5 and 6 show only displacement of the vane material.

The difference in simulated eigenfrequency values between the 2D and 3D model is completely opposite to literature in analytic determination of eigenfrequencies. When comparing both calculation methods, eigenfrequencies obtained using 2D methods are expected to turn out higher than eigenfrequencies obtained using 3D methods. However, in the case of the 2D and 3D numerical models, this opposite difference can be brought back to the fact that the 2D model does not include the total 3D structure and the corresponding mass of the impeller. Because of this, for numerical modelling the values obtained via a 2D method are expected to turn out lower than those obtained via 3D method. The values for the eigenfrequencies obtained from the 2D model are therefore ignored for the analytical discussion of the possibility of an eigenfrequency problem. The eigenfrequencies obtained from the 3D model are more representative of the eigenfrequencies of the actual impeller. Therefore these eigenfrequencies will be used in the analytical discussion of the possibility of an eigenfrequency problem.

7.2 Discussing the possibility of an eigenfrequency problem

The observed critical unstable behaviour occurs at a rotational speed of 6000 RPM, i.e. 100 Hz. The lowest value obtained for an eigenfrequency of the 3D model is 5207.9 Hz. 100 Hz. does not lie within the frequency ratio range of this eigenfrequency the literature expected: $0.5 < wa/w0 < 1.5$, as this ratio is 0.019. As all other eigenfrequencies obtained from the simulation are at higher frequencies, none of the eigenfrequencies can produce a frequency ratio lying in the specified range. Therefore, the vibrations caused by the high rotational speed of the impeller cannot be linked to the unstable behaviour of the pump.

Since the impeller has six blades, the blade-pass frequency is equal to six times the rotational speed of 100 Hz., thus 600 Hz. This is not within the frequency range the literature

expected: 0.5 < wa/w0 < 1.5 as this ratio is 0.115. Thus at this rotational speed the blade-pass frequency is not able to create vibrations that can cause an eigenfrequency problem and can therefore not be held responsible for the unstable behaviour of the pump.

To analytically assess if flow induced vibrations created by the liquid can create a frequency at 6000 RPM that fits within the expected frequency range, equation X. and X. are used. For the Reynolds number, using the results from the performance test, a range is found between ~24000. The Strouhal number found for the cylindrical tubes to the pump is 0.1978. This subsequently means that for the tubes the fluid induced vibrations at a rotational speed of 6000 rounds per minute occur with a vortex shedding frequency of approximately 50.54 Hz. This is also not within the frequency range the literature expected: 0.5 < wa/w0 < 1.5, as this ratio is 0.0097. Thus the vortex shedding frequency in the upstream tube cannot create an eigenfrequency problem in the pump.

It can therefore be stated that none of the assessed phenomena are able to cause an eigenfrequency problem in the impeller. This means that for RSQ1, the null hypothesis cannot be rejected.

7.2 Interpretation of the performance test results

During the experiment it was reported that the logging software for the suction pressure P1 and discharge pressure P2 parameters was not working correctly. Therefore the measurements of these parameters were recorded analogue. This did add an additional human error factor to the experiments, as the accuracy of the recorded measurements for P1 and P2 was lowered by the capabilities of the human, in comparison to the digitally logging of the parameters by the computer script. The results were still studied and used in other parts of the project.

The scatter plot displayed in figure 18. shows the pressure difference output results for all resistors and every rotational speed for every sample group. First of all, during the experiment it was observed that for samples from the reference group at rotational speeds over 6000 RPM the impeller could become desynchronised from the electromotor. When this phenomenon occurred, no output parameters could be measured, as the flow would drop dead. Therefore, for 6000 RPM and 6500 RPM, the reference group does not contain five usable parameter results, influencing the mean results. This phenomenon did not occur for the clamped group and experimental group.

What stands out in the graph is the contrast between the behaviour of the pressure difference at lower- and higher rotational speeds. For lower rotational speeds, it is suggested the pressure difference follows an observable linear trend for all groups. This is in accordance with the literature as an increase in the rotational speed results in a larger displacement of the flow. However, for higher rotational speeds all groups deviate from this linear behaviour. For the reference group and the clamped group this occurs from 5500 RPM. For the experimental group this deviation occurs from 5000 RPM. This deviation occurs simultaneously with the introduction of the unstable behaviour. It is therefore suggested that these parameters are correlated.

In order to evaluate the difference between all three sample groups for both the pressure difference and flow rate output parameters, the output values for a rotational speed in the stable regime, at 4000 RPM, were compared. Two separate two-sample T-tests were performed,

included in the appendix in section 9.12., figure 45. and figure 46.: one T-test compared the pressure difference parameter and one T-test compared the flow rate parameter. No significant difference for both parameters was observed between the clamped group and the reference group at 4000 RPM. Therefore, it can be stated that the difference in assembly has not statistically changed the output of the pump for a rotational speed of 4000 RPM. Thus, it can be stated that the clamping of the samples in the clamping group has not made the clamped group different from the reference group, making the clamping a good method to be used for the experiments. Furthermore, no significant difference for both parameters was observed between the clamped group and the experimental group at 4000 RPM. Therefore, it can be stated that the closing of the holes has not changed the pump performance in terms of pressure difference and flow rate at 4000 RPM. The results of the T-tests are included in the appendix, section 9.12. figure 47. and figure 48.

The scatter plot in figure 19. shows the pressure difference output for all results with a stable observation (1) for all resistors for all sample groups. The regression lines in this plot suggest a linear behaviour for the pressure difference for all three sample groups for the lower rotational speeds. For the reference group and the clamped group these lines show no difference, reinforcing the statement that these sample groups are equal in the stable regime in terms of performance parameter outputs. However, for the experimental group a slightly lowered slope is observed for the linear regression with respect to the other sample groups. This indicates a difference in the linear behaviour of the pressure difference between the experimental group and the other sample groups.

From the performance test results it can be stated that the clamped group has an equal behaviour as the reference group. Through the T-test it was shown that no significant difference is observed between the two groups. The linear regression line constructed of all stable results for the separate groups in figure 19. showed equal regression lines for both groups, reinforcing this statement. However, the T-test was only performed for two output parameters results at 4000 RPM. Furthermore, the linear regression line is constructed from four rotational speed points for the reference group and clamped group, while only from three rotational speed points for the experimental group. The arguments for the regression line are therefore not strong. Additional rotational speed measurement points have to be created in order for the behaviour to be properly defined.

The scatter plot in figure 20. shows the relation between the flow rate and the rotational speed of the impeller for the combined reference and clamped groups for each resistor used in the experimental setup. It is observed that the resistance influences the flow rate passing through the system: a higher resistance from a small diameter resistor decreases the flow rate. Furthermore, a decrease in slope of the linear regression lines can be observed for the resistors with a small diameter (high resistance). This suggests the resistance is inversely proportional to the flow rate, and inversely proportional to the derivative of the flow rate. This is in accordance with the literature, as in the electrical domain it is found that resistance R is inversely proportional to electrical current I and inversely proportional to the amount of net charge ΔQ passing through a given cross-sectional area.

7.3 Discussing the Q-H curves

Figure 21. shows the Q-H curves for every resistor at varying rotational speeds. This relation very distinctly shows the influence of a higher resistance on the performance of the pump. First of all, it is observed that the Q-H curve shifts to the left for higher resistances. This is interpreted as: the higher resistance from a small diameter resistor decreases the flow rate. Furthermore the slope of the Q-H curve increases with increasing resistance. This suggests the resistance is inversely proportional to the flow rate, and to the derivative of the flow rate. This is in accordance with the literature, as explained at the end of discussion section 7.2.

On the other hand, figure 22. displays the Q-H curves for the centrifugal pump with constant rotational speed for varying resistance. This figure further shows an almost constant pressure difference behaviour between the various resistances. For every rotational speed from 3500 RPM to 5000 RPM all pressure difference measurements for the different resistors are within a less than 20 mmHg range. A small decrease in pressure difference can be observed for every resistor, forming a trend with a small, negative slope. From the measurement points it can therefore be stated that the pressure difference is only weakly influenced by the resistance as it retains an almost constant value, observed at every rotational speed. This coincides with the literature as the inversely proportional relation between the resistance and the flow rate, results in a constant value for the pressure difference.

Furthermore, from both figures 21. and 22. it can be observed that the rotational speed has a large influence on both the pressure difference and the flow rate: the Q-H curve is shifted upwards, translating to an increased pressure difference, and is both shifted to the right and elongated, translating to an increase in flow rate and increase of the growth factor of the flow rate, for each increase in rotational speed. This is in accordance with the literature: an increase in velocity relates directly to an increase in flow rate. For a constant resistance, an increase in flow rate relates directly to an increase in the pressure difference over the pump, as $R = U/I$

7.4 Interpretation of the stability experiment results

Figure 23. displays the mean stability regimes of the combination of the clamped group and reference group for all resistors in a 100% stacked area chart. The legend includes the different stability regimes. An overview of the mean stability observations per resistance per rotational speed is shown in the appendix section 9.8, table 26. No significant differences in stability observations were found between the different resistors. Therefore all observations per rotational speed were combined to determine the mean stability regime distribution for each rotational speed. This holds for all sample groups. It was observed that 100% of the pump samples remain stable for rotational speeds up to 4500 RPM. At 5000 RPM tip displacement is clearly seen in more than 30% of the sample measurements. However, still more than 55% of the test samples show stable behaviour. From 5500 RPM the stable behaviour is no longer observed, with major instability being observed the dominant behaviour in the pump. From this rotational speed, critical instability is also first observed and at 6000 RPM and 6500 RPM this is the main behaviour observed.

For samples from the reference group, desynchronisation of the impeller from the electromotor was observed for rotational speeds of 6000 RPM and 6500 RPM at multiple

samples. This phenomenon was not observed at the clamped group. This difference can be explained by the introduction of an additional clamping force for the clamped group. In the reference group, only the magnetic force between the impeller and the electromotor was responsible for keeping the complete pump to the electromotor. When the critical instability phenomenon was observed, it could be seen that the pump was able to move slightly due to the loss of magnetic force caused by the increase in distance between the magnets in the impeller and the magnets in the electromotor, because of the oscillations of the impeller. This increase in distance caused the impeller to desynchronise, not being able to follow the electromotor anymore. With the addition of the constant clamping force, the pump was not able to move, prohibiting the possibility of desynchronization.

In figure 24., a 100% stacked area chart with the mean stability observations of the clamped group is shown to compare to the stability observations from the experimental group. The same legend used for figure 23. was used for this figure. An overview of the mean stability observations per resistance per rotational speed is shown in the appendix, section 9.10, table 32. Other than the exclusion of the desynchronisation regime, the stability regimes in figure 24. are comparable to figure 23. This indicates that the reference group and the clamped group do not show significant differences in terms of stability observations.

The stability regimes of the clamped group in figure 24. and the stability regimes of the experimental group in figure 25. were compared. An overview of the mean stability observations per resistance per rotational speed is shown in the appendix, section 9.10, table 33.

What is immediately striking about figure 25. compared to figure 24. is the shift of all stability regimes towards lower rotational speeds. Only for 3500 RPM a 100% stable regime is observed. The minor instability regime is now the majority observation at 4500 RPM compared to 5000 RPM in figure 24. Similarly, the major instability regime is the most prominently present regime at 5000 RPM compared to 5500 RPM in the clamped group. For the experimental group, critical instability is already observed at 5000 RPM and is present for 100% of the sample observations from 5500 RPM. It is observed that the sizes of the minor instability regime and the major instability in figure 25. are comparable to their sizes in figure 24., with both regimes being the majority of the observations for one rotational speed and a minority of the observations in two bordering rotational speeds.

From the results of the stability experiment for the clamped group and the experimental group and the comparison of the stability regime figures, it can be stated that the stability regimes are equally shaped for both groups. The location of the stability regimes for the experimental group is shifted to lower rotational speeds in comparison to the clamped group. This indicates that the design change, removing the holes from the impeller, has changed the stability of the pump and has made the pump more susceptible to unstable behaviour as the observable instability regimes have shifted towards lower rotational speeds. Vice versa can be stated that the holes in the impeller design of the pump have enabled the pump to remain a stable behaviour at a larger range of rotational speeds.

7.5 Interpretation of the CFD model results

7.5.1 Figures on the internal flow behaviour of the conventional impeller

Figures 26., 27. and 28. show the simulated internal flow behaviour of the fluid inside the pump in terms of fluid velocity, pressure distribution and velocity streamlines, respectively. Additional figures of the simulated internal flow behaviour are included in the appendix, section 9.11, figures 36-38.

In the left pane of figure 26. it can be observed that globally the highest velocities simulated appear around the impeller vanes. Locally at the vanes, the highest velocity is present lateral at the front side of the vanes. This is according to expectation, as the disruption of the fluid created by the geometry of the passing vanes during operation creates displacement of the fluid, resulting in an increase in the fluid velocity. On a local level, the lateral part of the vanes has a larger velocity with respect to the central part, resulting in a slight difference in fluid velocity over the front of the vanes.

A large portion of this velocity is transported from the impeller into the spiral towards the outlet of the pump. This is observed by the relatively higher velocity present in this part of the model compared to other parts next to the impeller. The velocity at the end of the spiral is shown to not be normally distributed over the area of the outlet pipe. Higher velocities at the lateral side of the spiral combined with an immediate change to lower velocities at the lateral side of the outlet pipe suggest turbulent flow caused by an elbow pipe structure. This means the curvature of the spiral is too intense for a fluid of this speed to stay a laminar flow. From the right pane it is also observed by the light blue colour that a minor part of the fluid velocity has moved underneath the impeller and to the inner part of the impeller. This can be interpreted as a low velocity flow being present underneath and inside the impeller.

Figure 27. shows the pressure distribution in the fluid in the pump. The low pressure present at the inlet and the high pressure at the outlet correspond to the input values for the suction- and discharge pressure. The lowest pressure simulated in the model is present behind the tip of the impeller vanes. The displacement of the fluid because of the passing of the vanes, creates a local suction pressure at the back of the vanes. The absolute height of the peaks is partially due to the set strict incompressibility of the flow in the model properties. In reality, fluids are never completely incompressible, resulting in lower local suction pressure peaks behind the vanes. The highest simulated in the model is present in front of the lateral side of the vane, specifically the vane in front of the outlet pipe. This is also on par with the expected results.

The pressure of the fluid from the inlet towards the impeller shows to increase gradually as it is approaching the vanes. The pressure increases around the impeller vanes and remains high in the spiral. The pressure distribution in the spiral shows the fluid at the outer diameter of the spiral has a higher pressure than the fluid at the inner diameter. Furthermore, the pressure is shown to build up from the beginning of the spiral towards the end of the spiral. Underneath and at the inner part of the impeller a pressure close to zero mmHg is maintained.

Figure 28. shows the velocity streamlines of the flow inside the pump. The results in this figure are in accordance with figure 26., as it is observed that most velocity is gained by the rotation of the impeller vanes. Most of the streamlines travel from the impeller into the spiral towards the outlet. At the outlet pipe, the turbulent flow behaviour caused by the curvature of the

spiral is observed. A low velocity flow from underneath the impeller through the holes in the impeller shaft can also be observed.

7.5.2 Output and performance tables of the conventional impeller

Table 8. shows the output parameters of the CFD model. The pressure at the inlet and the outlet has remained equal to the input value used to simulate the internal flow behaviour at 4000 RPM. However, the simulated values for the flow rate at the inlet and outlet are not as expected from the experimental results. The simulated flow rate at the inlet and the outlet is 0.44 of the flow rate measured in the experiments. It was investigated if this low flow rate was a product of an unwell-defined mesh. Therefore, the maximum mesh size was halved. This did not result in a simulated flow rate closer to the experimental flow rate, as shown in table 8. An additional mesh refinement also did not bring the simulated flow rate closer to the flow rate measured in the experiments. This suggests that the numerical model is lacking the correct boundary conditions to simulate the output parameters from the experiments. For larger refinements, the model stopped converging properly. This suggests there is a mesh problem for the model. Additionally it is suggested that the input parameters for the pressure at the inlet and outlet obtained from the experiments using the experimental model are not correct for the inlet and outlet of the pump. The pressure sensors P1 and P2 were connected at least two and six nominal diameters off the pump samples. It was assumed that the measured suction- and discharge pressure was equal to the pressure at the inlet and outlet of the pump, respectively. However, there is a chance that the basic resistance of the tube between the pump and the pressure sensors has additionally increased the measured pressure difference over the pump. Furthermore, the difference in tube diameter between the PVC tubing and the silicone tubing used to apply the flow sensor over could have been able to increase the flow rate due to the decrease in diameter of the silicone tube with respect to the diameter of the PVC tubing. These influences have to be taken into account for future research regarding the pump. Now the rest of the results will be discussed:

Table 9. shows the simulated performance parameters of the CFD model. Because the simulated values for the flow rate are inconsistent with the experimental values, it is assumed the values of all parameters dependent on the flow rate are incorrect. This includes the flow rate and mass flow. From the table it is observed that from the power shaft consumption only 24.2% is transferred to the fluid, giving the pump model an efficiency of 0.242. Furthermore the pump model has minimal torque.

A representable Q-H curve of the simulated pressure head and flow rate could not be made because of the incorrect flow rate simulated.

7.5.3 Output and performance results from the auxiliary sweep for the conventional impeller design

Table 10. shows the output parameters of the pump model for a range of rotational speeds from 3500 to 6000 RPM with a step size of 500 RPM. The pressure at the inlet and the outlet has remained equal to the input value used to simulate the internal flow behaviour at all rotational speeds. The simulated values for the flow rate at the inlet and outlet are not as expected from the experimental results. From 3500 to 5000 RPM for every increase in rotational

speed, an increase in the average flow rate is observed. However at 6000 RPM the value for the simulated flow rate has dropped from the flow rate simulated for 5500 RPM. Furthermore, at 6500 RPM, a large negative flow rate is simulated at both the inlet and outlet. An explanation for this can be the extremely coarse mesh used for the simulation. However it was seen that a refinement of the mesh at 4000 RPM did not increase the accuracy of the simulated flow rate. A global convergence problem of the CFD model is suspected to be responsible for the incorrect simulation of the parameters.

Table 11. shows the simulated performance parameters of the auxiliary sweep. Because the simulated values for the flow rate are inconsistent with the experimental values, it is assumed the values of all parameters dependent on the flow rate are incorrect. This includes the flow rate and mass flow. Furthermore, the simulations for 5500 and 6000 RPM were excluded in the assessment of the performance parameters because of the inconsistency of the flow rate values for these simulations. The highest efficiency is observed at 3500 RPM. Between higher rotational speeds the efficiency of the pump model is shown to be fluctuating, not showing a distinct increase or decrease in efficiency with the increase of the rotational speed.

7.5.4 Comparing the internal flow behaviour of the closed impeller to the conventional impeller design

Figure 29., 30., and 31. show the simulated internal behaviour of the fluid inside the closed impeller pump in terms of fluid velocity, pressure distribution and velocity streamlines.

Comparing the fluid velocity results in figure 29. to figure 26., it is observed that the only difference between the two situations is the fluid velocity simulated underneath the impeller. For the closed impeller this velocity is relatively lower than for the conventional impeller design. This suggests that the fluid underneath the impeller has more characteristics of a standing fluid for the closed impeller design than for the open impeller design.

Comparing the pressure distribution results in figure 30. to figure 27., it is observed that the pressure underneath the closed impeller design is relatively higher to the rest of the pump compared to the open impeller design. This suggests the fluid underneath the impeller relatively builds up more pressure for the closed hole design than for the open hole design.

Comparing the velocity streamline results in figure 31. to figure 28., it is observed that the flow velocity underneath the impeller is relatively lower for the closed impeller design compared to the open impeller design. This reinforces the suggestion that the fluid underneath the impeller has more characteristics of a standing fluid for the closed impeller design than for the open impeller design.

The comparison of the figures on the simulated internal flow behaviour of the closed impeller design and the conventional impeller design shows that, by closing the holes in the impeller, the relative velocity underneath the impeller is decreased, while the relative pressure of the flow is increased. This indicates that the effect of the design change, removing the holes from the shaft of the impeller, is most present underneath the impeller.

7.5.5 Comparing the output and performance parameters of the closed impeller to the conventional impeller design

Table 12. and 13. display the output parameters and performance parameters of the closed impeller design model, respectively.

Table 12. shows the output parameters of the CFD model. The pressure at the inlet and the outlet has remained equal to the input value used to simulate the internal flow behaviour at 4000 RPM. However, the simulated values for the flow rate at the inlet and outlet are not as expected from the experimental results. The simulated flow rate at the inlet and the outlet is 0.52 of the flow rate measured in the experiments. It is assumed that this deviation from the experimental results has the same origin as the deviation of the flow rate of the conventional impeller design to the experimental results. Comparing the simulated flow rates shows a higher flow rate for the closed impeller model than for the conventional impeller model.

Table 13. shows the simulated performance parameters of the CFD model of the closed impeller design. Because the simulated values for the flow rate are inconsistent with the experimental values, it is assumed the values of all parameters dependent on the flow rate are incorrect. This includes the flow rate and mass flow. From the table it is observed that from the power shaft consumption 28.8% is transferred to the fluid, giving the pump model an efficiency of 0.288. Furthermore the pump model has minimal torque. A Q-H curve of the simulated pressure head and flow rate could not be made because of the incorrect flow rate simulated.

Compared to the performance parameters of the conventional impeller design in table 9., the closed impeller design has an increase in efficiency of 4.6%. The torque and pressure head are similar for both designs.

The comparison of the output and performance parameter results between the CFD model of the closed impeller pump design and the CFD model of the conventional impeller design show that the design change, closing the holes of the impeller, has increased the flow rate at the inlet and outlet, as well as the efficiency of the pump, while the pressure difference over the pump, the head and torque of the pump have remained constant.

7.5.6 Comparing the auxiliary sweep results of the closed impeller to the conventional impeller design

Table 14. shows the output parameters of the pump model for a range of rotational speeds from 3500 to 6000 RPM with a step size of 500 RPM. The pressure at the inlet and the outlet has remained equal to the input value used to simulate the internal flow behaviour at all rotational speeds. The simulated values for the flow rate at the inlet and outlet are not as expected from the experimental results. From 3500 to 5000 RPM for every increase in rotational speed, an increase in the average flow rate is observed. However at 5500 RPM the value for the simulated flow rate has dropped from a flow rate of 4.177 L/min simulated for 5000 RPM to below 1 L/min. Furthermore, at 6000 RPM, the simulated flow rate remains lower than the flow rates simulated for 3500, 4000, 4500 and 5000 RPM at both the inlet and outlet. From the internal flow behaviour, it was observed that the relative velocity of the fluid above the impeller was higher for 5500 RPM than for the lower rotational speeds. The pressure underneath the impeller was observed to be relatively higher for 5500 RPM than for the lower rotational speeds.

Furthermore the velocity streamlines seemed to indicate a partial flow upwards. If this simulated behaviour is correct, the theory behind these results is currently not well understood. The corresponding figures are included in the appendix, section 9.11., figure 42.-44.

Compared to the output parameter results auxiliary sweep of the conventional impeller design in table 10., for rotational speeds up to 5000 RPM, the flow rates for the closed impeller design are higher for every rotational speed.

Table 15. shows the simulated performance parameters of the auxiliary sweep. Because the simulated values for the flow rate are inconsistent with the experimental values, it is assumed the values of all parameters dependent on the flow rate are incorrect. This includes the flow rate and mass flow. Furthermore, the simulations for 5500 and 6000 RPM were excluded in the assessment of the performance parameters because of the inconsistency of the flow rate values for these simulations. The highest efficiency is observed at 5000 RPM. The efficiency of the simulated pump is increasing with the increasing of the rotational speed.

Compared to the performance parameters of the conventional impeller design to table 11. the efficiency of the closed impeller design has increased for the simulation of the closed impeller design. The pressure head and torque have remained equal in between designs.

From the comparison between the results of the auxiliary sweep of the experimental impeller design and the results of the auxiliary sweep of the conventional impeller design, it can be stated that the design change, closing the holes of the impeller, has globally increased the flow rate and the efficiency of the pump. However, it was also observed that for lower rotational speed the model puts out unstable data. Unfortunately, the accuracy of both CFD models is low, as seen by the simulated flow rate at the inlet and outlet. Therefore the credibility of the CFD model is not high. The interpretation of the results can therefore only be used as a suggestion, as it is unable to deliver hard evidence. It is therefore also decided to not use the results from the CFD model as input for the analytical assessment of the balance of forces.

7.6 Discussion on the balance of forces

Due to the inconsistent simulating of the parameters in the CFD model, the experimental results were used to analytically assess the balance of forces. These results were not representable for the true answer, as the input parameters for pressures around the impeller cannot be chosen correctly using the experimental results. However, they do allow for a behaviour of the residual force to be identified.

The balance of forces was only assessed in axial direction, because the vibrations of the impeller were determined to occur in the axial direction. The radial forces were therefore excluded from the assessment. This means the balance of forces in the pump was determined at the different rotational speeds by solving for $F = F(1) + F(mag) + F(J) + F(Wd)$. Forces oriented upwards axially were considered positive. For the magnetic force, the formula for two cylindrical magnets with equal radii R, and lengths L1 and L2 with a distance limit of $x>>R$ was used.[49]

Table 16. shows the values for all forces at all measured rotational speeds for the mean output parameters of the conventional impeller design. For the shroud area on the discharge side the area of the bottom of the impeller, excluding the inner diameter was considered as the holes in the impeller shaft allowed for flow in this area. For the experimental impeller design the

shroud area on the discharge side the complete area under the impeller was considered as no flow in this area was shown present inside the shaft of the impeller for this design.

It is observed that the residual force in the system follows a positive trend for the increase of the rotational speed, approaching zero from below. A flip to a positive value and therefore an upwards pointing residual force is observed from 5000 RPM and on. However, since the suction- and discharge pressures are utilised to determine both components of the axial impeller force *F(1)* instead of the local pressure present on top and underneath the impeller, the values for *F(s)* and *F(d)* were higher than in reality. The values are therefore not considered and only the behaviour of the residual force is considered. The flip of the residual force from a negative value to a positive value indicates the residual force has turned from pointing to the base of the pump to pointing from the base. This means that the impeller is actively pushed away from the axis towards the boundaries of the pump.

Table 17. shows the calculations for the experimental design of the impeller of the pump. It is observed that the residual force in the system follows a positive trend for the increase of the rotational speed. This is similar to the behaviour of the conventional impeller design. However, for the experimental impeller design it is observed that the residual force already turns to the upwards direction at a lower rotational speed compared to the conventional impeller design. This is a direct result of the assumption that the shroud area for the discharge side is increased by the closing of the holes, since no flow is observed within the inner diameter of the impeller. From the comparison in balance of forces between the conventional impeller design and the experimental design it can therefore be concluded that the axial forces for the experimental design become positive at a lower rotational speed than the axial forces for the conventional design. This is in accordance with the results of the stability experiment.

8. Conclusion & Recommendations

In this project a triptych of research methods has been used to study the (non)linear behaviour of the XVIVO cirQlife centrifugal pump to answer the research question and investigate the root cause of the instability of the pump at rotational speeds at higher rotational speed. Based on the interpretation of the results, and conclusions made from this study, recommendations for improvement of parts of the current study and next steps towards future research are given.

8.1 Conclusion on eigenfrequency

Through the use of a numerical model it was studied if the free components of the centrifugal pump were suffering from an eigenfrequency problem at a high rotational speed caused by the rotational frequency of the impeller, by the blade-pass frequency of the vanes, or by FIVs caused in the tube in front of the pump. After analytical assessment, an eigenfrequency problem caused by these phenomena was shown to be impossible, as all the ratios for the frequencies created by the phenomena to the lowest eigenfrequency value simulated by the 3D model remained outside the expected range 0.5<wa/w0>1.5. The values simulated for the eigenfrequencies are too high to be dangerously excited by the studied phenomena. An

eigenfrequency problem can therefore not be caused by these phenomena. Therefore the null hypothesis for RSQ1 is retained and the alternative hypothesis that the vibrations are created by an eigenfrequency problem is discarded.

8.2 Recommendations for the eigenfrequency analysis

Recommendations for the analysis of an eigenfrequency problem of the pump include an experimental modal analysis to verify the numerical model. In the current experiment this is not performed, which creates the speculation of the numerical model possibly not being accurate. This field is not given a high priority however, since the results of this study show a very large gap between the analytically obtained frequencies of the vibrations caused by the rotational speed for the impeller, the blade-pass frequency of the vanes, or the frequency of the fluid induced vortices and the values for the eigenfrequencies simulated by the model.

8.3 Conclusion on the pump performance & stability

Through the use of an experimental model the performance parameters of the pump at higher rotational speeds were studied in order to get a better understanding of the output parameters of the pump in terms of pressure, flow rate and stability. Five resistors were designed and manufactured to simulate the different resistances to blood flow by a liver or a kidney during HMP or NMP in order to create Q-H plots for different operational settings. 10 pump samples were used, divided into a reference group of five glued samples and an unconventional group of five unassembled samples clamped watertight to the electromotor with a clamp.

For the stable results it was found that there was no significant difference in terms of output parameters between the reference group and the clamped group. Both sample groups followed a linear behaviour for pressure difference and flow rate. For the unstable results at higher rotational speeds this linear behaviour theory did not apply.

Using the Q-H curves, it was observed that resistance mostly influenced the flow rate through the pump, while the pressure difference over the pump was kept almost constant for different resistances at the same rotational speed. An inversely proportional relation between the resistance and the flow rate, and the derivative of the flow rate was identified. The rotational speed was shown to both influence the pressure difference and flow rate parameters. The results showed a proportional relation between the rotational speed and the pressure difference, and the flow rate.

Stable measurements of the pressure difference and flow rate at higher rotational speeds proved to be impossible as the pumps would show major instability from 5500 RPM, causing the parameters to fluctuate heavily. Critical instability was observed at rotational speeds from 6000 RPM. This prohibited the inclusion of the higher rotational speeds in the Q-H curves. Therefore, RSQ2 could not be fully answered properly for the output parameters pressure difference and flow rate.

It was however possible to map the stability regimes of the pump for all resistances and all rotational speeds. It was observed that the resistance used in the circuit did not significantly change the stability observations for the pump per rotational speed. Therefore one graph could

be created for the combination of the reference group and the clamped group. The reference group showed a distinctly different behaviour from the clamped group at 6000 RPM and 6500 RPM by displaying desynchronisation from the electromotor. This was attributed to the loss of magnetic force due to an increase between the aligned magnets caused by the unstable behaviour of the impeller. For the clamped group this was determined to not be possible. For the other rotational speeds, these groups showed no difference in stability observations. The performance test showed the desynchronisation of the samples within this group disrupted the flow, making it impossible to capture the output parameters. It was therefore concluded that the reference group was not suitable for an experiment involving rotational speeds above 6000 RPM and that modifications to the locking mechanism should be made in future experiments at this rotational speed.

The influence of the holes in the design of the impeller was studied by closing the holes inside the shaft and performing the performance test and the stability experiment. Two T-tests showed no significant difference in measured performance parameters between the experimental group and the clamped group at 4000 RPM. Comparing the linear regression lines drawn between the measurements observed to be stable however suggested a different linear behaviour of the pressure difference for the closed impeller design compared to the conventional design. No definitive answer can therefore be given to RSQ3 in terms of output parameters pressure difference and flow rate.

In the stability experiment, it was observed that all stability regimes of the pump shifted to lower rotational speeds in comparison to the conventional design: minor-, major- and critical instability of the experimental group were all already observed at lower rotational speeds. It can therefore be concluded that the removal of the holes in the impeller had made the pump more prone to unstable behaviour. Alternatively it can be said that the inclusion of the holes in the impeller create a larger range of operational settings for which the pump can retain a stable behaviour. This allows RSQ3 to be answered in terms of stability observations, answering this Research Sub-Question partially.

8.4 Recommendations for the performance test and stability experiment

Recommendations for the performance test include the improvement of the quality of measuring. The logging method available for the logging of the suction- and discharge pressure values was not reliable as it was found afterwards not every measurement was correctly logged. Furthermore, this method did not allow for logging of all measurable parameters. The flow rate had to be read out of the display of an Organ Assist module at all times. Being able to log all measurable parameters reliably using one logging device, lowers the work pressure during the experiments, removing human errors as much, and making room for more careful assessment of the experiment as it is being performed.

Furthermore it is recommended to change the method experiments are done on the XVIVO cirQlife centrifugal pump by modifying the locking mechanism of the pump by applying a clamping mechanism to the pump from the top, clamping the pump down to the electromotor. In the experiment it was shown that the current design of the pump is able to become desynchronised from the electromotor when the impeller lifts off the axis, increasing the distance

between the magnets and therefore the magnetic force in the process. By adding a clamping mechanism, there is not only a magnetic force for pulling the pump to the electromotor, as a constant clamping force is excluding any possibility of pump displacement. During the experiment it was concluded that there was no significant difference between the reference group and the clamped group. Therefore the clamping mechanism does not influence the output parameters of the pump.

The comparison between the two designs of the impeller (open impeller and closed impeller) showed in the stability experiment that the holes present in the standard design of the impeller causes the impeller to remain stable for higher rotational speeds. Therefore it can be said that the philosophy behind the design of the impeller is beneficial towards the stability of the pump. It is recommended to further study the influence of the holes present in the impeller in terms of size, shape, number, and location on the impeller.

To increase the strength of a regression analysis, it is recommended that the amount of different rotational speeds measured should be increased. This can be done either by decreasing the step size within the same range (have steps of 250 RPM or 200 RPM instead of 500 RPM) or by increasing the range (measuring from 500 RPM to 5000 RPM instead of 3500 RPM to 5000 RPM). In this current study the number of measurements for the stable regime is low, weakening the strength of the regression analysis significantly.

For future studies, it is recommended to investigate the difference in parameters between water used in the current experiment and blood, or blood-like medium. Water was assumed as the fluid for this first study regarding the XVIVO cirQlife centrifugal pump. However, the material properties of water differ significantly from the material properties of blood, or blood-like medium. It is of interest to investigate the effect of a different perfusion fluid on the behaviour of the pump.

A further recommendation is that the setup of the experimental model is critically assessed in order to validate if the pressure and flow measurements are correctly obtained and labelled. In this project, the flow was measured using a flow sensor that could only be applied to a tube of a smaller diameter than the rest of the circuit. It is recommended that the experiment is repeated using a flow sensor that can be applied over a same-size tube to prevent flow rate modification from happening because of the narrowing of the tube. Furthermore.

The last recommendation on the experimental model regards the difference between output parameters from the real world application of the pump and the performance parameters of the pump in the experimental model. The influence of all of the components present in the XVIVO application should be further investigated to obtain a good overview of all parameters of the circuit in the device.

8.5 Conclusion on the CFD analysis of the internal flow behaviour

Through the use of a numerical model the internal flow behaviour of the pump was studied. It was observed that the CFD model was not able to simulate the flow rate corresponding to the input pressures at the inlet and outlet of the pump model. Other flow rate dependent parameters could therefore also not be simulated accurately. Several options were suggested to have created this error: a not well-defined mesh, not well-defined boundary

conditions, or experimental results unrepresentable of the parameters present at the inlet and outlet of the pump due to choices made for the experimental model.

From the comparison between the closed impeller design and the conventional impeller design it was concluded that the holes in the impeller were responsible for a decrease in pressure and increase in flow velocity underneath the impeller. The pressure head and torque remained equal for both models.

8.6 Recommendations on the CFD model and numerical characterisation of the internal flow behaviour

Recommendations for future research regarding the use of the CFD model for the numerical characterisation of the internal flow behaviour of the pump model include the reassessment of all interactions between the fluid and parts of the pump. In this project Fluid-Structure Interactions were not included, as it was assumed these were not significant to the flow behaviour.

A second recommendation for a more extensive research includes further refinement of the mesh of the model. Using an extremely coarse mesh simplified many of the circular aspects of the pump to polygons, such as the inlet, outlet and spiral. For this first approximation this was deemed sufficient, but for further investigation regarding the internal flow behaviour of this centrifugal pump, going further into local flow behaviour of a specific component of the pump, this refinement of the mesh would be of great assistance to make changes in behaviour in these smaller regions more defined.

The simulation of the conceptual model for the impeller without holes showed that using the CFD model it has been able to compare the performance parameters between different impeller designs. It is recommended that for a future potential redesign of the impeller of the XVIVO cirQlife pump, more extensive CFD analysis is used to study the output parameters of the concept in combination with the internal flow behaviour of the pump, before prototypes are manufactured and tested on, as CFD analysis will be able to decrease the number of time-consuming and costly tests performed on different geometry prototypes. However, in order to do this, first the accuracy of the existing model should be improved.

8.7 Conclusion on the balance of forces results

The balance of radial forces was analytically assessed using the experimentally obtained performance parameters. Due to the inaccuracy of the CFD model it was decided to exclude the results of the CFD model from the assessment of the balance of forces. The exact values obtained from the assessment of the balance of forces were not taken into account, as the input data used for the pressure distribution around the impeller was chosen incorrectly. However, a similar relation could be identified for the conventional impeller model and the experimental impeller model between the rotational speed of the impeller and the residual force. The balance of axial forces changed directions from a specific rotational speed, indicating that the impeller was being pushed away from the axis. It was concluded that through the assumption that the closed impeller design had a larger shroud area on the discharge side, this tipping point occurred at a lower rotational speed. However, RSQ4, could not be answered accurately since

CFD results were not used for the assessment of the balance of forces. The results are therefore only a rough approximation.

8.8 Recommendations on the assessment of the balance of forces

Recommendations for the assessment of the balance include using the correct data for the local pressure around the impeller for the calculation of the axial impeller force components. In this experiment this was not possible due to the inaccuracy of the CFD model. The exact values for the balance of forces for all rotational speeds were not obtained.

9. Appendix

9.1 Modelling instructions 2D eigenfrequency model

From the File menu, choose New.

NEW
In the New window, click Model Wizard.

MODEL WIZARD

1. In the Model Wizard window, click 2D.
2. In the Select Physics tree, select Structural Mechanics>Solid Mechanics (solid).
3. Click Add.
4. Click Study.
5. In the Select Study tree, select General Studies>Eigenfrequency.
6. Click Done.

GEOMETRY 1: complete 2D geometry

1. Rename component 1 (comp1) to Complete 2D Geometry.

GEOMETRY 2: Impeller core

1. Click Add Component, select 2D.
2. Rename component 2 (comp2) to Impeller Core.
3. Change Length unit to mm.
4. In the Geometry toolbar, select Circular Arc.
5. Under Properties, change to Endpoints and start angle.
6. For Starting Point, fill in r: 0, z: 20.29.
7. For Endpoint fill in: r: 1.29, z: 19.
8. For Angles fill in Starta angle: 90 deg, and check Clockwise.
9. In the Geometry toolbar, select Polygon.
10. For Object Type, change to Open curve.
11. Fill in:

r (mm)	z (mm)
2.13	19
1.29	19

12. In the Geometry toolbar, select Interpolation Curve.
13. For Object Type, change to Open curve.
14. Fill in:

r (mm)	z (mm)
2.13	19

2.13	16.4
2.11	15.9
2.41	10.2
2.76	8.6
4.2	4.64
4.64	1.71

15. In the Geometry toolbar, select Circular Arc.
16. Under Properties, change to Endpoints and radius.
17. For Starting Point, fill in r: 4.64, z: 1.71.
18. For Endpoint fill in: r: 6.62, z: 0.
19. For Radius fill in 2.
20. Under Angles check Short arc.
21. In the Geometry toolbar, select Polygon.
22. For Object Type, change to Open curve.
23. Fill in:

r (mm)	z (mm)
6.62	0
16.05	0
16.05	6.3
14.1	6.3

24. In the Geometry toolbar, select Circular Arc.
25. Under Properties, change to Endpoints and radius.
26. For Starting Point, fill in: r: 4.17738, z: 15.04
27. For Endpoint, fill in r: 14.09998, z: 10.
28. For Radius, fill in 10.
29. Under Angles, select Short arc.
30. In the Geometry toolbar, select Polygon.
31. Under Object Type, change to Open curve.
32. Fill in:

r (mm)	z (mm)
3.29	22
4.17737956614	15.04

33. In the Geometry toolbar, select Quadratic Bezier.
34. For Control points, fill in:

r (mm)	z (mm)
1: 0	32.68
2: 1.92833	32.68
3: 3.29	22

35. For Weights, fill in:

1: 1
2: 1/sqrt(2)
3: 1

36. In the Geometry toolbar, select Polygon.
37. Under Object Type, change to Open curve.
38. Fill in:

r (mm)	z (mm)
0	32.68
0	20.29

39. In the Geometry toolbar, select Transforms, select Copy.
40. Select the complete geometry outline.
41. In the Geometry toolbar, select Transforms, select Mirror.
42. Select copy1.
43. Form Union.

GEOMETRY 3: large vane

1. Click Add Component, select 2D.
2. Rename component 3 (comp3) to Large Vane.
3. Change Length unit to mm.
4. In the Geometry toolbar, select Polygon.
5. Under Object Type, change to Open curve.
6. Fill in:

r (mm)	z (mm)
15.41	4.4
15.55	7.46

7. In the Geometry toolbar, select Quadratic Bezier.
8. For Control Points, fill in:

r (mm)	z (mm)
1: 15.55	7.46

2: 15.55	10.98
3: 12.31	10.98

9. For Weights, fill in:

1: 1
2: 1/sqrt(2)
3: 1

10. In the Geometry toolbar, select Quadratic Bezier.
11. For Control Points, fill in:

r (mm)	z (mm)
1: 12.31	10.98
2: 10.6815	10.98
3: 9.56	12.58

12. For Weights, fill in:

1: 1
2: 1/sqrt(2)
3: 1

13. In the Geometry toolbar, select Polygon.
14. Under Object Type, change to Open curve.
15. Fill in:

r (mm)	z (mm)
9.56	12.58
8.06	14.72

16. In the Geometry toolbar, select Quadratic Bezier.
17. For Control Points, fill in:

r (mm)	z (mm)
1: 8.06	14.72
2: 7.66516	15.2833
3: 6.95	15.12

18. For Weights, fill in:

1: 1

2: 1/sqrt(2)
3: 1

19. In the Geometry toolbar, select Polygon.
20. Under Object Type, change to Open curve.
21. Fill in:

r (mm)	z (mm)
6.95	15.12
3.14	14.25
2.35	14.16
2.35	11
10	4.4
15.41	4.4

22. Form Union.

GEOMETRY 4: small vane

1. Click Add Component, select 2D.
2. Rename Component 4 (comp4) to Small Vane.
3. Change Length unit to mm.
4. In the Geometry toolbar, select Polygon.
5. Fill in:

r (mm)	z (mm)
-15.41	4.4
-15.63	7.13
-15.66	7.46
-15.41	4.4
-9.5	4.4
-7.07	6.5
-8.11	14.72
-8.11	8.11
-9.9	10.89

6. In the Geometry toolbar, select Quadratic Bezier.
7. For Control Points, fill in:

r (mm)	z (mm)
1: -15.66	7.46
2: -15.66	10.98
3: -12.39	10.98

8. For Weights, fill in:

1: 1
2: 1/sqrt(2)
3: 1

9. In the Geometry toolbar, select Quadratic Bezier.
10. For Control Points, fill in:

r (mm)	z (mm)
1: -12.39	10.98
2: -11.29	10.98
3: -11.23	11.28

11. For Weights, fill in:

1: 1
2: 1/sqrt(2)
3: 1

12. In the Geometry toolbar, select Quadratic Bezier.
13. For Control Points, fill in:

r (mm)	z (mm)
1: -11.23	10.98
2: -10.5	11.7
3: -9.9	10.89

14. For Weights, fill in:

1: 1
2: 1/sqrt(2)
3: 1

15. Form Union.

GEOMETRY 5: axis + axis base

1. Click Add Component, select 2D axisymmetric.
2. Rename Component 7 (comp7) to Axis + Axis Base.
3. Change Length unit to mm.
4. In the Geometry toolbar, select Rectangle.
5. Under Object Type, select Solid.
6. For Size and Shape, fill in: Width: 3, Height, 20.8.
7. For Position, for Base, select Corner, fill in: x: -1.5, y: -2.49.
8. In the Geometry toolbar, select Polygon.
9. Under Object Type, select Open curve.
10. Fill in:

r (mm)	z (mm)
7.3	-0.8
18.41	-0.8
18.75	1.12
18.95	1.12
19.15	0.92
19.22	-2.8
0	-2.8
0	-2.49
1.5	-2.49
1.5	7.24
1.93	6.57
2.41	5.37
2.62	4.6
2.85	3.04

11. In the Geometry toolbar, select Circular Arc.
12. Under Properties, change to Endpoints and radius.
13. For Starting Point, fill in: r: 2.85, z: 3.04.
14. For Endpoint, fill in: r: 7.3, z: -0.8.
15. Set Radius to 4.5. Select Short Arc.
16. In the Geometry toolbar, select Conversions, select Convert to Solid.
17. Select the complete base geometry outline.
18. In the Geometry toolbar, select Transforms, select Copy. Select csol1.

19. In the Geometry toolbar, select Transforms, select Mirror. Select copy2.
20. Form Union.

GEOMETRY 6: nylon ball

1. Click Add Component, select 2D.
2. Rename Component 7 (comp7) to Nylon Ball.
3. Change Length unit to mm.
4. In the Geometry toolbar, select Circle.
5. Under Object Type, select Solid.
6. For Size and Shape, fill in Radius: 1.19, Sector angle: 360.
7. For Position, under Base, select Center. Fill in x: 0, y: 19.
8. In the Geometry toolbar, select Circle.
9. Under Object Type, select Solid.
10. For Size and Shape, fill in Radius: 1.29, Sector angle: 180.
11. For Position, under Base, select Center. Fill in x: 0, y: 19.
12. In the Geometry toolbar, select Booleans and Partitions, select Difference.
13. For Objects to add, select c2. For objects to subtract, select c1. Check Keep objects to subtract.
14. Form Union.

GEOMETRY 7: magnets

15. Click Add Component, select 2D.
16. Rename Component 7 (comp7) to Magnets.
17. Change Length unit to mm.
18. In the Geometry toolbar, select Rectangle.
19. Under Object Type, select Solid.
20. For Size and Shape, fill in Width: 6, Height: 4.
21. For Position, under Base, select Corner. Fill in x: 7.5, y: 0.
22. In the Geometry toolbar, select Transforms, select Copy.
23. Select r2.
24. In the Geometry toolbar, select Transforms, select Mirror.
25. Select copy3.
26. Form Union.

GEOMETRY 1: complete 2D geometry

1. In the Geometry toolbar, select Import.
2. Under Source, select Geometry sequence. Select Impeller Core.
3. Import.
4. In the Geometry toolbar, select Import.
5. Under Source, select Geometry sequence. Select Large Vane.
6. Import.
7. In the Geometry toolbar, select Import.
8. Under Source, select Geometry sequence. Select Small Vane.
9. Import.

10. In the Geometry toolbar, select Import.
11. Under Source, select Geometry sequence. Select Axis + Axis Base.
12. Import.
13. In the Geometry toolbar, select Import.
14. Under Source, select Geometry sequence. Select Nylon Ball.
15. Import.
16. In the Geometry toolbar, select Import.
17. Under Source, select Geometry sequence. Select Magnets.
18. Import.
19. In the Geometry toolbar, select Booleans and Partitions, select Difference.
20. For Objects to add, select the Nylon Ball (imp5). For Objects to subtract, select the Axis + Axis Base (imp4). Check Keep objects to subtract.
21. In the Geometry toolbar, select Booleans and Partitions, select Difference.
22. For Objects to add, select the Magnets (imp6). For Objects to subtract, select the Impeller Core (imp1). Check Keep objects to subtract
23. In the Geometry toolbar, select Booleans and Partitions, select Union.
24. Select the geometries for the Impeller Core, Large Vane, Small Vane, Magnets and Nylon Ball.
25. In the Geometry toolbar, select Booleans and Partitions, select Union.
26. Select the geometries for the Axis + Axis Base.
27. Click Form Union. Under Action, change to Form an assembly.

9.2 Modelling instructions 3D eigenfrequency model

From the File menu, choose New.

NEW
In the New window, click Model Wizard.

MODEL WIZARD

1. In the Model Wizard window, click 3D.
2. In the Select Physics tree, select Structural Mechanics>Solid Mechanics (solid).
3. Click Add.
4. Click Study.
5. In the Select Study tree, select General Studies>Eigenfrequency.
6. Click Done.

GEOMETRY 1: complete geometry

1. Rename component 1 (comp1) to Complete 3D Impeller.

GEOMETRY 2: Impeller core

44. Click Add Component, select 2D Axisymmetric.
45. Rename component 2 (comp2) to Impeller Core.
46. Change Length unit to mm.

47. In the Geometry toolbar, select Circular Arc.
48. Under Properties, change to Endpoints and start angle.
49. For Starting Point, fill in r: 0, z: 20.29.
50. For Endpoint fill in: r: 1.29, z: 19.
51. For Angles fill in Starta angle: 90 deg, and check Clockwise.
52. In the Geometry toolbar, select Polygon.
53. For Object Type, change to Open curve.
54. Fill in:

r (mm)	z (mm)
2.13	19
1.29	19

55. In the Geometry toolbar, select Interpolation Curve.
56. For Object Type, change to Open curve.
57. Fill in:

r (mm)	z (mm)
2.13	19
2.13	16.4
2.11	15.9
2.41	10.2
2.76	8.6
4.2	4.64
4.64	1.71

58. In the Geometry toolbar, select Circular Arc.
59. Under Properties, change to Endpoints and radius.
60. For Starting Point, fill in r: 4.64, z: 1.71.
61. For Endpoint fill in: r: 6.62, z: 0.
62. For Radius fill in 2.
63. Under Angles check Short arc.
64. In the Geometry toolbar, select Polygon.
65. For Object Type, change to Open curve.
66. Fill in:

r (mm)	z (mm)
6.62	0
16.05	0

16.05	6.3
14.1	6.3

67. In the Geometry toolbar, select Circular Arc.
68. Under Properties, change to Endpoints and radius.
69. For Starting Point, fill in: r: 4.17738, z: 15.04
70. For Endpoint, fill in r: 14.09998, z: 10.
71. For Radius, fill in 10.
72. Under Angles, select Short arc.
73. In the Geometry toolbar, select Polygon.
74. Under Object Type, change to Open curve.
75. Fill in:

r (mm)	z (mm)
3.29	22
4.17737956614	15.04

76. In the Geometry toolbar, select Quadratic Bezier.
77. For Control points, fill in:

r (mm)	z (mm)
1: 0	32.68
2: 1.92833	32.68
3: 3.29	22

78. For Weights, fill in:

1: 1
2: 1/sqrt(2)
3: 1

79. In the Geometry toolbar, select Polygon.
80. Under Object Type, change to Open curve.
81. Fill in:

r (mm)	z (mm)
0	32.68
0	20.29

82. Form Union.

GEOMETRY 3: large vane

23. Click Add Component, select 2D.

24. Rename component 3 (comp3) to Large Vane.
25. Change Length unit to mm.
26. In the Geometry toolbar, select Polygon.
27. Under Object Type, change to Open curve.
28. Fill in:

r (mm)	z (mm)
15.41	4.4
15.55	7.46

29. In the Geometry toolbar, select Quadratic Bezier.
30. For Control Points, fill in:

r (mm)	z (mm)
1: 15.55	7.46
2: 15.55	10.98
3: 12.31	10.98

31. For Weights, fill in:

1: 1
2: 1/sqrt(2)
3: 1

32. In the Geometry toolbar, select Quadratic Bezier.
33. For Control Points, fill in:

r (mm)	z (mm)
1: 12.31	10.98
2: 10.6815	10.98
3: 9.56	12.58

34. For Weights, fill in:

1: 1
2: 1/sqrt(2)
3: 1

35. In the Geometry toolbar, select Polygon.
36. Under Object Type, change to Open curve.
37. Fill in:

r (mm)	z (mm)

9.56	12.58
8.06	14.72

38. In the Geometry toolbar, select Quadratic Bezier.
39. For Control Points, fill in:

r (mm)	z (mm)
1: 8.06	14.72
2: 7.66516	15.2833
3: 6.95	15.12

40. For Weights, fill in:

1: 1
2: 1/sqrt(2)
3: 1

41. In the Geometry toolbar, select Polygon.
42. Under Object Type, change to Open curve.
43. Fill in:

r (mm)	z (mm)
6.95	15.12
3.14	14.25
2.35	14.16
2.35	11
10	4.4
15.41	4.4

44. Form Union.

GEOMETRY 4: small vane

16. Click Add Component, select 2D.
17. Rename Component 4 (comp4) to Small Vane.
18. Change Length unit to mm.
19. In the Geometry toolbar, select Polygon.
20. Fill in:

r (mm)	z (mm)
-15.41	4.4

-15.63	7.13
-15.66	7.46
-15.41	4.4
-9.5	4.4
-7.07	6.5
-8.11	14.72
-8.11	8.11
-9.9	10.89

21. In the Geometry toolbar, select Quadratic Bezier.
22. For Control Points, fill in:

r (mm)	z (mm)
1: -15.66	7.46
2: -15.66	10.98
3: -12.39	10.98

23. For Weights, fill in:

1: 1
2: 1/sqrt(2)
3: 1

24. In the Geometry toolbar, select Quadratic Bezier.
25. For Control Points, fill in:

r (mm)	z (mm)
1: -12.39	10.98
2: -11.29	10.98
3: -11.23	11.28

26. For Weights, fill in:

1: 1
2: 1/sqrt(2)
3: 1

27. In the Geometry toolbar, select Quadratic Bezier.
28. For Control Points, fill in:

r (mm)	z (mm)
1: -11.23	10.98
2: -10.5	11.7
3: -9.9	10.89

29. For Weights, fill in:

1: 1
2: 1/sqrt(2)
3: 1

30. Form Union.

GEOMETRY 5: nylon ball

1. Click Add Component, select 3D.
2. Rename Component 5 (comp5) to Nylon Ball.
3. Change Length unit to mm.
4. In the Geometry toolbar, select Sphere.
5. Set Radius to 1.19.
6. Under Position, fill in x: 0, y: 0, z: 19.
7. Form Union.

GEOMETRY 6: axis

1. Click Add Component, select 3D structure.
2. Rename Component 6 (comp6) to Axis.
3. Change Length unit to mm.
4. In the Geometry toolbar, select Cylinder.
5. Set Radius to 1.5, Height to 20.5.
6. Under Position, fill in x: 0, y: 0, z: -2.19.
7. In the Geometry, select Sphere.
8. Set Radius to 2.5.
9. Under Position, fill in x: 0, y: 0, z: 20.31.
10. In the Geometry toolbar, select Booleans and Partitions, select Difference.
11. For Objects to add, select cyl1. For Objects to subtract, select sph1.
12. In the Geometry toolbar, select Cone.
13. For Bottom radius, fill in 1.2. For Height, fill in: 0.3. Change Specify top size using to Radius. For Top radius, fill in 1.5.
14. Under Position, fill in x: 0, y: 0, z: -2.49.
15. Form Union.

GEOMETRY 7: axis base

21. Click Add Component, select 2D axisymmetric.
22. Rename Component 7 (comp7) to Axis Base.

23. Change Length unit to mm.
24. In the Geometry toolbar, select Polygon.
25. Under Object Type, select Open curve.
26. Fill in:

r (mm)	z (mm)
7.3	-0.8
18.41	-0.8
18.75	1.12
18.95	1.12
19.15	0.92
19.22	-2.8
0	-2.8
0	-2.49
1.5	-2.49
1.5	7.24
1.93	6.57
2.41	5.37
2.62	4.6
2.85	3.04

27. In the Geometry toolbar, select Circular Arc.
28. Under Properties, change to Endpoints and radius.
29. For Starting Point, fill in: r: 2.85, z: 3.04.
30. For Endpoint, fill in: r: 7.3, z: -0.8.
31. Set Radius to 4.5. Select Short Arc.
32. Form Union.

GEOMETRY 8: magnets

1. Click Add Component, select 3D.
2. Rename Component 8 (comp8) to Magnets.
3. Change Length unit to mm.
4. In the Geometry toolbar, select Cylinder.
5. For Radius, fill in: 3. For Height, fill in: 4.
6. For Position fill in x: 10, y: 0: z: 0.5.
7. In the Geometry toolbar, select Transforms, select Copy.

8. Select cyl1.
9. In the Geometry toolbar, select Transforms, select Rotate.
10. Select copy1. For Rotation, specify: Axis of rotation. Axis type: z-axis. Angle: 90 deg.
11. In the Geometry toolbar, select Transforms, select Copy.
12. Select cyl1.
13. In the Geometry toolbar, select Transforms, select Rotate.
14. Select copy2. For Rotation, specify: Axis of rotation. Axis type: z-axis. Angle: 180 deg.
15. In the Geometry toolbar, select Transforms, select Copy.
16. Select cyl1.
17. In the Geometry toolbar, select Transforms, select Rotate.
18. Select copy3. For Rotation, specify: Axis of rotation. Axis type: z-axis. Angle: 270 deg.
19. Form Union.

GEOMETRY 9: hole

1. Click Add Component, select 2D.
2. Rename Component 9 (comp9) to Hole.
3. Change Length unit to mm.
4. In the Geometry toolbar, select Polygon.
5. Fill in:

r (mm)	z (mm)
17.63	-1.3
19	-1.37
19	1.37
17.63	1.3

6. In the Geometry toolbar, select Circular Arc.
7. Specify: Center, radius, angles.
8. For Center, fill in: x: 17.63, y: 0.
9. For Radius fill in Radius: 1.3
10. For Angles, fill in Starting angle: 90, End angle: -90.
11. In the Geometry toolbar, select Conversions, select Convert to Solid.
12. Select pol1 and ca1.
13. Form Union.

GEOMETRY 1: complete 3D geometry

1. In the Geometry toolbar, select Work plane.
2. In Plane Definition, for Plane, choose xz-plane. For y-coordinate, fill in: 4.61.
3. From the Work Plane toolbar, select Import.
4. In Import, for Source, choose Geometry sequence, select Impeller Core.
5. Import.
6. In the Work Plane toolbar, select Fillet.
7. Select the bottom lateral corner of the geometry.

8. Fill in Radius: 1.44.
9. In the Work Plane toolbar, select Fillet.
10. Select the top lateral corner of the geometry.
11. Fill in Radius: 1.87.
12. In the Work Plane toolbar, select Conversions, select Convert to Solid.
13. Select the complete geometry outline.
14. In the Geometry toolbar, select Revolve, select wp1.
15. In the Geometry toolbar, select Work plane.
16. In Plane Definition, for Plane, choose xz-plane.
17. From the Work Plane toolbar select Import.
18. In Import, for Source, choose Geometry sequence, for Geometry, select Large Vane.
19. Import.
20. In the Work Plane toolbar, select Conversions, select Convert to Solid.
21. Select the complete geometry outline.
22. In the Geometry toolbar, select Extrude, select wp2.
23. In Distances, specify Distances from plane. Fill in 1.33.
24. In the Geometry toolbar, select Transforms, select Copy.
25. Select ext1.
26. In the Geometry toolbar, select Transforms, select Rotate.
27. Select copy1.
28. In Rotation, specify: axis of rotation, Axis type: z-axis, Angle: 120 deg.
29. In the Geometry toolbar, select Transforms, select Copy.
30. Select ext1.
31. In the Geometry toolbar, select Transforms, select Rotate.
32. Select copy2.
33. In Rotation, specify: axis of rotation, Axis type: z-axis, Angle: 240 deg.
34. In the Geometry toolbar, select Work plane.
35. In Plane Definition, for Plane, choose xz-plane. For y-coordinate, fill in: -4.61.
36. From the Work Plane toolbar, select Import.
37. In Import, for Source, choose Geometry sequence, for Geometry, select Small Vane.
38. Import.
39. In the Work Plane toolbar, select Conversions, select Convert to Solid.
40. Select the complete geometry outline.
41. In the Geometry toolbar, select Extrude, select wp3.
42. In Distances, specify Distances from plane. Fill in -1.34.
43. In the Geometry toolbar, select Transforms, select Copy.
44. Select ext2.
45. In the Geometry toolbar, select Transforms, select Rotate.
46. Select copy3.
47. In Rotation, specify: axis of rotation, Axis type: z-axis, Angle: 120 deg.
48. In the Geometry toolbar, select Transforms, select Copy.
49. Select ext2.
50. In the Geometry toolbar, select Transforms, select Rotate.
51. Select copy4.

52. In Rotation, specify: axis of rotation, Axis type: z-axis, Angle: 240 deg.
53. In the Geometry toolbar, select Import.
54. For Source, select Geometry sequence. Select Nylon Ball.
55. Import.
56. In the Geometry toolbar, select Work Plane.
57. In Plane Definition, for Plane, select zy-plane.
58. In the Work Plane toolbar, select Import.
59. For Source, select Geometry sequence. Select Hole.
60. Import.
61. In the Geometry toolbar, select Extrude. Select wp4.
62. In Distances, specify: Distances from plane.
63. Fill in:

5
-5

64. Check Reverse direction.
65. In the Geometry toolbar, select Booleans and Partitions, select Difference.
66. For Objects to add, select rev1.
67. For Objects to subtract, select ext3.
68. In the Geometry toolbar, select Import.
69. For Source, select Geometry sequence, select Axis.
70. Import.
71. In the Geometry toolbar, select Work Plane.
72. In Plane Definition, for Plane, select yz-plane.
73. In the Work Plane toolbar, select Import.
74. For Source, select Geometry sequence. Select Axis Base.
75. In the Work Plane toolbar, select Conversions, select Convert to Solid.
76. Select the complete geometry outline.
77. In the Geometry toolbar, select Revolve. Select wp5.
78. In the Geometry toolbar select Import.
79. For Source, select Geometry sequence. Select Magnets.
80. In the Geometry toolbar, select Booleans and Partitions, select Difference.
81. For Objects to add, select dif1.
82. For Objects to subtract, select imp3.
83. Check Keep objects to subtract.
84. In the Geometry toolbar, select Booleans and Partitions, select Union.
85. Select ext1, rot1, rot2, ext2, rot3, rot4, imp1, imp3, dif2.
86. In the Geometry toolbar, select Booleans and Partitions, select Union.
87. Select imp2, rev2.
88. Select Form Union.
89. Under Action, change to Form an assembly.
90. Build All.

9.3 Modelling instructions CFD model

From the File menu, choose New.

NEW
In the New window, click Model Wizard.

MODEL WIZARD

1. In the Model Wizard window, click 3D.
2. In the Select Physics tree, select Fluid FLow>Single-Phase Flow>Rotating Machinery, Fluid Flow>Turbulent Flow>Turbulent Flow, k-ω
3. Click Add.
4. Click Study.
5. In the Select Study tree, select Preset Studies for Selected PHysics Interfaces>Frozen Rotor with Initialization.
6. Click Done.

GLOBAL DEFINITIONS:

1. For the Global Parameters, fill in:

Name	Expression	Value	Description
a1	20.66	20.66	Initial spiral radius
af	23.61	23.61	Final spiral radius
n1	1	1	Number of turns
thick	0	0	Thickness of the spiral
theta_0	0	0	Initial angle
theta_f	(af-a1)/b1	6.2832	Final angle
b1	(af-a1)/(2*pi*n1)	0.46951	Spiral growth rate
b2	distance/(2*pi)	0.46951	Updated growth rate
distance	(af-a1)/n1	2.95	Turn to turn distance
gap	distance-thick	2.95	gap
r_tube_begin	1.945	1.945	Initial radius tube
r_tube_end	4.255	4.255	Final radius tube
factor	(r_tube_end/r_tube_begin) /134.48	0.0088315	Growth rate of the diameter of the spiral

GEOMETRY 1: fluid around the impeller

1. Rename Component 1 to Fluid around the Impeller
2. In the Geometry toolbar, select Work Plane.
3. Under Plane Definition, set Plane: xz-plane.
4. In the Work Plane toolbar, select Polygon.
5. Fill in:

xw (mm)	yw (mm)
5.19	36.38
0	36.38
0	-2.8
17.79	-2.8
17.79	7.47
17.76	8.81

6. In the Work Plane toolbar, select Circular Arc.
7. Specify: Endpoints and radius.
8. For Starting Point, fill in: xw: 5.19, yw: 36.38.
9. For Endpoint, fill in: xw: 8.66, yw: 18.17.
10. For Radius, fill in: Radius: 64.12. For Angles, check Short arc.
11. In the Work Plane toolbar, select Circular Arc.
12. Specify: Endpoints and radius.
13. For Starting Point, fill in: xw: 8.66, yw: 18.17.
14. For Endpoint, fill in: xw: 9.83, yw: 15.84.
15. For Radius, fill in: Radius: 10.05. For Angles, check Short arc.
16. In the Work Plane toolbar, select Circular Arc.
17. Specify: Endpoints and radius.
18. For Starting Point, fill in: xw: 9.83, yw: 15.84.
19. For Endpoint, fill in: xw: 11.3, yw: 13.88.
20. For Radius, fill in: Radius: 24.92. For Angles, check Short arc.
21. In the Work Plane toolbar, select Circular Arc.
22. Specify: Endpoints and radius.
23. For Starting Point, fill in: xw: 11.3, yw: 13.88.
24. For Endpoint, fill in: xw: 13.76, yw: 12.68.
25. For Radius, fill in: Radius: 3.32. For Angles check Short arc.
26. In the Work Plane toolbar, select Circular Arc.
27. Specify: Endpoints and radius.
28. For Starting Point, fill in: xw: 13.76, yw: 12.68.
29. For Endpoint, fill in: xw: 17.76, yw: 8.81.
30. For Radius, fill in: Radius: 4.06. For Angles, check Short arc.
31. In the Work Plane toolbar, select Conversions, select Convert to Solid.
32. Select the complete geometry outline.

33. In the Geometry toolbar, select Revolve.
34. Select wp1.
35. In the Geometry toolbar, select Import.
36. In Import, for Source, choose Geometry sequence, for Geometry, select complete 3D geometry. (the geometry created in the 3D model for the numerical eigenfrequency analysis)
37. Import.
38. In the Geometry toolbar, select Booleans and Partitions, select Difference.
39. For Object to add, select rev1.
40. For Objects to subtract, select imp1.
41. In the Geometry toolbar, select Cylinder.
42. For Object Type, change to Type: Solid.
43. For Size and Shape, fill in: Radius: 21.29, Height: 3.1.
44. For Position, fill in: x: 0, y: 0, z: 4.37.
45. In the Geometry toolbar, select Booleans and Partitions, select Difference.
46. For Objects to add, select cyl1.
47. For Objects to subtract, select dif1.
48. Check Keep objects to subtract.
49. In the Geometry toolbar, select Work Plane.
50. In Plane Definition, change Plane type to Coordinates. For Point 1;z, Point 2;z, Point 3;z fill in z: -197333.
51. In the Work Plane toolbar, select Parametric Curve.
52. In Parameter, fill in Name: s, Minimum: theta_0, Maximum: theta_f.
53. In Expressions, fill in xw: X_sprial(s)+N_x(s)*thick/2, yw: Y_spiral(s)+N_y(s)*thick/2
54. In the Geometry toolbar, select Work Plane.
55. In Plane definition, change Plane to xz-plane.
56. In the Work Plane toolbar, select Circle.
57. For Object Type, select Solid.
58. For Size and Shape, fill in: Radius: r_tube_begin, Sector angle: 360.
59. In the Geometry toolbar, select Sweep.
60. For Faces to sweep select wp3. For Edges to follow, select wp2.
61. Check Smooth edge connections.
62. Set Parameterization to Arc length.
63. Under Motion of Cross Section, set Parameter name: s, Scale factor: 1+factor*s, Twist angle: 0.
64. Check Twist compensation.
65. Set Face-spine alignment to No adjustment.
66. In the Geometry toolbar, select Extrude.
67. Set Extrude from to Work plane and for Work plane, select Work Plane 3. Set wp3 as Input objects.
68. Under Distances, specify Distances from plane and fill in 10.5.
69. In the Geometry toolbar, select Cone.
70. For Object Type, select Solid.

71. Fill in: Bottom radius: 5.19, Height: 20.05, Specify top size using: Radius, Top radius: 4.65.
72. For Position, fill in: x: 0, y: 0, z: 36.38.
73. Axis type set to z-axis.
74. In the Geometry toolbar, select Cone.
75. For Object Type, select Solid.
76. Fill in: Bottom radius: 5.19, Height: 24.54, Specify top size using: Radius, Top radius: 4.255.
77. For Position, fill in: x: -23.59, y: -24.54, z: 8.55.
78. Axis type set to y-axis.
79. In the Geometry toolbar, select Cone.
80. For Object Type, select Solid.
81. Fill in: Bottom radius: 5.19, Height: 16.65, Specify top size using: Radius, Top radius: 4.65.
82. For Position, fill in: x: 23.59, y: 24.54, z: 8.55.
83. Axis type set to y-axis.
84. In the Geometry toolbar, select Transforms, select Rotate.
85. Select cone3.
86. Under Rotation, specify Axis of rotation, Axis type: z-axis, and Angle: 180 deg.
87. Form Union.

9.4 List of performance variables of the CFD model

Table 18. list of performance variables used in the CFD model

Name	Expression	Description
rhoRef	aveop2(spf.rhoref)	Reference density
delta_p	int_out(p)/int_out(1)-int_in(p)/int_in(1)	Static pressure increase
detta_p_tot	((int_out(p+1/2*rhoRef*spf.U^2)/int_out(1)-int_in(p+1/2*rhoRef*spf.U^2)/int_in(1)))	Total pressure increase
Torque	int_rot(+spf.T_stressx*y-spf.T_stressy*x)	Torque
Power	abs(int_rot(rot1.alphat)*Torque/int_rot(1))	Shaft power consumption
flowrate	int_in(u*nx+v*ny+w*nz)	Flow rate
massflow	rhoRef*flowrate	Mass flow
H_power	abs(massflow*delta_p_tot/rhoRef)	Power given to fluid
H	delta_p_tot/(rhoRef*g_const)	Head
eta	H_power/Power	Pump efficiency

9.5 List of eigenfrequencies 2D model

Table 19. List of the 60 determined eigenfrequencies of the 2D model

Eigenfrequency (Hz)	Angular frequency (rad/s)
204.56	1285.3
220.38	1384.7
2387.4	15001
3107.7	19526
4087.2	25681
7109.4	44670
9192.3	57757
17296	1.09E+05
26397	1.66E+05
26949	1.69E+05
28804	1.81E+05
33586	2.11E+05
36518	2.29E+05
38036	2.39E+05
38527	2.42E+05
43987	2.76E+05
48186	3.03E+05
50567	3.18E+05
53657	3.37E+05
55417	3.48E+05
61744	3.88E+05
62085	3.90E+05
65570	4.12E+05
67882	4.27E+05
69218	4.35E+05
73908	4.64E+05
74564	4.69E+05
77162	4.85E+05

77636	4.88E+05
79347	4.99E+05
83098	5.22E+05
84135	5.29E+05
85305	5.36E+05
88061	5.53E+05
91843	5.77E+05
93014	5.84E+05
95452	6.00E+05
97825	6.15E+05
1.01E+05	6.33E+05
1.02E+05	6.41E+05
1.05E+05	6.59E+05
1.07E+05	6.70E+05
1.08E+05	6.80E+05
1.10E+05	6.94E+05
1.12E+05	7.03E+05
1.13E+05	7.10E+05
1.14E+05	7.16E+05
1.16E+05	7.28E+05
1.18E+05	7.42E+05
1.19E+05	7.46E+05
1.20E+05	7.55E+05
1.22E+05	7.66E+05
1.23E+05	7.73E+05
1.26E+05	7.89E+05
1.28E+05	8.02E+05
1.29E+05	8.10E+05
1.31E+05	8.25E+05
1.32E+05	8.28E+05
1.33E+05	8.34E+05
1.34E+05	8.39E+05

9.6 List of eigenfrequencies of 3D model

Table 20. List of the 60 determined eigenfrequencies of the 3D model.

Eigenfrequency (Hz)	Angular frequency (rad/s)
0.0038489i	0.024183i
0.0062780i	0.039446i
0.0032172	0.020214
0.0046775	0.02939
0.0062658	0.039369
0.008785	0.055198
5207.9	32722
5667.3	3.56E+04
7139.5	4.49E+04
8993.7	5.65E+04
12033	7.56E+04
12090	7.60E+04
12205	7.67E+04
12776	8.03E+04
13202	8.29E+04
13568	8.53E+04
13640	8.57E+04
13795	8.67E+04
14547	9.14E+04
14998	9.42E+04
15390	9.67E+04
15669	9.85E+04
16235	1.02E+05
16705	1.05E+05
18025	1.13E+05
18076	1.14E+05
18470	1.16E+05
18677	1.17E+05
20164	1.27E+05

20319	1.28E+05
20621	1.30E+05
20791	1.31E+05
21153	1.33E+05
24280	1.53E+05
24736	1.55E+05
25483	1.60E+05
26059	1.64E+05
26820	1.69E+05
2.72E+04	1.71E+05
2.75E+04	1.73E+05
2.75E+04	1.73E+05
2.78E+04	1.75E+05
2.83E+04	1.78E+05
2.85E+04	1.79E+05
3.03E+04	1.90E+05
3.06E+04	1.92E+05
3.06E+04	1.93E+05
3.08E+04	1.93E+05
3.16E+04	1.99E+05
3.26E+04	2.05E+05
3.36E+04	2.11E+05
3.40E+04	2.14E+05
3.45E+04	2.17E+05
3.54E+04	2.23E+05
3.59E+04	2.25E+05
3.61E+04	2.27E+05
3.66E+04	2.30E+05
3.70E+04	2.32E+05
3.75E+04	2.35E+05
3.77E+04	2.37E+05

9.7 Mean output parameters of the performance test and stability experiment

Table 21. Mean output values R1: 6.6 mm diameter.

Resistor:	R1: 6.6 mm diameter						
Rotational speed of cirQlife pump [RPM]	3500	4000	4500	5000	5500	6000	6500
Q1 [L/min]	5.584	6.519	7.467	8.384	9.348	*10.366	*10.406
Standard deviation Q1 [L/min]	0.131	0.154	0.168	0.192	0.247	*0.251	*0.263
P1 (suction pressure) [mmHg]	-28.80	-38.80	-48.80	-60.00	-75.50	*-98.00	*-98.00
Standard deviation P1 [mmHg]	2.3	0.919	2.098	0.000	2.838	*2.739	*2.739
P2 (discharge pressure) [mmHg]	93.50	124.70	160.00	199.00	243.50	*306.00	*306.00
Standard deviation P2 [mmHg]	2.415	0.949	0.000	2.108	6.687	*8.944	*8.944
H Pressure Head (m)	1.689	2.250	2.868	3.551	4.369	*5.526	*5.526
Stability observation (*/**/***/****/*****)	* (100%)	* (100%)	* (100%)	* (60%) ** (40%)	** (10%) *** (75%) **** (15%)	**** (70%) ***** (30%)	**** (60%) ***** (40%)

Table 22. Mean output values R2: 5.6 mm diameter.

Resistor:	R2: 5.6 mm diameter						
Rotational speed of cirQlife pump [RPM]	3500	4000	4500	5000	5500	6000	6500
Q1 [L/min]	5.362	6.257	7.179	8.055	8.983	*10.088	*10.160
Standard deviation Q1 [L/min]	0.201	0.222	0.247	0.275	0.297	*0.314	*0.365
P1 (suction pressure) [mmHg]	-25.40	-35.00	-43.60	-55.60	-66.50	*-90.00	*-91.00
Standard deviation P1	1.897	0.000	1.578	1.265	4.743	*6.124	*6.519

[mmHg]							
P2 (discharge pressure) [mmHg]	95.70	126.00	163.00	205.00	252.00	*315.00	*315.00
Standard deviation P2 [mmHg]	1.636	6.733	4.830	2.357	10.328	*8.660	*8.660
H Pressure Head (m)	1.673	2.216	2.838	3.573	4.362	*5.540	*5.554
Stability observation (*/**/***/****/*****)	* (100%)	* (100%)	* (100%)	* (50%) ** (50%)	** (20%) *** (65%) **** (15%)	**** (55%) ***** (45%)	**** (50%) ***** (50%)

Table 23. Mean output values R3: 5.2 mm diameter.

Resistor:	R3: 5.2 mm diameter						
Rotational speed of cirQlife pump [RPM]	3500	4000	4500	5000	5500	6000	6500
Q1 [L/min]	5.055	5.922	6.776	7.611	8.458	*9.698	*9.778
Standard deviation Q1 [L/min]	0.058	0.089	0.111	0.119	0.130	*0.181	*0.101
P1 (suction pressure) [mmHg]	-24.00	-31.20	-40.70	-50.50	61.00	*-85.00	*-87.00
Standard deviation P1 [mmHg]	1.247	2.098	1.636	1.581	2.108	*7.071	*4.472
P2 (discharge pressure) [mmHg]	99.00	131.50	169.50	210.50	257.50	*322.00	*322.00
Standard deviation P2 [mmHg]	2.108	2.415	1.581	1.581	7.546	*4.472	*4.472
H Pressure Head (m)	1.699	2.240	2.887	3.579	2.700	*5.567	*5.594
Stability observation (*/**/***/****/*****)	* (100%)	* (100%)	* (100%)	* (70%) ** (30%)	** (20%) *** (80%)	**** (60%) ***** (40%)	**** (50%) ***** (50%)

Table 24. Mean output values R4: 4.4 mm diameter.

Resistor:	R4: 4.4 mm diameter

Rotational speed of cirQlife pump [RPM]	3500	4000	4500	5000	5500	6000	6500
Q1 [L/min]	4.315	4.993	5.712	6.422	7.169	*8.136	*8.298
Standard deviation Q1 [L/min]	0.120	0.152	0174	0.189	0.305	*0.084	*0.113
P1 (suction pressure) [mmHg]	-18.200	-22.200	-30.000	-38.600	-44.800	*-54.00	*-58.00
Standard deviation P1 [mmHg]	0.632	1.033	0.000	0.966	2.201	*5.477	*4.472
P2 (discharge pressure) [mmHg]	108.00	141.50	181.50	227.30	279.00	*364.00	*380.00
Standard deviation P2 [mmHg]	2.582	2.415	2.415	2.497	7.746	*8.944	*12.247
H Pressure Head (m)	1.742	2.253	2.904	3.645	4.434	*5.717	*5.989
Stability observation (*/**/***/****/*****)	* (100%)	* (100%)	* (100%)	* (70%) ** (30%)	** (30%) *** (70%)	**** (70%) ***** (30%)	**** (50%) ***** (50%)

Table 25. Mean output values R5: 3.8 mm diameter.

Resistor:	R5: 3.8 mm diameter						
Rotational speed of cirQlife pump [RPM]	3500	4000	4500	5000	5500	6000	6500
Q1 [L/min]	3.531	4.088	4.636	5.176	5.804	*6.594	*6.784
Standard deviation Q1 [L/min]	0.070	0.102	0.097	0.104	0.210	*0.068	*0.114
P1 (suction pressure) [mmHg]	-13.50	-18.00	-20.00	-22.40	-30.40	*-40.00	*-41.00
Standard deviation P1 [mmHg]	1.958	0.000	0.000	0.843	7.336	*0.000	*2.236
P2 (discharge pressure) [mmHg]	114.70	151.00	193.00	240.70	328.00	*388.00	*404.00
Standard deviation P2 [mmHg]	0.949	2.108	2.582	1.636	47.679	*4.472	*6.519
H Pressure Head (m)	1.770	2.325	2.925	3.607	4.905	5.853	6.085

Stability observation (*/**/***/****/*****)	* (100%)	* (100%)	* (100%)	* (60%) ** (40%)	** (20%) *** (70%) **** (10%)	**** (75%) ***** (25%)	**** (50%) ***** (50%)

9.8 Stability results table for sample 1-5;A-E

Table 26. Stability results of samples 1-5;A-E for all resistors at all rotational speeds.

RPM	3500	4000	4500	5000	5500	6000	6500
R1	* (100%)	* (100%)	* (100%)	* (60%) ** (40%)	** (10%) *** (75%) **** (15%)	**** (70%) ***** (30%)	**** (60%) ***** (40%)
R2	* (100%)	* (100%)	* (100%)	* (50%) ** (50%)	** (20%) *** (65%) **** (15%)	**** (55%) ***** (45%)	**** (50%) ***** (50%)
R3	* (100%)	* (100%)	* (100%)	* (70%) ** (30%)	** (20%) *** (80%)	**** (60%) ***** (40%)	**** (50%) ***** (50%)
R4	* (100%)	* (100%)	* (100%)	* (70%) ** (30%)	** (30%) *** (70%)	**** (70%) ***** (30%)	**** (50%) ***** (50%)
R5	* (100%)	* (100%)	* (100%)	* (60%) ** (40%)	** (20%) *** (70%) **** (10%)	**** (75%) ***** (25%)	**** (50%) ***** (50%)
Mean:	* (100%)	* (100%)	* (100%)	* (62%) ** (38%)	** (20%) *** (72%) **** (8%)	**** (66%) ***** (34%)	**** (52%) *****(48%)

9.9 Mean output parameters of the performance test and stability experiment for the altered samples with closed holes

Table 27. Mean output values R1: 6.6 mm diameter for the closed-hole design samples A*-E*.

Resistor:	R1: 6.6 mm diameter*						
Rotational speed of cirQlife pump [RPM]	3500	4000	4500	5000	5500	6000	6500
Q1 [L/min]	5.572	6.512	7.452	8.402	9.914	10.500	10.520
Standard deviation Q1 [L/min]	0.264	0.299	0.339	0.365	0.395	0.212	0.277

P1 (suction pressure) [mmHg]	-30.00	-38.80	-48.60	-60.00	-81.00	-96.00	-98.00
Standard deviation P1 [mmHg]	0.000	1.095	2.191	0.000	2.236	5.477	2.739
P2 (discharge pressure) [mmHg]	95.00	123.80	160.00	199.00	272.00	307.00	309.00
Standard deviation P2 [mmHg]	0.000	1.643	0.000	2.236	8.367	14.832	11.402
H Pressure Head (m)	1.726	2.238	2.865	3.551	4.832	5.513	5.567
Stability observation (*/**/***/****/*****)	*(100%)	*(80%) **(20%)	**(90%) ***(10%)	**(10%) ***(90%)	**** (100%)	**** (100%)	**** (100%)

Table 28. Mean output values R2: 5.6 mm diameter for the closed-hole design samples A*-E*.

Resistor:	R2: 5.6 mm diameter*						
Rotational speed of cirQlife pump [RPM]	3500	4000	4500	5000	5500	6000	6500
Q1 [L/min]	5.336	6.244	7.152	8.032	9.454	10.072	10.124
Standard deviation Q1 [L/min]	0.186	0.218	0.245	0.277	0.317	0.349	0.365
P1 (suction pressure) [mmHg]	-25.80	-35.60	-45.00	-55.00	-76.00	-86.00	-88.00
Standard deviation P1 [mmHg]	2.387	1.342	0.000	0.000	4.183	5.477	4.472
P2 (discharge pressure) [mmHg]	96.20	129.00	165.00	207.00	281.00	315.00	319.00
Standard deviation P2 [mmHg]	1.643	2.236	0.000	2.739	2.236	10.000	13.416
H Pressure Head (m)	1.685	2.265	2.884	3.592	4.886	5.485	5.567
Stability observation (*/**/***/****/*****)	*(100%)	*(100%)	*(30%) **(70%)	**(20%) ***(80%)	**** (100%)	**** (100%)	**** (100%)

Table 29. Mean output values R3: 5.2 mm diameter for the closed-hole design samples A*-E*.

Resistor:	R3: 5.2 mm diameter*						
Rotational speed of	3500	4000	4500	5000	5500	6000	6500

cirQlife pump [RPM]							
Q1 [L/min]	5.128	5.992	6.840	7.698	9.062	9.638	9.824
Standard deviation Q1 [L/min]	0.172	0.198	0.234	0.229	0.288	0.347	0.297
P1 (suction pressure) [mmHg]	-24.20	-30.80	-40.40	-50.00	-68.00	-80.00	-82.00
Standard deviation P1 [mmHg]	1.304	1.095	0.894	0.000	4.472	0.000	4.472
P2 (discharge pressure) [mmHg]	99.00	133.00	169.00	210.00	288.00	320.00	327.00
Standard deviation P2 [mmHg]	2.236	2.739	2.236	0.000	4.472	14.577	4.472
H Pressure Head (m)	1.702	2.255	2.876	3.565	4.872	5.472	5.594
Stability observation (*/**/***/****/*****)	*(100%)	*(100%)	*(20%) **(80%)	**(10%) ***(90%)	**** (100%)	**** (100%)	**** (100%)

Table 30. Mean output values R4: 4.4 mm diameter for the closed-hole design samples A*-E*.

Resistor:	R4: 4.4 mm diameter*						
Rotational speed of cirQlife pump [RPM]	3500	4000	4500	5000	5500	6000	6500
Q1 [L/min]	4.320	5.006	5.722	6.432	7.554	8.290	8.348
Standard deviation Q1 [L/min]	0.064	0.092	0.114	0.107	0.134	0.144	0.195
P1 (suction pressure) [mmHg]	-18.00	-23.00	-30.00	-38.80	-50.00	-60.00	-60.00
Standard deviation P1 [mmHg]	0.000	1.414	0.000	1.095	0.000	0.000	0.000
P2 (discharge pressure) [mmHg]	109.60	143.00	183.00	230.00	309.00	368.00	374.00
Standard deviation P2 [mmHg]	0.894	2.739	2.739	6.124	2.236	8.367	10.840
H Pressure Head (m)	1.7615 03098	2.2845 41523	2.9247 18762	3.6847 58972	4.9133 54438	5.8531 89108	5.9349 13862
Stability observation	*(100%)	*(100%)	*(20%)	***(90%)	****	****	****

(*/**/***/****/*****)			**(70%) ***(10%)	****(10%)	(100%)	(100%)	(100%)

Table 31. Mean output values R5: 3.8 mm diameter for the closed-hole design samples A*-E*.

Resistor:	R5: 3.8 mm diameter*						
Rotational speed of cirQlife pump [RPM]	3500	4000	4500	5000	5500	6000	6500
Q1 [L/min]	3.542	4.098	4.642	5.334	6.052	6.652	6.828
Standard deviation Q1 [L/min]	0.046	0.059	0.063	0.196	0.080	0.087	0.192
P1 (suction pressure) [mmHg]	-12.00	-18.00	-20.80	-29.00	-39.00	-43.00	-45.00
Standard deviation P1 [mmHg]	0.000	0.000	1.095	4.183	2.236	2.739	5.000
P2 (discharge pressure) [mmHg]	117.00	153.00	194.00	275.00	320.00	390.00	404.00
Standard deviation P2 [mmHg]	4.472	2.739	2.236	37.914	0.000	0.000	8.944
H Pressure Head (m)	1.781	2.353	2.949	4.164	4.913	5.921	6.139
Stability observation (*/**/***/****/*****)	*(100%)	*(100%)	*(20%) **(70%) ***(10%)	***(30%) ****(70%)	**** (100%)	**** (100%)	**** (100%)

9.10 Stability results table for sample A*-E*

Table 32. The mean stability results for sample A-E for each resistor for each rotational speed with the mean stability distribution for each rotational speed.

RPM	3500	4000	4500	5000	5500	6000	6500
R1	* (100%)	* (100%)	* (100%)	* (20%) ** (80%)	*** (100%)	**** (100%)	**** (100%)
R2	* (100%)	* (100%)	* (100%)	* (40%) ** (60%)	** (20%) *** (80%)	**** (100%)	**** (100%)
R3	* (100%)	* (100%)	* (100%)	* (40%) ** (60%)	** (20%) *** (80%)	**** (100%)	**** (100%)
R4	* (100%)	* (100%)	* (100%)	* (40%) ** (60%)	** (20%) *** (80%)	**** (100%)	**** (100%)

R5	* (100%)	* (100%)	* (100%)	* (40%) ** (60%)	** (20%) *** (80%)	**** (100%)	**** (100%)
mean:	* (100%)	* (100%)	* (100%)	* (36%) ** (64%)	** (16%) *** (84%)	**** (100%)	**** (100%)

Table 33. The mean stability results for sample A*-E* for each resistor for each rotational speed with the mean stability distribution for each rotational speed.

RPM	3500	4000	4500	5000	5500	6000	6500
R1	* (100%)	* (80%) ** (20%)	** (90%) *** (10%)	** (10%) *** (90%)	**** (100%)	**** (100%)	**** (100%)
R2	* (100%)	* (100%)	* (30%) ** (70%)	** (20%) *** (80%)	**** (100%)	**** (100%)	**** (100%)
R3	* (100%)	* (100%)	* (20%) ** (80%)	** (10%) *** (90%)	**** (100%)	**** (100%)	**** (100%)
R4	* (100%)	* (100%)	* (20%) ** (70%) *** (10%)	*** (90%) **** (10%)	**** (100%)	**** (100%)	**** (100%)
R5	* (100%)	* (100%)	* (20%) ** (70%) *** (10%)	*** (30%) **** (70%)	**** (100%)	**** (100%)	**** (100%)
mean:	* (100%)	* (96%) ** (4%)	* (18%) ** (76%) *** (6%)	** (8%) *** (76%) **** (16%)	**** (100%)	**** (100%)	**** (100%)

9.11 Additional figures

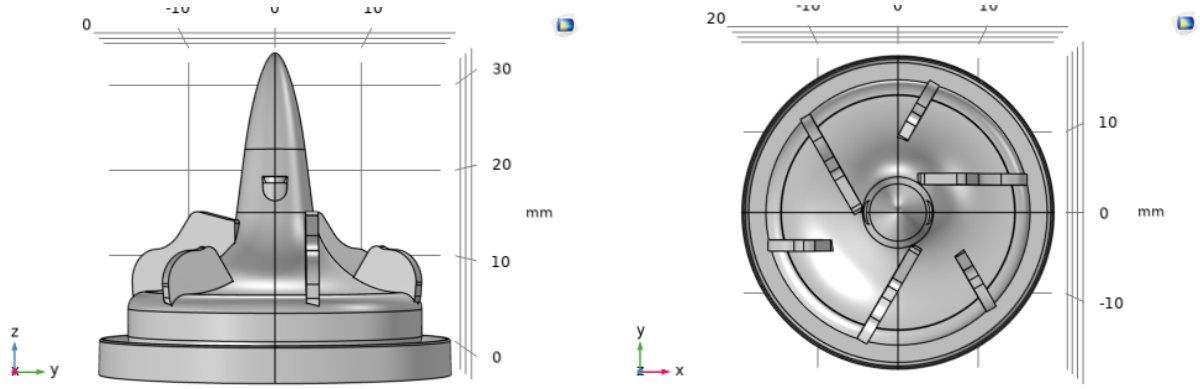

Figure 32. Additional figures of the Geometry of the 3D model of the impeller. Left: side view. Right: top view.

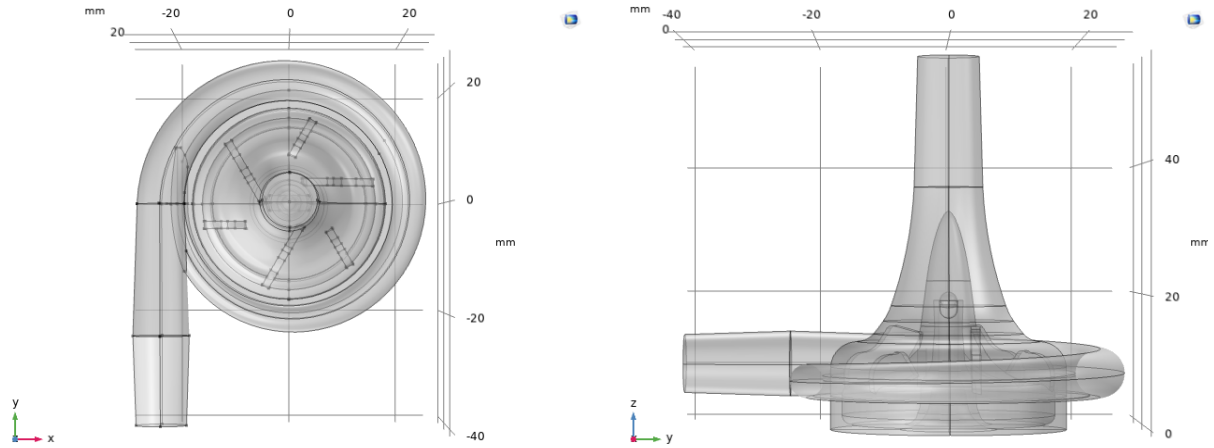

Figure 33. Additional figures of the geometry of the CFD model. Left: top view. Right: side view.

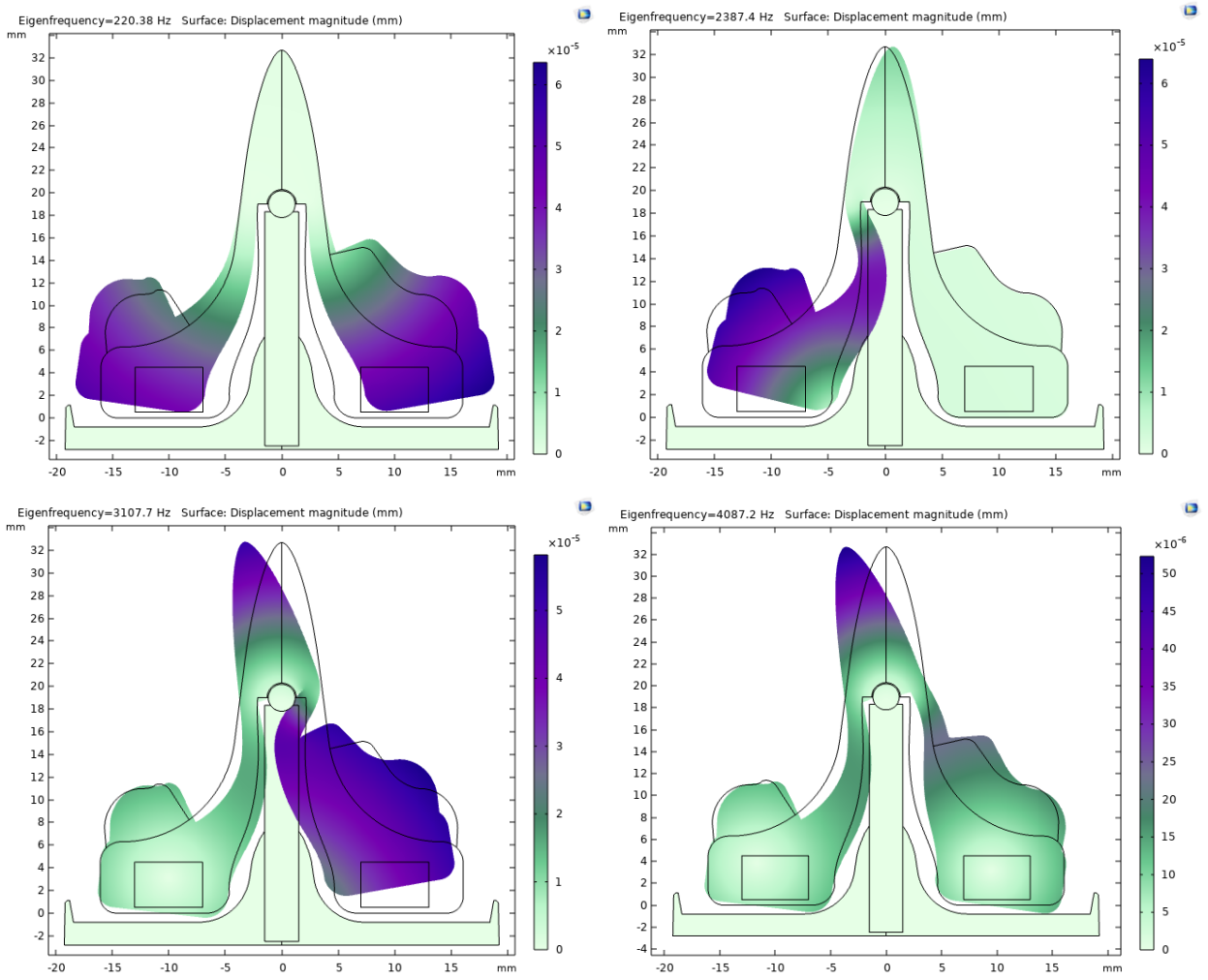

Figure 34. Mode shapes of the 2D model corresponding to simulated eigenfrequency two, three, four, and five. Top left: mode shape at 220.38 Hz. Top right: mode shape at 2387.4 Hz. Bottom left: mode shape at 3107.7 Hz. Bottom right: mode shape at 4087.2 Hz.

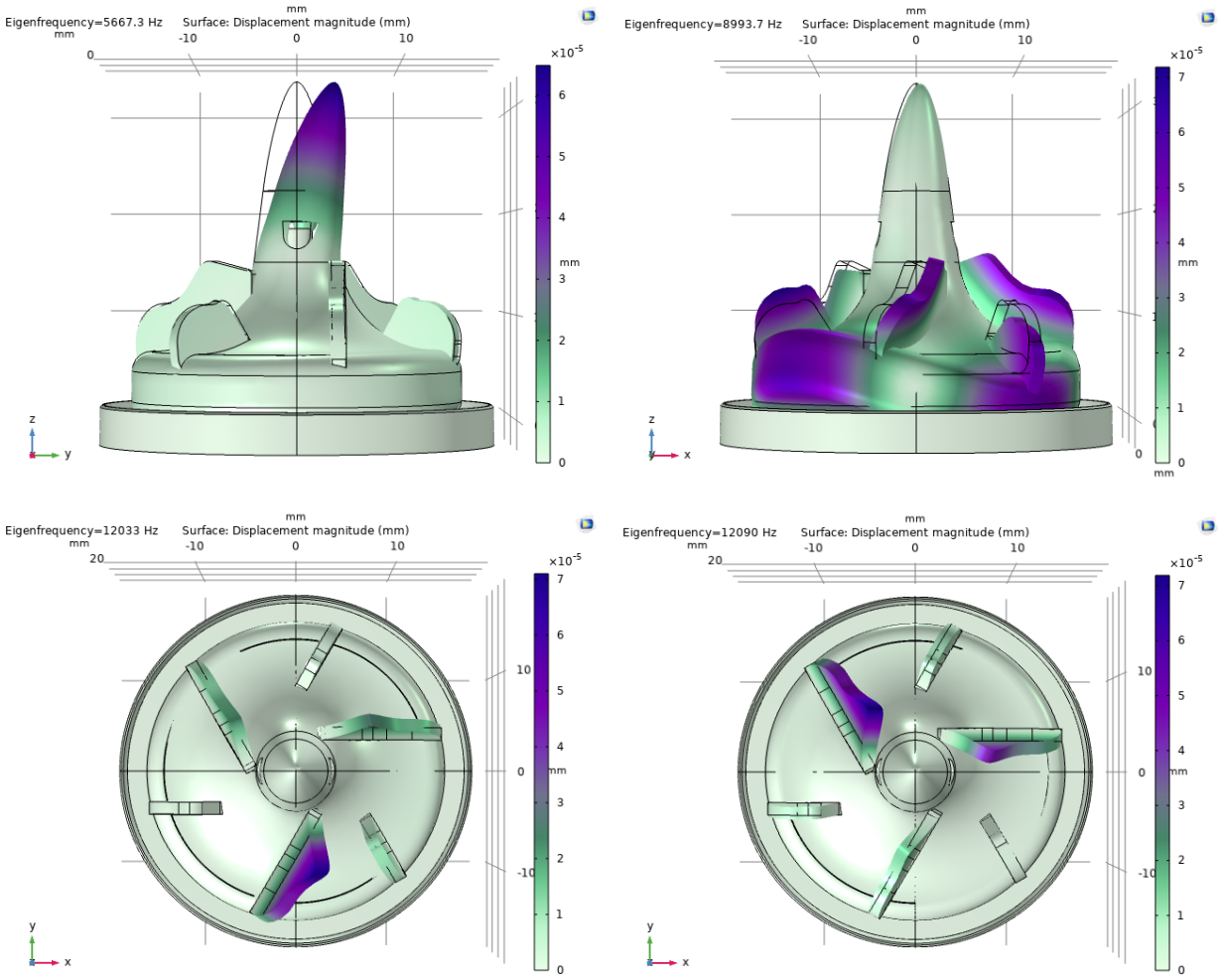

Figure 35. Mode shapes of the 3D model corresponding to simulated eigenfrequency eight, ten, eleven, and twelve. Top left: mode shape at 5667.3 Hz. Top right: mode shape at 8993.7 Hz. Bottom left: mode shape at 12033 Hz. Bottom right: mode shape at 12090 Hz.

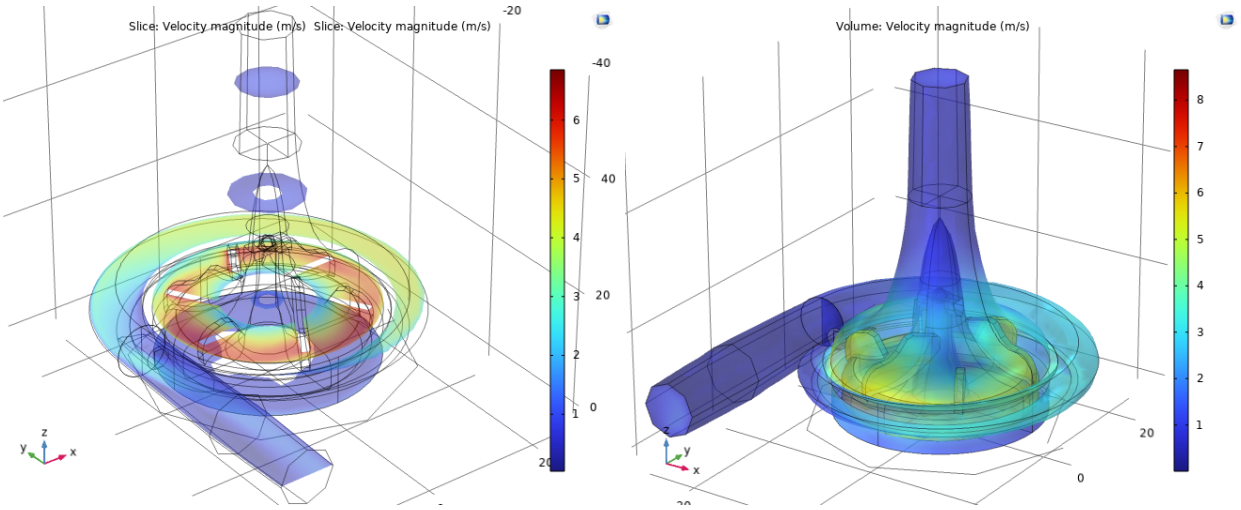

Figure 36. Additional figures of the fluid velocity in the pump model at 4000 RPM. Left: overview left side, horizontal cross-sections. Right: Overview right side, volume velocity.

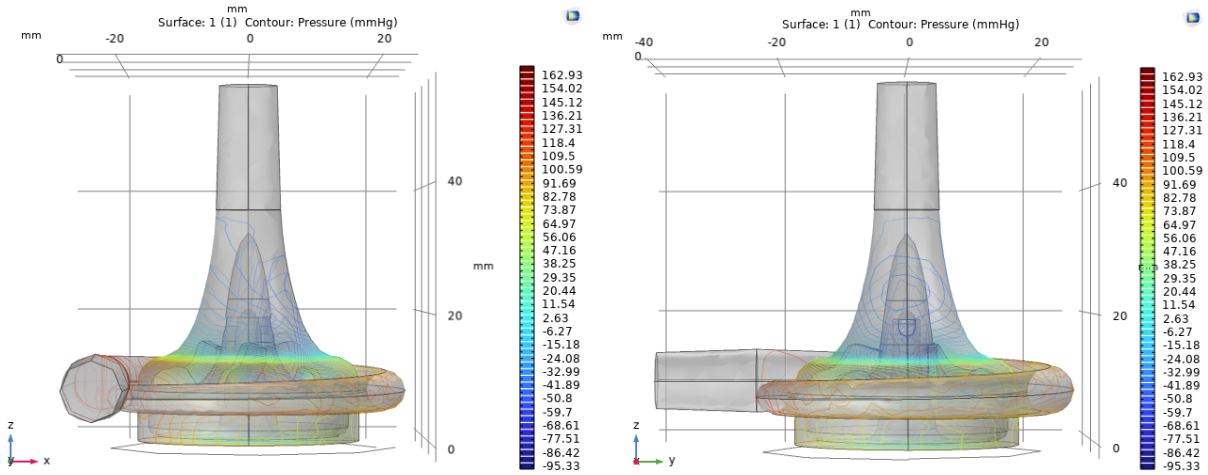

Figure 37. Additional figures of the pressure distribution in the fluid in the pump model at 4000 RPM. left: front view. Right: side view.

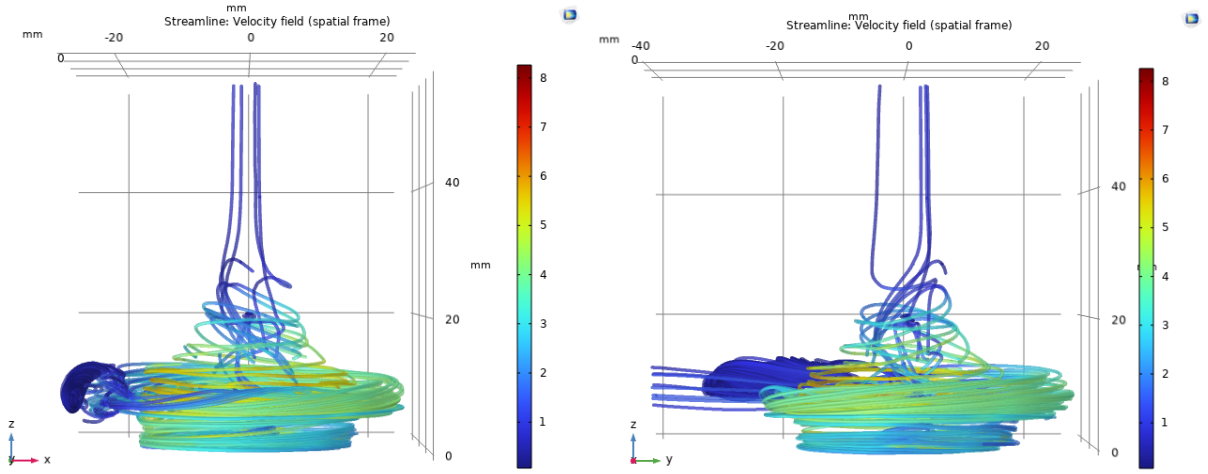

Figure 38. Additional figures of the velocity streamlines of the fluid in the pump model at 4000 RPM. Left: front view. Right: side view.

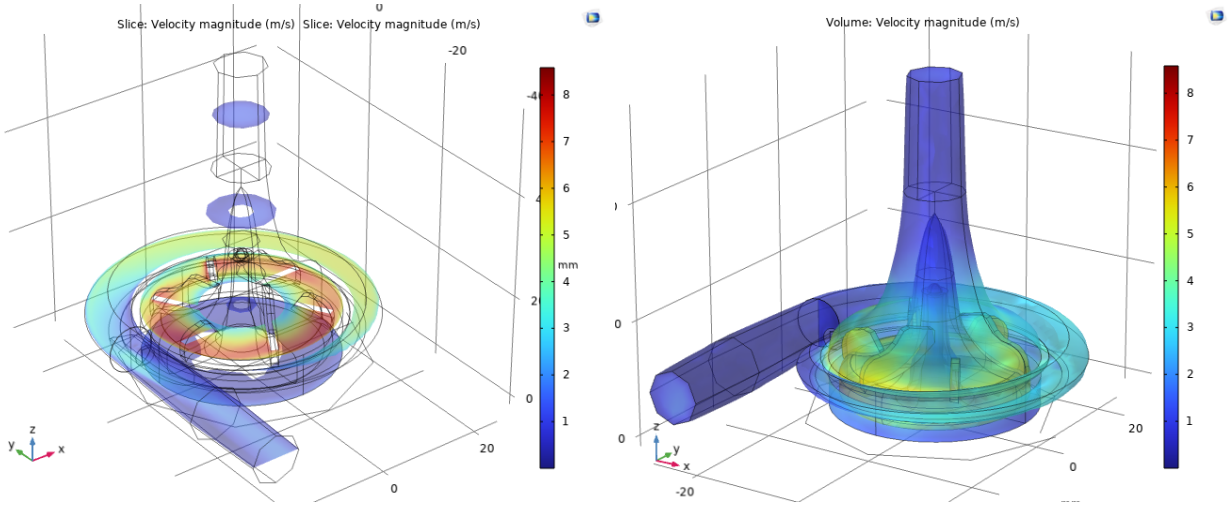

Figure 39. Additional figures of the fluid velocity in the closed impeller pump model at 4000 RPM. Left: overview left side, horizontal cross-sections. Right: Overview right side, volume velocity.

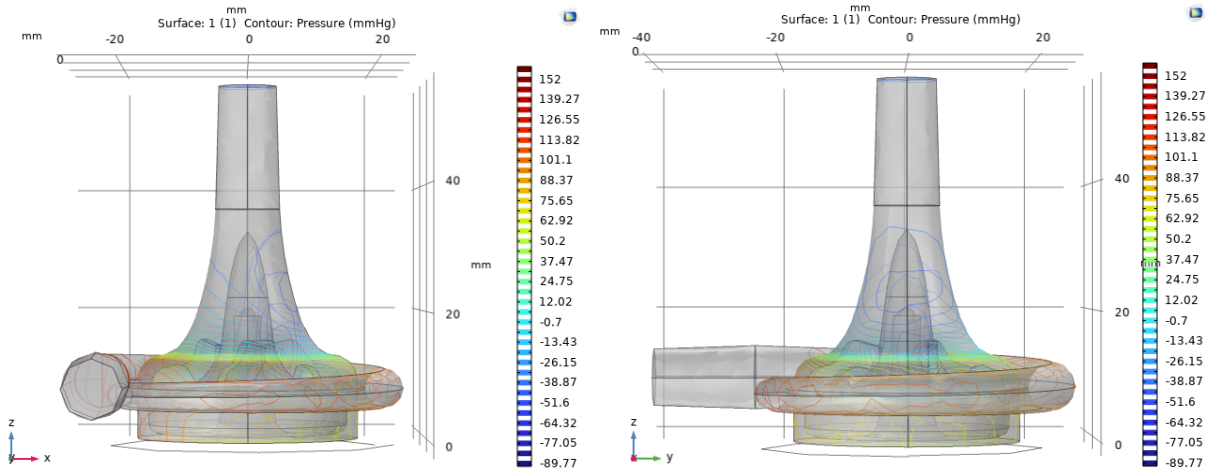

Figure 40. Additional figures of the pressure distribution in the fluid in the closed impeller pump model at 4000 RPM. Left: front view. Right: side view.

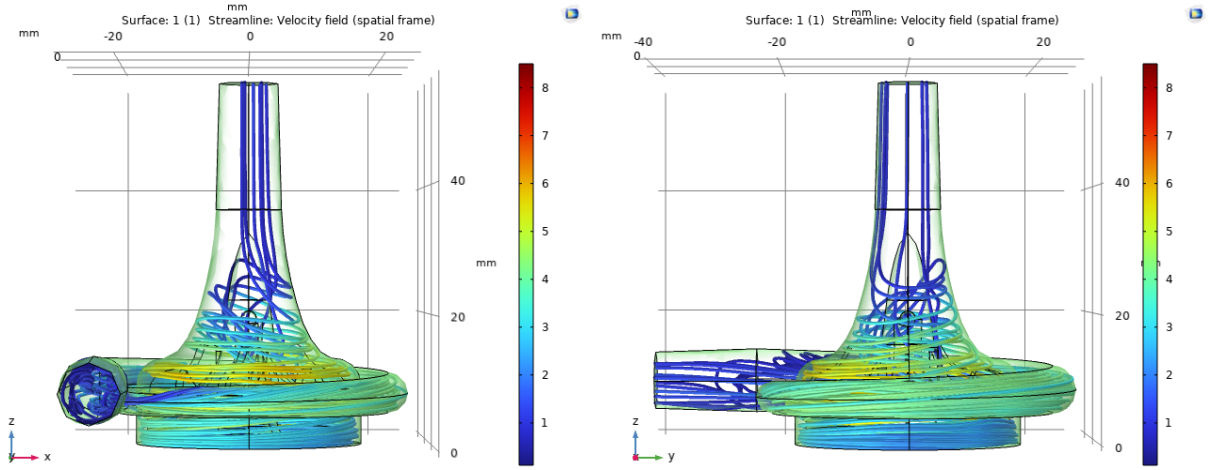

Figure 41. Additional figures of the velocity streamlines of the fluid in the closed impeller pump model at 4000 RPM. Left: front view. Right: side view.

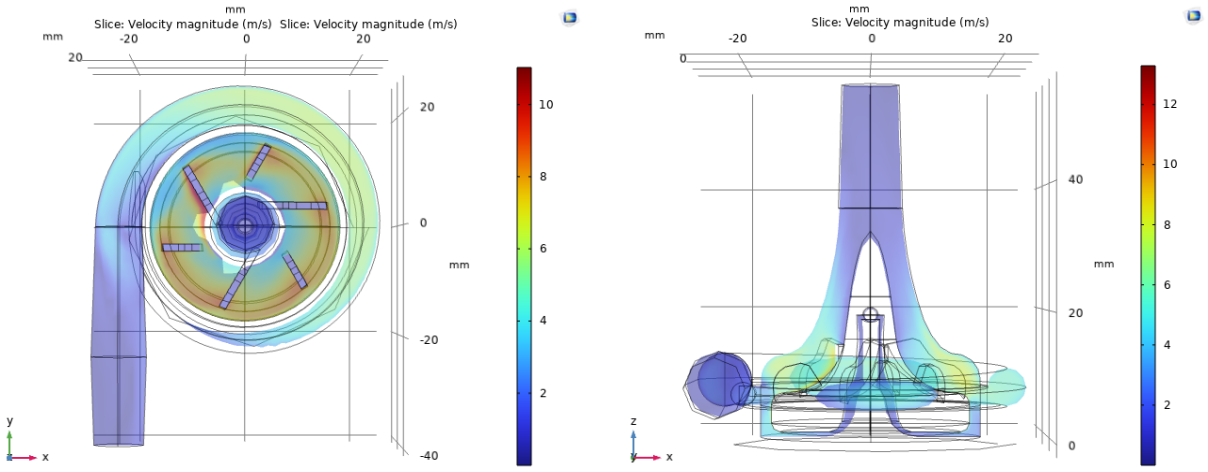

Figure 42. Fluid velocity in the closed impeller pump model at 5500 RPM. Left: top view, horizontal cross-sections. Right: front view, vertical cross-section.

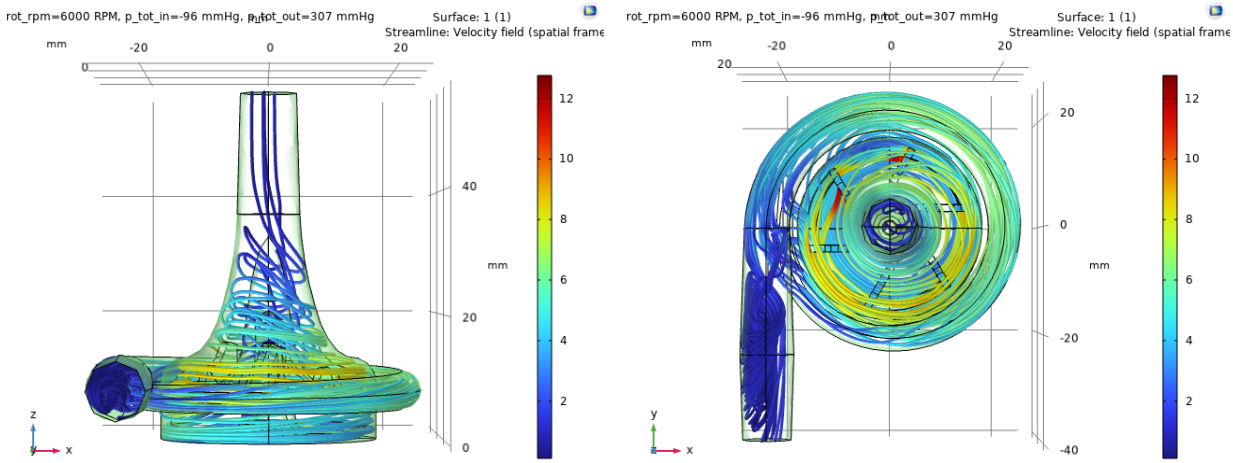

Figure 43. Flow velocity streamlines in the closed impeller pump model at 5500 RPM. Left: front view. Right: top view.

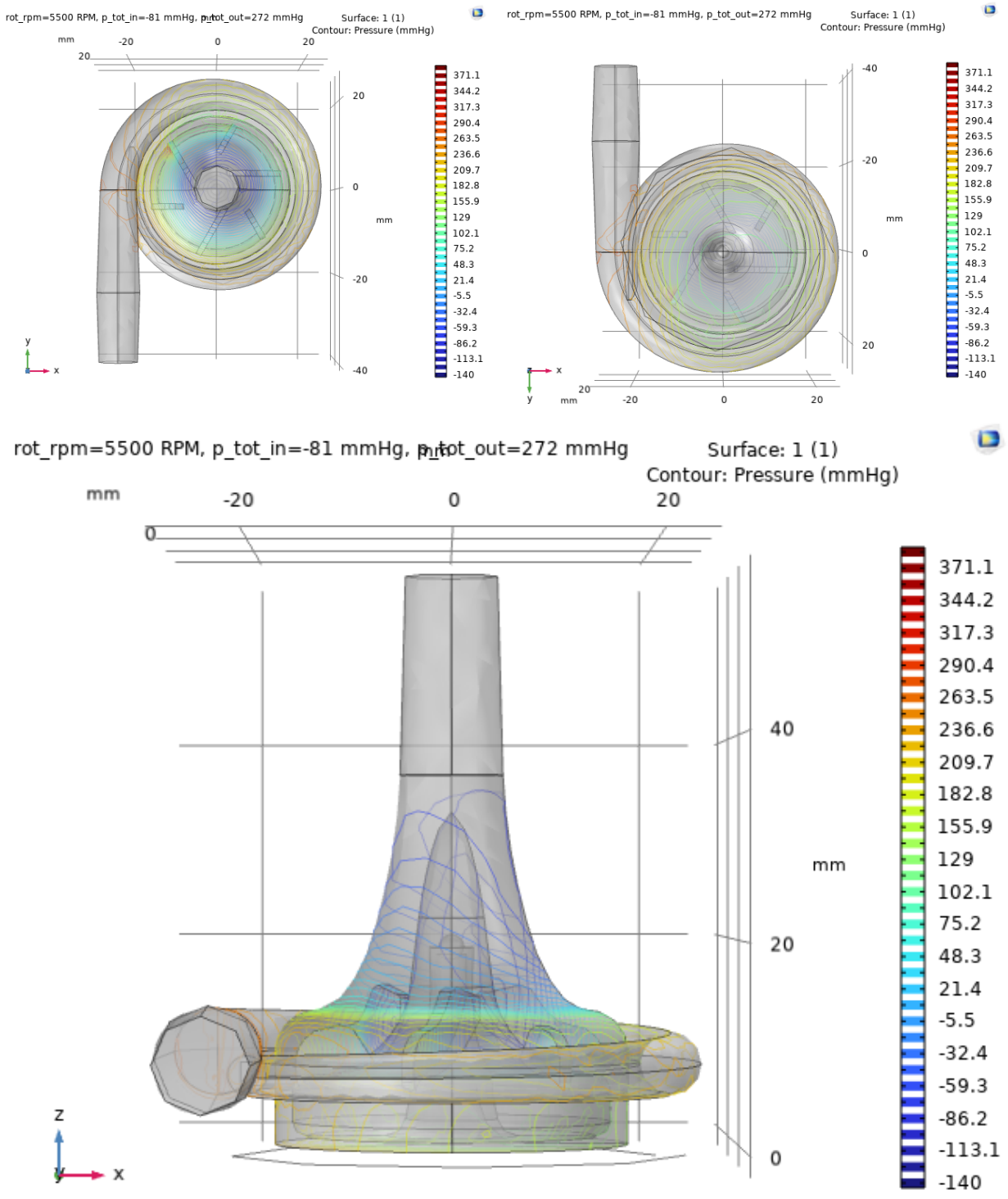

Figure 44. Pressure distribution in the closed impeller pump model at 5500 RPM. Top left: top view. Top right: bottom view. Bottom: front view.

9.12 T-test results

WORKSHEET 8

Two-Sample T-Test and CI: Fluid Flow [L/min], Group

Method

μ_1: population mean of Fluid Flow [L/min] when Group = Clamped
μ_2: population mean of Fluid Flow [L/min] when Group = Ref
Difference: $\mu_1 - \mu_2$

Equal variances are not assumed for this analysis.

Descriptive Statistics: Fluid Flow [L/min]

Group	N	Mean	StDev	SE Mean
Clamped	25	5.511	0.903	0.18
Ref	25	5.600	0.949	0.19

Estimation for Difference

Difference	95% CI for Difference
-0.089	(-0.616, 0.438)

Test

Null hypothesis $H_0: \mu_1 - \mu_2 = 0$
Alternative hypothesis $H_1: \mu_1 - \mu_2 \neq 0$

T-Value	DF	P-Value
-0.34	47	0.735

Figure 45. Results of the T-test for fluid flow between the reference group and the clamped group.

WORKSHEET 8

Two-Sample T-Test and CI: Pressure [mmHg], Group

Method

μ_1: population mean of Pressure [mmHg] when Group = Clamped
μ_2: population mean of Pressure [mmHg] when Group = Ref
Difference: $\mu_1 - \mu_2$

Equal variances are not assumed for this analysis.

Descriptive Statistics: Pressure [mmHg]

Group	N	Mean	StDev	SE Mean
Clamped	25	163.76	5.63	1.1
Ref	25	164.20	3.40	0.68

Estimation for Difference

Difference	95% CI for Difference
-0.44	(-3.10, 2.22)

Test

Null hypothesis	$H_0: \mu_1 - \mu_2 = 0$
Alternative hypothesis	$H_1: \mu_1 - \mu_2 \neq 0$

T-Value	DF	P-Value
-0.33	39	0.740

Figure 46. Results of the T-test for pressure difference between the reference group and the clamped group.

WORKSHEET 9

Two-Sample T-Test and CI: Fluid Flow [L/min], Group

Method

μ_1: population mean of Fluid Flow [L/min] when Group = Clamped
μ_2: population mean of Fluid Flow [L/min] when Group = Imp closed
Difference: $\mu_1 - \mu_2$

Equal variances are not assumed for this analysis.

Descriptive Statistics: Fluid Flow [L/min]

Group	N	Mean	StDev	SE Mean
Clamped	25	5.511	0.903	0.18
Imp closed	25	5.570	0.930	0.19

Estimation for Difference

Difference	95% CI for Difference
-0.059	(-0.581, 0.462)

Test

Null hypothesis	$H_0: \mu_1 - \mu_2 = 0$
Alternative hypothesis	$H_1: \mu_1 - \mu_2 \neq 0$

T-Value	DF	P-Value
-0.23	47	0.820

Figure 47. Results of the T-test for fluid flow between the clamped group and the experimental group.

WORKSHEET 9

Two-Sample T-Test and CI: Pressure [mmHg], Group

Method

μ_1: population mean of Pressure [mmHg] when Group = Clamped
μ_2: population mean of Pressure [mmHg] when Group = Imp closed
Difference: $\mu_1 - \mu_2$

Equal variances are not assumed for this analysis.

Descriptive Statistics: Pressure [mmHg]

Group	N	Mean	StDev	SE Mean
Clamped	25	163.76	5.63	1.1
Imp closed	25	165.60	4.07	0.81

Estimation for Difference

Difference	95% CI for Difference
-1.84	(-4.64, 0.96)

Test

Null hypothesis H_0: $\mu_1 - \mu_2 = 0$
Alternative hypothesis H_1: $\mu_1 - \mu_2 \neq 0$

T-Value	DF	P-Value
-1.32	43	0.192

Figure 48. Results of the T-test for pressure difference between the clamped group and the experimental group.

10. Bibliography

[1] Ganesh, P., & Rama Krishna, S. (2020). Diagnosis and Resolution of Vibration Issues in Vertical Centrifugal Pump. *Journal of Failure Analysis and Prevention*, *20*(3), 1019–1028. https://doi.org/10.1007/s11668-020-00910-0

[2] Shah, S. R., Jain, S. V., Patel, R. N., & Lakhera, V. J. (2013). CFD for centrifugal pumps: A review of the state-of-the-art. *Procedia Engineering*, *51*(NUiCONE 2012), 715–720. https://doi.org/10.1016/j.proeng.2013.01.102

[3] Guarrera, J. V., Henry, S. D., Samstein, B., Odeh-Ramadan, R., Kinkhabwala, M., Goldstein, M. J., … Emond, J. C. (2010). Hypothermic machine preservation in human liver transplantation: The first clinical series. *American Journal of Transplantation*, *10*(2), 372–381. https://doi.org/10.1111/j.1600-6143.2009.02932.x

[4] Perkins, J. D. (2007). Techniques to ensure adequate portal flow in the presence of splenorenal shunts. *Liver Transplantation*, *13*(5), 767–768. https://doi.org/10.1002/lt

[5] Boteon, Y. L., Laing, R. W., Schlegel, A., Wallace, L., Smith, A., Attard, J., … Mergental, H. (2018). Combined Hypothermic and Normothermic Machine Perfusion Improves Functional Recovery of Extended Criteria Donor Livers. *Liver Transplantation*, *24*(12), 1699–1715. https://doi.org/10.1002/lt.25315

[6] *eigenfrequency_analysis* 2018, accessed 1 October 2022, <https://www.comsol.com/multiphysics/eigenfrequency-analysis>

[7] *5.2 Free vibration of conservative, single degree of freedom, linear systems* n.d., accessed 1 October 2022, <https://www.brown.edu/Departments/Engineering/Courses/En4/Notes/vibrations_free_undamped/vibrations_free_undamped.htm#:~:text=Free%20vibration%20means%20that%20no,equation%20of%20motion%20is%20linear>

[8] Halliday, David; Resnick, Robert; Walker, Jearl (2005). Fundamentals of Physics. Vol. part two (7th ed.). John Wiley & Sons Ltd. ISBN 978-0-471-71716-4.

[9] *Piping vibrations* n.d., accessed 1 November 2022, <https://www.dnv.com/services/piping-vibrations-110735#:~:text=Flow%induced%20vibration%20is%20the,valves>

[10] Amalia, E., Moelyadi, M. A., & Ihsan, M. (2018). Effects of Turbulence Model and Numerical Time Steps on von Karman Flow Behavior and Drag Accuracy of Circular Cylinder. *Journal of Physics: Conference Series*, *1005*(1). https://doi.org/10.1088/1742-6596/1005/1/012012

[11] King, R. (1977). A review of vortex shedding research and its application. *Ocean Engineering*, *4*(3), 141–171. https://doi.org/10.1016/0029-8018(77)90002-6

[12] *Performance Testing of Centrifugal Pumps* 2021, accessed 10 april 2023, <https://www.student.unsw.edu.au/how-do-i-cite-electronic-sources>

[13] *Centrifugal Pump Performance Test* 2013, accessed 23 november 2022 <https://www.inspection-for-industry.com/centrifugal-pump-performance-test.html>

[14] EXPERIMENT #10: PUMPS n.d., accessed 24 November 2022, <https://docs.google.com/document/d/142ZFqST-fRDQrS4PzZd8rn_AcsL2mdzesGPx9Qxirf4/edit>

[15] Mentzos, M.,Filios, A.,Margaris, P.,Papanikas, D.,2004. “A numerical simulation of the impeller-volute interaction in a centrifugal pump,” Proceedings of International Conference from Scientific Computing to Computational Engineering. Athens, pp. 1-7.
[16] Mentzos, M., Filios, A., Margaris, P., Papanikas, D., 2005. “CFD predictions of flow through a centrifugal pump impeller,” Proceedings of International Conf. Experiments/Process/System Modelling/ Simulation/Optimization. Athens, pp. 1-8.
[17] Bacharoudis, E.,Filios, A.,Mentzos, M.,Margaris, D., 2008.Parametric Study of a Centrifugal Pump Impeller by Varying the Outlet Blade Angle. The Open Mechanical Engineering Journal 2, p. 75.
[18] Kim, J. H., Lee, H. C., Kim, J. H., Kim, S., Yoon, J. Y., & Choi, Y. S. (2015). Design techniques to improve the performance of a centrifugal pump using CFD. Journal of Mechanical Science and Technology, 29(1), 215–225. https://doi.org/10.1007/s12206-014-1228-6
[19] *Axial thrust* n.d., accessed 12 May 2023, <https://www.ksb.com/en-global/centrifugal-pump-lexicon/article/axial-thrust-1117296>
[20] *Radial thrust* n.d., accessed 12 May 2023, <https://www.ksb.com/en-global/centrifugal-pump-lexicon/article/radial-thrust-1115816>
[21] Röhrig, R., Jakirlić, S., & Tropea, C. (2015). Comparative computational study of turbulent flow in a 90° pipe elbow. International Journal of Heat and Fluid Flow, 55, 120–131. https://doi.org/10.1016/j.ijheatfluidflow.2015.07.011
[22] *Cavitation Test Setup* n.d., accessed 4 november 2022, <https://instrumentationtools.com/cavitation-test-setup/>
[23] Yartsev, A 2022, *Hepatic blood flow*, accessed 5 November 2022, <https://derangedphysiology.com/main/cicm-primary-exam/required-reading/cardiovascular-system/Chapter%20475/hepatic-blood-flow>
[24] Rocha, F. G. (2012). Liver blood flow: Physiology, measurement, and clinical relevance. Blumgart’s Surgery of the Liver, Biliary Tract and Pancreas, 74–86. https://doi.org/10.1016/B978-1-4377-1454-8.00004-7
[25] Lobritto, S. (2017). Organogenesis and Histologic Development of the Liver. Fetal and Neonatal Physiology, 2-Volume Set, 909-913.e2. https://doi.org/10.1016/B978-0-323-35214-7.00094-9
[26] Perera, T., Mergental, H., Stephenson, B., Roll, G. R., Cilliers, H., Liang, R., … Muiesan, P. (2015). First human liver transplantation using a marginal allograft resuscitated by normothermic machine perfusion. Liver Transplantation, 22(1), 120–124. https://doi.org/10.1002/lt.24369
[27] Op Den Dries, S., Karimian, N., Sutton, M. E., Westerkamp, A. C., Nijsten, M. W. N., Gouw, A. S. H., … Porte, R. J. (2013). Ex vivo normothermic machine perfusion and viability testing of discarded human donor livers. *American Journal of Transplantation*, *13*(5), 1327–1335. https://doi.org/10.1111/ajt.12187
[28] Matton, A. P. M., Burlage, L. C., van Rijn, R., de Vries, Y., Karangwa, S. A., Nijsten, M. W., … Porte, R. J. (2018). Normothermic machine perfusion of donor livers without the need for human blood products. Liver Transplantation, 24(4), 528–538. https://doi.org/10.1002/lt.25005
[29] Vogel, T., Brockmann, J. G., Quaglia, A., Morovat, A., Jassem, W., Heaton, N. D., … Friend, P. J. (2017). The 24-hour normothermic machine perfusion of discarded human liver grafts. *Liver Transplantation*, *23*(2), 207–220. https://doi.org/10.1002/lt.24672

[30] Kabagambe, S. K., Palma, I. P., Smolin, Y., Boyer, T., Palma, I., Sageshima, J., … Perez, R. V. (2019). Combined Ex Vivo Hypothermic and Normothermic Perfusion for Assessment of High-risk Deceased Donor Human Kidneys for Transplantation. *Transplantation*, *103*(2), 392–400. https://doi.org/10.1097/TP.0000000000002299
[31] Hameed, A. M., Lu, D. B., Patrick, E., Xu, B., Hu, M., Chew, Y. V., … Pleass, H. C. (2019). Brief Normothermic Machine Perfusion Rejuvenates Discarded Human Kidneys. *Transplantation Direct*, *5*(11), E502. https://doi.org/10.1097/TXD.0000000000000944
[32] Weissenbacher, A., Lo Faro, L., Boubriak, O., Soares, M. F., Roberts, I. S., Hunter, J. P., … Friend, P. J. (2019). Twenty-four–hour normothermic perfusion of discarded human kidneys with urine recirculation. *American Journal of Transplantation*, *19*(1), 178–192. https://doi.org/10.1111/ajt.14932
[33] Molina, D. K., & DiMaio, V. J. M. (2012). Normal Organ Weights in Men. The American Journal of Forensic Medicine and Pathology, 33(4), 368–372. https://doi.org/10.1097/paf.0b013e31823d29
[34] Guarrera, J. V., Henry, S. D., Samstein, B., Odeh-Ramadan, R., Kinkhabwala, M., Goldstein, M. J., … Emond, J. C. (2010). Hypothermic Machine Preservation in Human Liver Transplantation: The First Clinical Series. American Journal of Transplantation, 10(2), 372–381. https://doi.org/10.1111/j.1600-6143.2009.02932.x
[35] Guarrera, J. V., Henry, S. D., Samstein, B., Reznik, E., Musat, C., Lukose, T. I., … Emond, J. C. (2015). Hypothermic machine preservation facilitates successful transplantation of “orphan” extended criteria donor livers. American Journal of Transplantation, 15(1), 161–169. https://doi.org/10.1111/ajt.12958
[36] Vekemans, K., Liu, Q., Pirenne, J., & Monbaliu, D. (2008). Artificial circulation of the liver: Machine perfusion as a preservation method in liver transplantation. Anatomical Record, 291(6), 735–740. https://doi.org/10.1002/ar.20662
[37] Dutkowski, P., De Rougemont, O., & Clavien, P. A. (2008). Machine perfusion for “marginal” liver grafts. American Journal of Transplantation, 8(5), 917–924. https://doi.org/10.1111/j.1600-6143.2008.02165.x
[38] Jomaa, A., Gurusamy, K., Siriwardana, P. N., Claworthy, I., Collier, S., De Muylder, P., … Davidson, B. (2013). Does hypothermic machine perfusion of human donor livers affect risks of sinusoidal endothelial injury and microbial infection? A feasibility study assessing flow parameters, sterility, and sinusoidal endothelial ultrastructure. *Transplantation Proceedings*, *45*(5), 1677–1683. https://doi.org/10.1016/j.transproceed.2013.01.011
[39] Abudhaise, H., Davidson, B. R., DeMuylder, P., Luong, T. V., & Fuller, B. (2018). Evolution of dynamic, biochemical, and morphological parameters in hypothermic machine perfusion of human livers: A proof-of-concept study. *PLoS ONE*, *13*(9), 1–12. https://doi.org/10.1371/journal.pone.0203803
[40] Monbaliu, D., Liu, Q., Libbrecht, L., De Vos, R., Vekemans, K., Debbaut, C., … Pirenne, J. (2012). Preserving the morphology and evaluating the quality of liver grafts by hypothermic machine perfusion: A proof-of-concept study using discarded human livers. Liver Transplantation, 18(12), 1495–1507. https://doi.org/10.1002/lt.23550
[41] Maathuis, M.-H. J., Manekeller, S., van der Plaats, A., Leuvenink, H. G. D., ’t Hart, N. A., Lier, A. B., … Minor, T. (2007). Improved Kidney Graft Function After Preservation Using a Novel

Hypothermic Machine Perfusion Device. Annals of Surgery, 246(6), 982–991. doi:10.1097/sla.0b013e31815c4019
[42] Jochmans, I., Moers, C., Smits, J. M., Leuvenink, H. G. D., Treckmann, J., Paul, A., … Pirenne, J. (2011). The prognostic value of renal resistance during hypothermic machine perfusion of deceased donor kidneys. American Journal of Transplantation, 11(10), 2214–2220. https://doi.org/10.1111/j.1600-6143.2011.03685.x
[43] Polyak, M. M. R., Arrington, B. O. M., Stubenbord, W. T., Boykin, J., Brown, T., Jean-Jacques, M. A., … Kinkhabwala, M. (2000). The influence of pulsatile preservation on renal transplantation in the 1990s. Transplantation, 69(2), 249–258. https://doi.org/10.1097/00007890-200001270-00010
[44] Habib, S 2023, *Density Of ABS Material | The Complete Guide*, PlasticRanger accessed on 4 July 2023, <https://plasticranger.com/density-of-abs-material/#:~:text=ABS%20plastic%20density%20generally%20ranges,cm%C2%B3%20and%201%2C050%20kg%2Fm3>
[45] Tomasz, G 2021, *Comprehensive Guide on Acrylonitrile Butadiene Styrene (ABS)*, Omnexus, accessed on 26 February 2023, <https://omnexus.specialchem.com/selection-guide/acrylonitrile-butadiene-styrene-abs-plastic>
[46] Modulus of elasticity and Poisson's coefficient of polymeric materials n.d., accessed on 4 March 2023, <https://www.sonelastic.com/en/fundamentals/tables-of-materials-properties/polymers.html>
[47] Alliance N-45 Neodymium Iron Boron Magnetic Material n.d., accessed on 14 March 2023, <https://www.matweb.com/search/datasheet_print.aspx?matguid=e7eda0f5b11243a6a9ea46f21d667dc1>
[48] Bakker Magnetics. (2015). Neodymium Sintered Standard Grades, 31(June), 2015.
[49] Ravaud, R; Lemarquand, G; Babic, S; Lemarquand, V; Akyel, C (2010). "Cylindrical magnets and coils: Fields, forces, and inductances". IEEE Transactions on Magnetics. 46 (9): 3585–3590. Bibcode:2010ITM....46.3585R. doi:10.1109/TMAG.2010.2049026. S2CID 25586523.